Low-T_c Superconducting Detector for Future CMB Missions

Designing Lens-Antenna coupled Microwave Kinetic Inductance Detectors applicable to 50-90 GHz using β-Ta

Master's Thesis

Matthijs Roos

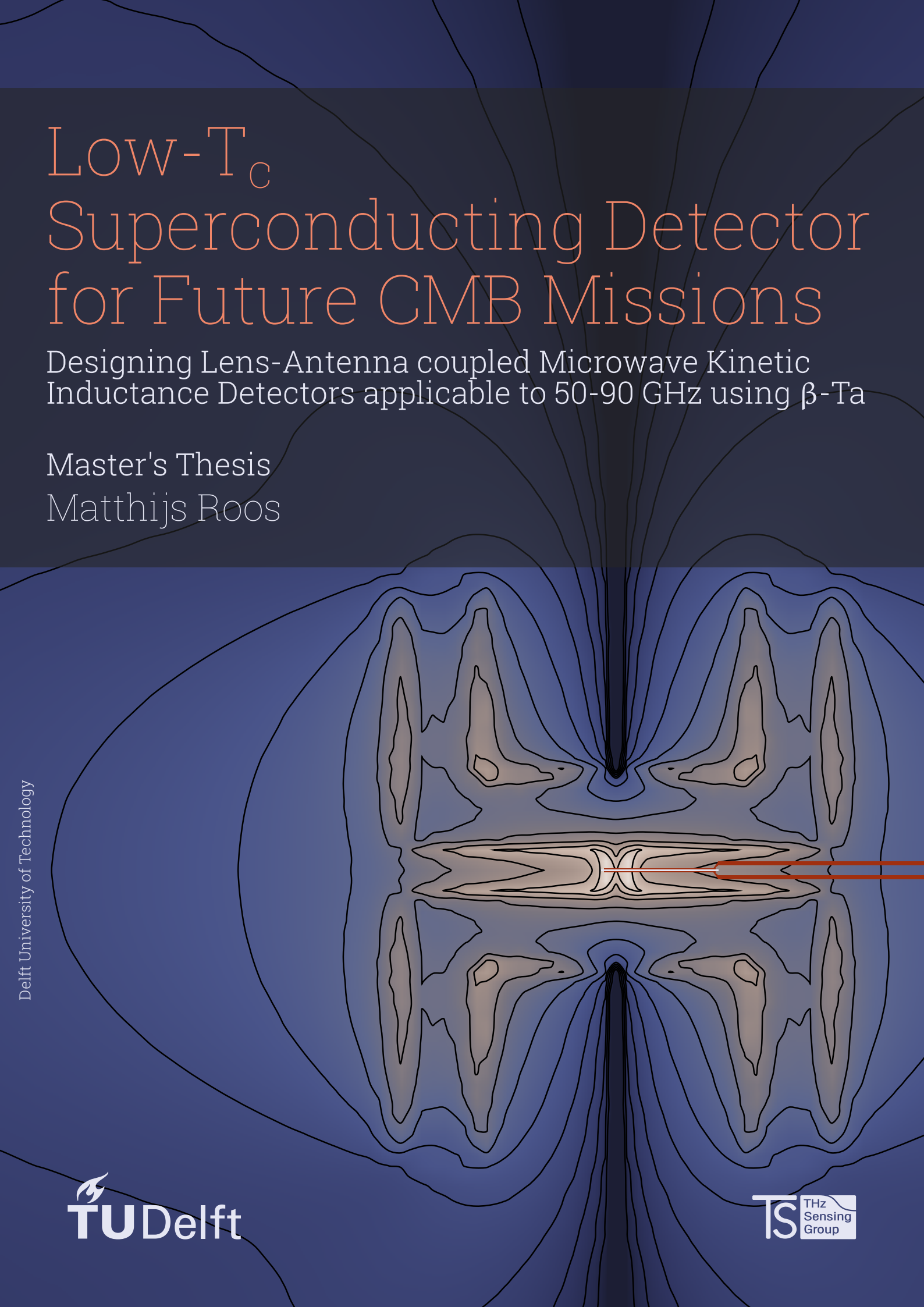

Delft University of Technology

TU Delft

THz Sensing Group

Low-T_c Superconducting Detector for Future CMB Missions

Designing Lens-Antenna coupled Microwave Kinetic Inductance Detectors applicable to 50-90 GHz using β-Ta

by

Matthijs Roos

to obtain the degree of Master of Science in Applied Physics,
within the track Physics for Instrumentation,
at the Delft University of Technology,
to be defended publicly on Friday 12 June 2026 at 13:00.

Student number:	5363446	
Project duration:	6 October 2025 – 29 May 2026	
Thesis committee:	Prof. dr. ir. J.J.A. Baselmans,	TU Delft / SRON, supervisor
	Prof. dr. ir. H.S.J. van der Zant,	TU Delft
	dr. ir. S.O. Dabironezare,	TU Delft / SRON
	dr. K. Karatsu,	TU Delft / SRON, supervisor

Cover: *Hybrid kinetic inductance detector structure projected onto the near-field beam pattern of the 70GHz twin-slot antenna design obtained in this thesis. The antenna is designed to couple pair-breaking radiation to the β-Ta strip, which can be seen as the center line of the narrow coplanar waveguide in the center of the electric field.*

An electronic version of this thesis is available at http://repository.tudelft.nl/.

TU Delft

THz Sensing Group

Abstract

The next generation of Cosmic Microwave Background (CMB) missions require sensitive detectors to probe the processes that shaped the early Universe. The $50 - 90$GHz frequency range is of particular interest, both for the measurement of the weak B-mode polarization patterns from primordial gravitational waves and for detection of spectral distortions in the CMB.
Since Microwave Kinetic Inductance Detectors (MKIDs) offer great multiplexing capabilities, high sensitivity, easy fabrication, and reduced cost, they would be ideal for CMB missions. MKIDs are superconducting pair-breaking detectors, which makes them capable of detecting photons with a minimum photon energy of twice the superconducting gap energy, $hf \geq 2\Delta$. The superconducting gap energy is intrinsic to the superconductor embedded in the detector's hybrid microwave resonator structure ($\Delta \approx 1.76 k_B T_c$), and thus poses a direct limit on the frequencies the detector can measure. For example, the conventionally used Aluminum ($T_c = 1.2 - 1.4$K) would only be able to detect photons with frequencies larger than 90GHz. β-phase Tantalum (β-Ta), a disordered superconductor with $T_c = 0.6 - 1.0$K, would enable detection of frequencies as low as 45GHz.
In this thesis, we therefore investigate the viability of using β-Ta in designing hybrid MKIDs for frequencies in the $50 - 90$GHz range.

The effect of quasiparticle trapping due to disorder in superconductors is known to reduce the sensitivity of MKIDs. Consequently, the volume of β-Ta within the microwave resonator must be minimized to mitigate this effect and achieve photon-noise-limited sensitivity. We opt for a lens-antenna coupled hybrid MKID design to decouple the frequency sensitive antenna and the active volume of the resonator, such that both can be optimized independently.

The detectors presented in this thesis have been designed for 70GHz radiation, at the center of the $50 - 90$GHz range. The lens antenna features an extended hemispherical lens coupling radiation from a black body source to a twin-slot antenna. The twin-slot antenna couples this pair-breaking radiation to the volume of β-Ta. We consider β-Ta/NbTiN hybrid MKIDs for the quarter-wave resonators. To approximate the properties of the superconducting materials at both readout and pair-breaking frequencies, Mattis-Bardeen theory is used.

Given the large normal state resistivity of β-Ta, the narrow coplanar waveguide in the hybrid MKID has a large characteristic impedance. This makes it difficult for the twin-slot antenna to match in impedance. Therefore, the dimensions of the narrow coplanar waveguide have to be optimized to minimize both its active volume and characteristic impedance, simultaneously. We obtain a trade-off in its dimensions, which is also limited by UV lithography fabrication limitations. The twin-slot antenna design is subsequently optimized for a sufficient impedance match.

We identify radiation losses at readout frequencies due to the addition of the twin-slot antenna structure. These losses are found to exceed the dissipation within the quasiparticle system predicted by Mattis-Bardeen theory at low operating temperatures, and would therefore dominate the internal quality factor of the MKIDs.

Conclusively, this thesis presents a viable methodology to design MKIDs in the range of $50 - 90$GHz using β-Ta. The dimension optimizations of the narrow coplanar waveguide and the twin-slot antenna are not fully decoupled, and their impedance matching poses challenges to the MKID design. For future research, it is important to find an approach that would give more engineering freedom in their separate designs.

Acknowledgements

First and foremost, I would like to extend my heartfelt gratitude toward my supervisors, Prof. dr. ir. Jochem Baselmans and dr. Kenichi Karatsu.
Jochem, thank you for your addictive enthusiasm about experimental astronomy. The occasional specific suggestions in particular made me curious to study new aspects about this project. Above all, I admire the way you instantly seemed to understand how to support me whenever I ran into problems.
Kenichi, thank you for your guidance and support throughout this entire project. Not only the countless discussions, but also your help in interpreting my findings were really valuable to me. Besides important lessons in doing research, you have taught me to always be critical and realistic.

Additionally, I would like to thank dr. Giulia Conenna for all her technical insights during the project. I am curious to see your next steps in developing low-T_c MKIDs.
I would also like to thank both Kenichi and Giulia for their thorough feedback, which helped me to get this thesis to its final form.

I would like to thank dr. ir. Shabab Dabironezare for teaching me important concepts of electromagnetics that were vital for my design work.

I would like to thank the cleanroom staff at SRON who were involved in delivering feedback on my mask report and currently contribute to the fabrication of the chips.
In addition, I would like to thank ing. David Thoen for his enthusiasm in sharing essential implications of using certain fabrication techniques.

I am also grateful to all the members of the Terahertz Sensing group. You have created an incredibly welcoming research environment that I was proud to be a part of.
I want to thank all fellow MSc students for all our time together, especially our routine coffee/tea breaks. In particular, Jim, Mees, Pien, and Tristan, thank you for the many conversations and laughs over the span of my thesis.

As the completion of this thesis also means that my time studying in Delft is almost coming to an end, I would like to take this opportunity to express my gratitude for all the friendships I have made throughout my years in Delft.
From the ones that I have known since day one to those that I only got to know in recent years, thank you for making the countless hours spent studying together on the *Plein* so much more enjoyable.

Furthermore, I would like to thank all my fellow board members. I cannot stress enough how happy I am to now call you my close friends.

A special thanks to Cat and Gabriël for their endless support, whether we are practically neighbors or on completely different continents.

Finally, I want to express my gratitude toward my brother and parents. Daan, thank you for all our conversations, not only concerning my studies, but also about all the interests we share. I not only see in you a great brother, but more importantly an amazing mentor. I wish you the best of luck with the academic journey ahead of you. My parents, for showing interest in everything I do. Regardless of where and when, you always do anything to be there for me. I want you to know that I value this deeply.

Contents

1 Introduction

What secrets does the cosmos still hide from us? Although advances in astronomical instrumentation over the last few decades have allowed us to unravel numerous, there are still many questions left unanswered about the phenomena in our Universe. One field of interest in particular is the early Universe, where we could find answers to how fundamental structures of the Universe grew and whether processes like Cosmic Inflation occurred. While the laws of physics do not allow us to directly look back in time, there is a different approach to research the history of the Universe.

1.1. Cosmic Microwave Background

The measurement of a seemingly isotropic and unpolarized excess noise temperature marked the discovery of the Cosmic Microwave Background (CMB) [1]. It is now well-known that the hot processes that shaped the early Universe can be seen as relic radiation, observed as a background temperature of approximately 2.73K [2]. However, the CMB blackbody spectrum appeared not to be perfectly uniform and isotropic: spectral distortions, polarization patterns, and temperature anisotropies shape the CMB (see figure 1.1).

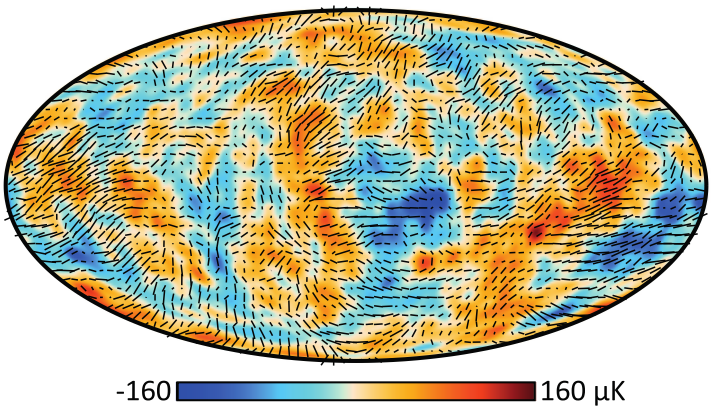

Figure 1.1 – Polarization map overlaid on the temperature fluctuations in the Cosmic Microwave Background (both smoothed to 5°), as observed by the Planck Collaboration [3].

Processes driving matter and radiation out of thermal equilibrium create spectral distortions in the CMB. The associated signals are usually formed by energy exchange between electrons and photons through Compton scattering. For an overview of these different processes, see figure 1.2.

Depending on whether scattering happened efficiently, we can observe two types of distortions that refer to different epochs in the thermal history of the Universe. μ-distortions are seen in the epoch after thermalization, and are due to early photon emission and scattering. As scattering gradually became inefficient, we start to see y-distortions for later epochs, which are due to contact with hot electrons [5, 6].

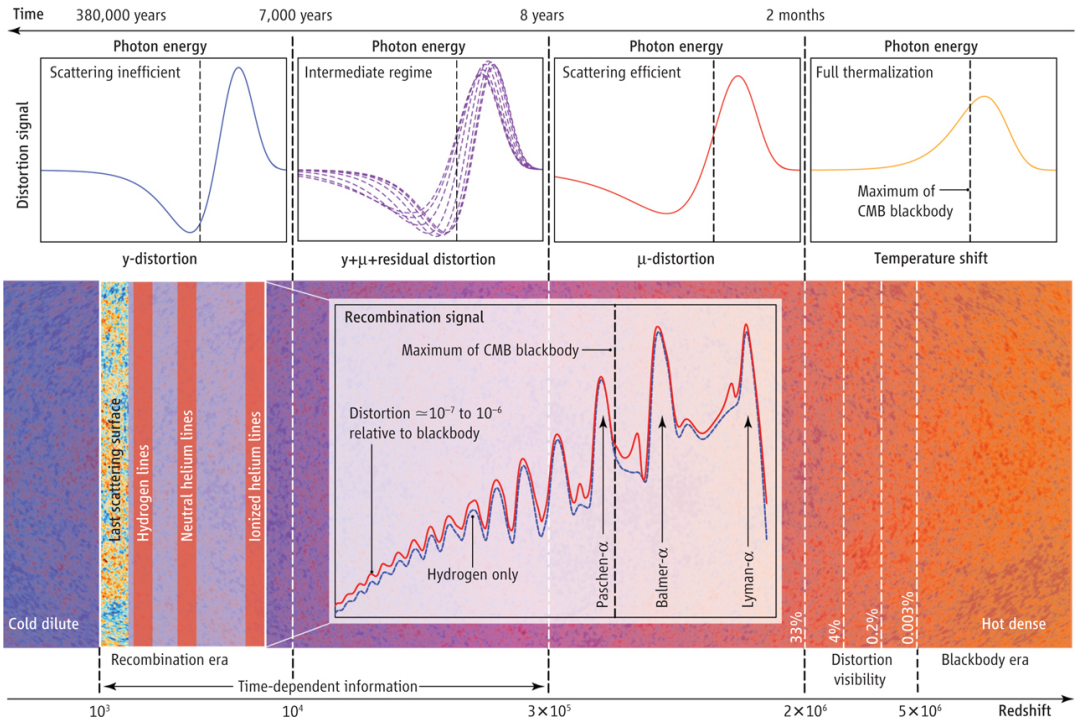

Figure 1.2 – Different spectral distortion signals and how they shaped the CMB spectrum across time. The shape of each distortion contains valuable information that is epoch-dependent. This allows for the different sources to be distinguishable. The line-emission seen in the inset is created during the cosmological recombination eras. Figure from [4]. For further reading on the spectral distortions, see [5].

All these deviations from an isotropic blackbody spectrum thus contain information on the thermal history of the Universe. These spectral distortions are relatively faint, corresponding to fractional changes in intensity in the order of $10^{-8} - 10^{-6}$.

Another prominent example of spectral distortion is the inverse Compton scattering of CMB photons with high-energy electrons inside of galaxy clusters. This effect is commonly referred to as the Sunyaev-Zeldovich effect (SZE) [6, 7]. One can observe inverse-Compton-scattered photons toward any reservoir of hot plasma. Therefore, galaxy formation, being a source of large quantities of moving hot ionized gas, leads to substantial distortions [8, 9]. An interesting and notable feature of the SZE is that it is redshift-independent, therefore providing a large-scale probe of the structure of the Universe [5, 9].

The CMB also contains polarization patterns. While these are observed as E-mode (curl-free) polarization, there might also be a B-mode (curl) component present. Those B-mode patterns would arise from primordial gravitational waves that were generated during Cosmic Inflation [10]. In fact, the observation of B-mode patterns in the CMB would be direct evidence for Cosmic Inflation [11].
The B-mode patterns would typically be rather faint. Besides the primordial gravitational waves, there are a number of sources that are orders of magnitude more apparent. Weak gravitational lensing of E-modes in the foreground can induce B-modes [12]. Then, there are several foreground sources like synchrotron emission or emission from dust aligning with local magnetic fields, resulting in B-modes in their photon emissions [13]. All in all, a detector to observe this effect would have to be sensitive to be able to differentiate the relatively weak effect these primordial gravitational waves left on the CMB.

Need for CMB missions

To summarize the previous section, while relatively faint, the spectral distortions and polarization patterns in the Cosmic Microwave Background probe the processes that shaped the early Universe.
Consequently, there is a need for CMB missions, focused on frequencies ranging from 50GHz to several THz [14]. In particular, the lower side of this frequency range is of scientific interest. The $50 - 90$GHz range shows the lowest level of foreground contamination for B-mode measurements [15], and covers the majority of the decrement in spectral distortions [10]. CMB missions thus require sensitive detection technologies that are capable of covering this frequency range.

Traditionally, one would think of using the highly sensitive Transition-Edge Sensor (TES) [16], a type of bolometer, to do CMB experiments with. An example of such a CMB mission is the BICEP/Keck Array [17]. TESs have limited multiplexing capabilities, however, and therefore require complex electronics to make readout of large arrays possible.
More attractive for CMB missions is the use of Microwave Kinetic Inductance Detectors (MKIDs). MKIDs allow for high achievable multiplexing, high sensitivity, easier fabrication due to its simple architecture, and for a more cost-friendly instrument [18–20].
Another option would be to use Thermal Kinetic Inductance Detectors (TKIDs), a type of KID that combine multiplexing capabilities with the sensitivity of bolometers. TKIDs allow for engineering freedom, at the cost of a complex fabrication process [21, 22], making them less attractive than MKIDs.
MKIDs have already been widely used in missions for many years. Recent examples include DESHIMA2.0 [23], and the proposed TIFUUN [24] and PRIMA [25]. Recent examples of CMB missions using MKIDs include GroundBIRD [26] and the proposed FOSSIL [27].

1.2. Using MKIDs for CMB missions

When a superconducting material is cooled below its critical temperature T_c, the electrons inside of it form Cooper pairs [28]. These Cooper pairs move without any resistance. When an alternating current is applied on the Cooper pairs, their inertia will give rise to an inductive behavior of the material, which we call kinetic inductance. At a non-zero temperature, not all of the electrons will be paired up. Instead, some electrons will be in an excited state, where they form electron-hole superpositions, so-called quasiparticles. These quasiparticles do dissipate energy.
An incident photon with energy hf can also break Cooper pairs if its energy exceeds the pair-breaking energy 2Δ. This would result in the kinetic inductance of the superconductor to change. This change can be cleverly exploited when the superconductor is integrated in a microwave resonator circuit (see figure 1.3a). An absorbed pair-breaking photon will then cause the resonator's properties to change, which can be read out through coupling to a readout line. This is the principle of an MKID: a change in the number of quasiparticles in the superconductor shifts the resonance frequency and changes the amplitude of the resonance dip (see figure 1.3b) [29].

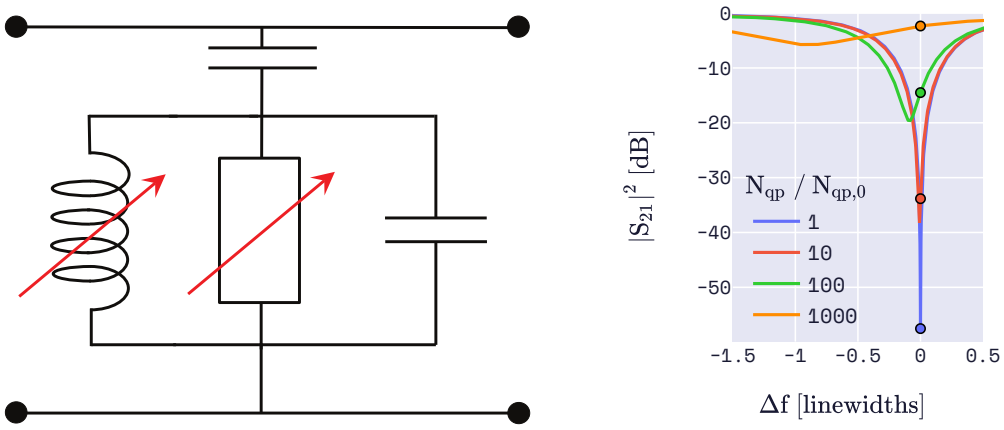

(a) (b)

Figure 1.3 – **(a)** Simplified microwave resonator circuit, capacitively coupled to a readout line. Breaking of Cooper pairs into quasiparticles changes the kinetic inductance and resistance inside the resonator. Image taken from [30]. **(b)** The effect of increasing the quasiparticle number N_{qp} on the forward transmission S_{21} of an MKID. Here, $N_{qp,0}$ represents the number of quasiparticles at an operating temperature $T = T_c/10$. The resonance frequency shifts due to the change in kinetic inductance, and the amplitude decreases due to the change in resistance.

Conventionally, Aluminum (Al) is used as the material for the superconducting film embedded in the resonator. Given a $T_c = 1.2 - 1.4$K, it is consequently able to detect photons as low as approximately $f \approx 3.53 k_B T_c/h \approx$ 90GHz. This entails that we would not be able to detect photons in the aforementioned frequency range of $50 - 90$GHz. For us to be able to use the advantage of MKIDs for these lower frequencies, we have to employ a superconductor with a lower critical temperature than that of Al.

One material that would have a critical temperature low enough, would be β-Ta with a $T_c = 0.6 - 1.0$K, dependent on deposition conditions [31–33]. β-Ta is a metastable form of Tantalum with a complex tetragonal unit cell structure [34–36]. While β-Ta has the potential to reach the required critical temperature, it is also known to be a disordered superconductor. Disordered superconductors are characterized by a high normal state sheet resistance R_N, which results in a high kinetic inductance $L_k = \hbar R_N/\pi\Delta$ [32, 37]. The disorder of β-Ta is also known to limit the response of KIDs due to the effect of quasiparticle trapping, an this sensitivity reduction can only be mitigated if we minimize its volume within the detector [38].
Other low-T_c superconductors could also be considered. An example is Hafnium (Hf, $T_c = 0.13 - 0.6$K), which is used at UCSB and JPL for optical and near-infrared MKIDs [32, 39]. However, initial work has shown that it is difficult to integrate Hf into hybrid devices.
There have been applications of β-Ta in superconducting devices. In the context of MKIDs, this also includes exploiting its resistivity to create an absorbing mesh to protect the superconducting detectors from cosmic rays [40] and suppress stray light [41]. β-Ta is also used to absorb radiation in optical LEKIDs [42]. Recently, the key quasiparticle dynamics defining disorder in β-Ta were explored [43].

1.3. A Low-T_c Superconducting Detector

This thesis will explore the viability and potential challenges of implementing a superconducting material different than the conventionally used Al in an MKID array, with the intent of it having a critical temperature low enough to make detection between $50 - 90$GHz possible. The research goal will be as follows:

Design a Microwave Kinetic Inductance Detector applicable to CMB missions in 50 − 90 GHz using a low-T_c superconductor.

To obtain the research goal, we will use β-Ta as our low-T_c superconductor.

The fundamental sensitivity limit for a superconducting detector is the noise due to fluctuations in the photon arrival rate, the photon noise [44]. Another goal is thus to achieve photon-noise limited-performance of the detector, as we seek a detector that is able to differentiate the weak signals described in section 1.1.
We mentioned that the reduced sensitivity of β-Ta can only be mitigated by minimization of its volume. This requires the volume of the β-Ta to be independent of the frequency of the incoming radiation. For LEKIDs, the volume and the frequency are fundamentally coupled, and this decoupling is impossible. For this reason, we try to achieve the research goal through the use of β-Ta in a lens-antenna coupled hybrid KID.

This thesis will be structured as follows.
In chapter 2, we consider the theoretical background required to understand how superconductors can be used in MKIDs. We also discuss how one can probe the dissipation and kinetic inductance through changes in the resonator properties. Several important noise sources are considered. Additionally, we elaborate on the motivation for a hybrid KID design. This chapter concludes by discussing different implications of disorder in superconductors.
We proceed to cover the design method for a lens-antenna coupled hybrid KID in chapter 3. We consider the choices for a twin-slot antenna and an extended hemispherical lens, and show how they can collectively be analyzed. We conclude by discussing how we can model KID designs.
Next, these methods are applied in chapter 4 to design lens-antenna coupled hybrid KIDs using β-Ta. We elaborate on the design constraints for each of the elements within the detectors, and continue with optimizing them based on those constraints. We conclude by analyzing the lens antenna and the effect of coupling the antenna to the KIDs.
Combining the design of the different elements of the lens-antenna coupled KIDs, we present the designs of chips that can be used for experimental evaluation in chapter 5.
Finally, the conclusions of this thesis, as well as suggestions for future research, are presented in chapter 6.

2

Theory of a Superconducting Detector

This chapter provides the theoretical background on how superconductors can be used to build a Kinetic Inductance Detector (KID). We start by describing how electrons in a superconducting state lead to a complex conductivity (section 2.1). Next, we consider the integration of superconducting materials in a microwave resonator, and show how it can be used as a detector (section 2.2). We conclude this chapter by discussing the implications of disorder in a superconductor (section 2.3).

2.1. Superconductivity

2.1.1. Quasiparticles and Cooper pairs

Within a normal metal, electrons can move almost freely through its lattice: any interactions between electrons are negligible and we can use the free electron model. As temperature approaches zero, the electrons fill up all possible kinetic energy states up to the Fermi energy.
The electrons directly interact with each other through the strong Coulomb repulsion. This interaction acts over distances larger than the typical distance between electrons. As a result, an electron, being surrounded by many in an electron cloud, will only experience an effectively screened Coulomb repulsion [30].

For superconductors, we need to go beyond the free electron model and incorporate the interaction between the electrons and the ionic lattice of the material. The positively charged ions within the lattice are attracted to an electron moving through it. As their inertia is larger than that of electrons, it takes more time for the ions to restore to their initial position in the lattice. This leaves a trail of larger positive charge density behind the electron, which can cause an indirect attraction to another electron. This attraction can be stronger than the screened Coulomb repulsion, allowing for two electrons with opposite spin and momentum to pair up and form a Cooper pair (see figure 2.1a) [45]. For temperatures below a critical temperature T_c, the thermal energy is too low and Cooper pairing is energetically favored. This theory of superconductivity was first described by Bardeen, Cooper, and Schrieffer (BCS) [28].

In the ground state, or zero temperature, all electrons will be in the lowest energy state and thus bound in Cooper pairs. They can all exist together in this state, as Cooper pairs are bosonic and the Pauli-exclusion principle does not apply to them. Any excitation from this ground state takes the form of two 'Bogoliubov' quasiparticles, which is a superposition of electron-like and hole-like quasiparticles [37]. It takes a minimum energy of $E > 2\Delta$ to break a Cooper pair. Here, Δ represents the so-called superconducting gap energy, a minimum excitation energy. Figure 2.1b shows pair-breaking by an incident photon schematically.

The gap energy Δ is a function of temperature, which is shown in figure 2.2a[1]. In the limit of $T \to 0$, the gap energy converges to $\Delta_0 \approx 1.76 k_B T_c$ [46]. For $T \ll T_c$, we can approximate its temperature dependency as $\Delta(T) \approx \Delta_0 - \sqrt{2\pi\Delta_0 k_B T} e^{-\Delta_0/k_B T}$ [37].
As Δ_0 is proportional to T_c, we can convert to a minimum pair-breaking frequency corresponding to $\hbar\omega = 2\Delta_0$, or $hf_c \approx 3.53 k_B T_c$.

[1] A derivation of how to solve $\Delta(T)$ numerically for BCS superconductors is given in Appendix A.1.

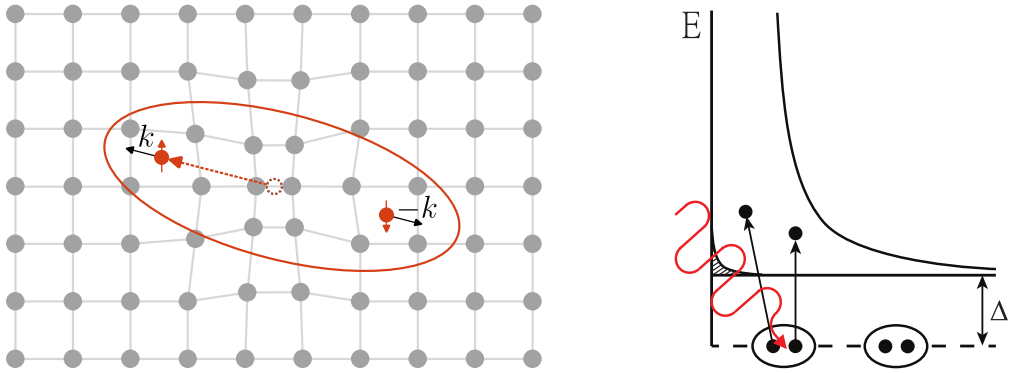

(a) (b)

Figure 2.1 – **(a)** A moving electron (orange) leaves behind a higher positive charge density within the ionic lattice (connected gray dots) which only restores slowly, attracting another electron. The two electrons, with opposite spins and momenta, pair up to form a Cooper pair. Figure adapted from [43]. **(b)** Schematic of a photon breaking a Cooper pair. A photon (red) of energy $\hbar\omega > 2\Delta$ breaks a Cooper pair and excites the two quasiparticles (black). Vertical axis represents energy E, to which the quasiparticle density of states is added. Figure from [30].

At finite temperature, part of the electrons will thus be in an unbound state. This corresponds to a quasiparticle density of states $N_s(E) = N_0 \mathrm{Re}\{E/\sqrt{E^2 - \Delta^2}\}$, with N_0 being the (single spin) normal state density of states. Multiplied by the Fermi function $f(E) = (1 + e^{E/k_BT})^{-1}$, and integrated over all energy states, the density of states yields the quasiparticle number density [37],

$$n_{qp} = 4\int_0^\infty N_s(E) f(E) dE \approx 2\Delta_0 N_0 \sqrt{\frac{2\pi k_B T}{\Delta_0}} e^{-\Delta_0/k_BT}, \tag{2.1}$$

where the approximation is valid for $T \ll T_c$. Figure 2.2b shows n_{qp} as a function of temperature.

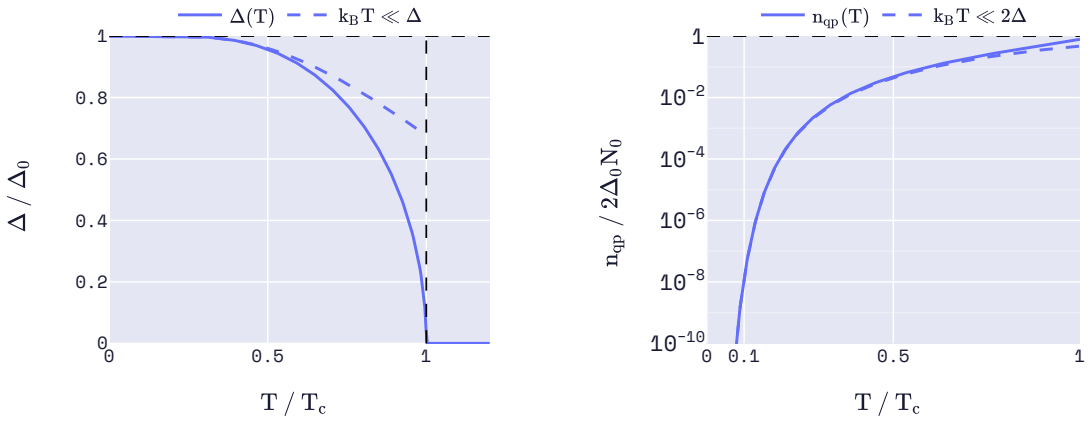

(a) (b)

Figure 2.2 – **(a)** Superconducting gap energy as a function of temperature. **(b)** Quasiparticle density in a superconductor as a function of temperature. In (a) and (b), the low-temperature approximations $\Delta(T) \approx \Delta_0 - \sqrt{2\pi\Delta_0 k_B T} e^{-\Delta_0/k_BT}$ and $n_{qp}(T) \approx 2N_0\sqrt{2\pi\Delta_0 k_B T} e^{-\Delta_0/k_BT}$ are respectively added as blue dashed lines.

2.1.2. Complex conductivity

Mattis and Bardeen (MB) showed that through BCS-theory, one can formulate a description of a complex conductivity [47]. They did so by integrating over all possible ways to absorb photons of energy $\hbar\omega$. It can be rewritten to match the form $\sigma = \sigma_1 - j\sigma_2$, by splitting the integral based on intervals where the integrand is either real or imaginary[2].

[2] Appendix B elaborates on the formulation and interpretation of the Mattis-Bardeen equations.

In the dirty or the extremely anomalous limit, the Mattis-Bardeen equations are defined as [47],

$$\frac{\sigma_1}{\sigma_N} = \frac{1}{\hbar\omega}\int_{\Delta}^{\infty}[2f(E) - 2f(E+\hbar\omega)]\frac{E(E+\hbar\omega)+\Delta^2}{\sqrt{E^2-\Delta^2}\sqrt{(E+\hbar\omega)^2-\Delta^2}}dE \tag{2.2}$$
$$- \frac{1}{\hbar\omega}\int_{\min[\Delta-\hbar\omega;\,-\Delta]}^{-\Delta}[1 - 2f(E+\hbar\omega)]\frac{E(E+\hbar\omega)+\Delta^2}{\sqrt{E^2-\Delta^2}\sqrt{(E+\hbar\omega)^2-\Delta^2}}dE,$$

$$\frac{\sigma_2}{\sigma_N} = \frac{1}{\hbar\omega}\int_{\max[\Delta-\hbar\omega;\,-\Delta]}^{\Delta}[1 - 2f(E+\hbar\omega)]\frac{E(E+\hbar\omega)+\Delta^2}{\sqrt{\Delta^2-E^2}\sqrt{(E+\hbar\omega)^2-\Delta^2}}dE, \tag{2.3}$$

where $f(E)$ is the Fermi function at energy E. σ_N is the normal state conductivity, which scales with the total number of electrons present in the material. Its reciprocal is the normal state resistivity $\rho_N = 1/\sigma_N$. For $\hbar\omega, k_BT \ll 2\Delta$, we can approximate the Mattis-Bardeen equations for thermally excited quasiparticles [48],

$$\frac{\sigma_1}{\sigma_N} \approx \frac{4\Delta}{\hbar\omega}e^{-\frac{\Delta}{k_BT}}\sinh\left(\frac{\hbar\omega}{2k_BT}\right)\mathrm{K}_0\left(\frac{\hbar\omega}{2k_BT}\right), \tag{2.4}$$

$$\frac{\sigma_2}{\sigma_N} \approx \frac{\pi\Delta}{\hbar\omega}\left[1 - 2e^{-\frac{\Delta}{k_BT}}e^{-\frac{\hbar\omega}{2k_BT}}\mathrm{I}_0\left(\frac{\hbar\omega}{2k_BT}\right)\right], \tag{2.5}$$

where K_0 and I_0 are the zeroth-order Bessel functions of the first and second kind, respectively. Complex conductivity as both a function of frequency and temperature is shown in figure 2.3.

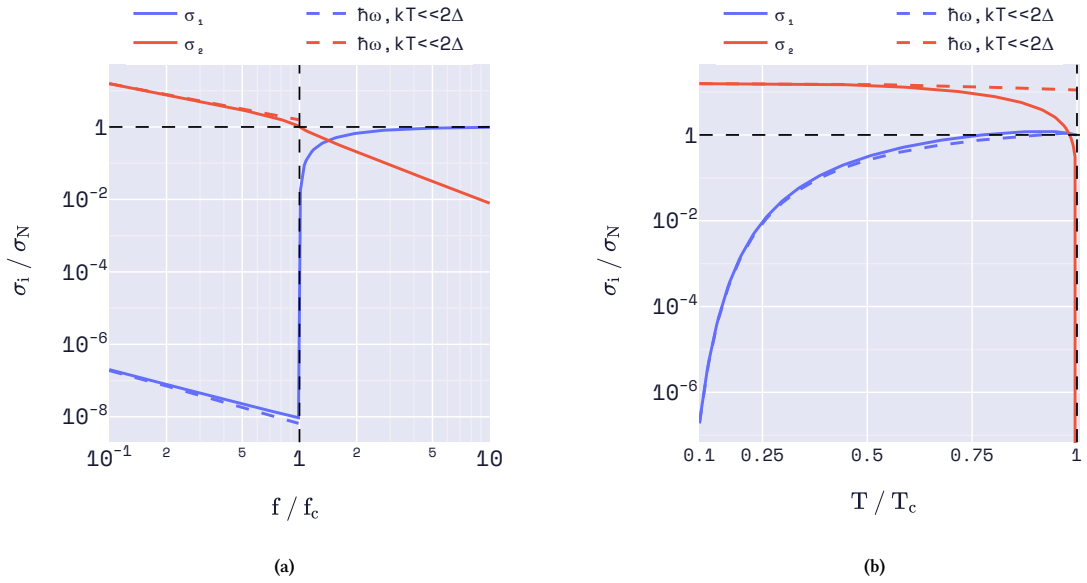

Figure 2.3 – Complex conductivity as a function of **(a)** frequency (at $T = T_c/10$) and **(b)** temperature (at $f = f_c/10$) for a superconductor with $T_c = 0.6$K and $\rho_N = 49\mu\Omega$·cm. Dashed colored lines are added for approximations determined for $\hbar\omega, k_BT \ll 2\Delta$.

σ_1 and σ_2 directly relate to the number of electrons bound in Cooper pairs and excited as quasiparticles (see figure 2.4a). Therefore, with a change of quasiparticle density, we see a change in complex conductivity. For low temperatures ($T \ll T_c$), $d\sigma/dn_{qp}$ is equivalent for slight changes in temperature and absorption of pair-breaking photons [48]. Using the low temperature approximations of $\Delta(T)$ and n_{qp}, one can then derive a lowest order approximation [48],

$$\frac{d\sigma_1}{dn_{qp}} \approx \frac{\sigma_N}{N_0\hbar\omega}\sqrt{\frac{2\Delta_0}{\pi k_BT}}\sinh\left(\frac{\hbar\omega}{2k_BT}\right)\mathrm{K}_0\left(\frac{\hbar\omega}{2k_BT}\right), \tag{2.6}$$

$$\frac{d\sigma_2}{dn_{qp}} \approx -\frac{\sigma_N\pi}{2N_0\hbar\omega}\left[1 + \sqrt{\frac{2\Delta_0}{\pi k_BT}}e^{-\frac{\hbar\omega}{2k_BT}}\mathrm{I}_0\left(\frac{\hbar\omega}{2k_BT}\right)\right]. \tag{2.7}$$

Both the numerical derivative and these approximations are shown as a function of temperature in figure 2.4b.

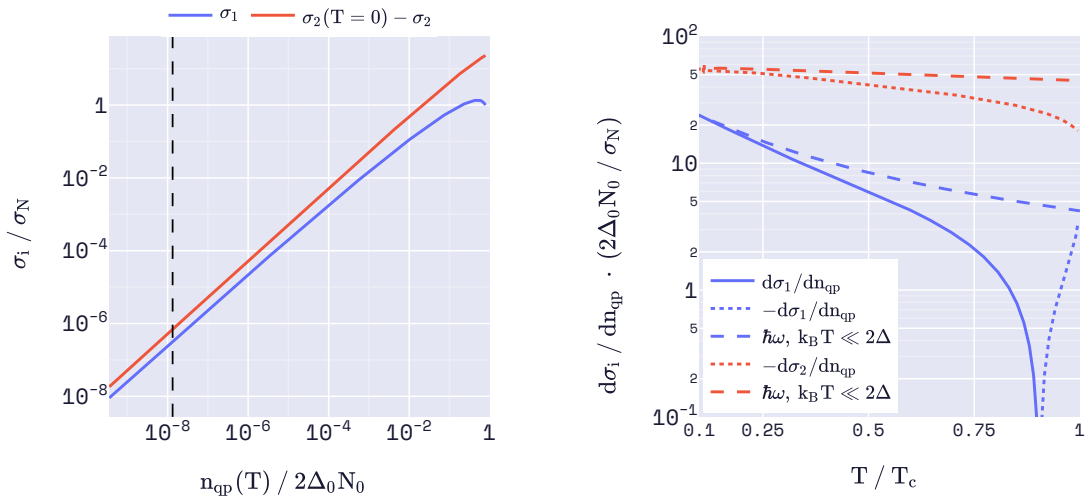

(a) **(b)**

Figure 2.4 – **(a)** Complex conductivity as a function quasiparticle density. A vertical dashed line is added to show the density for $T = T_c/10$. **(b)** $d\sigma/dn_{qp}$ as a function of temperature. Dashed coloured lines are added for approximations determined for $\hbar\omega, k_B T \ll 2\Delta$. For both figures $\rho_N = 49\mu\Omega{\cdot}$cm, $T_c = 0.6$K, and $f = f_c/10$ are used.

For a superconducting film of thickness d on top of a substrate, of which the latter has a significantly large impedance, we can relate the complex conductivity to its corresponding sheet impedance [49],

$$Z_s = R_s + jX_s = \sqrt{\frac{j\mu_0\omega}{\sigma_1 - j\sigma_2}} \coth\left(d\sqrt{j\mu_0\omega(\sigma_1 - j\sigma_2)}\right). \tag{2.8}$$

From the sheet reactance, we derive the definition for sheet kinetic inductance[3], $L_{k,s} = X_s/\omega$. The sheet impedance for a superconducting film as a function of both frequency and temperature is shown in figure 2.5.

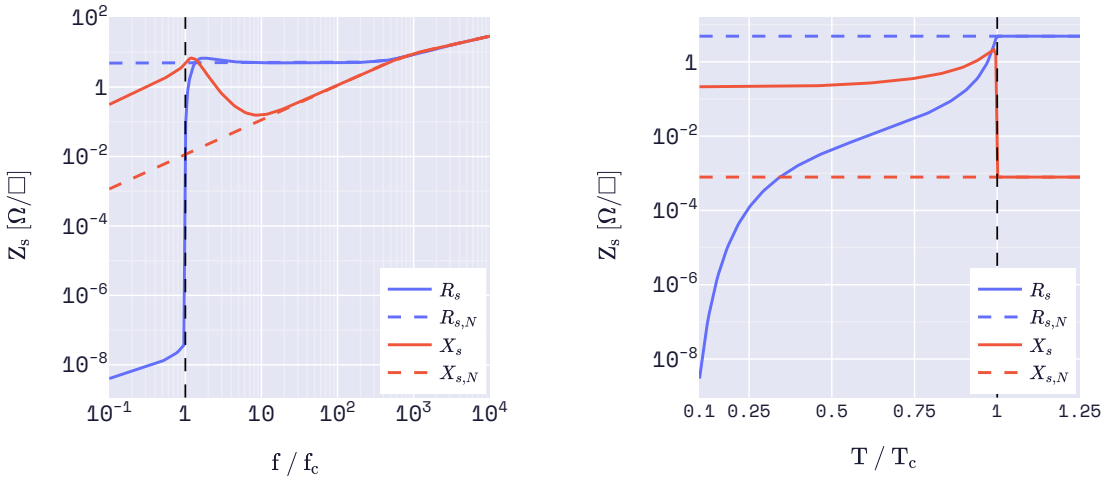

(a) **(b)**

Figure 2.5 – Sheet impedance as a function of **(a)** frequency (at $T = T_c/10$) and **(b)** temperature (at $f = f_c/10$) for a superconducting film with $T_c = 0.6$K, $\rho_N = 49\mu\Omega{\cdot}$cm and $d = 40$nm. The dashed lines represent the sheet impedance for the normal metal equivalent. The normal state sheet resistance converges to $R_{s,N} = \rho_N/d$ for low frequencies.

[3]The term 'kinetic inductance' is used, as the inductive behavior caused by the Cooper pairs is associated with the momentum of the superconducting electrons (with mass m_e) bound in Cooper pairs. Namely, their total kinetic energy can be directly related to the magnetic energy stored in an inductor through $\frac{1}{2}(2n_s V \cdot m_e)v^2 = \frac{1}{2}L_k I^2$, where $2n_s$ is the Cooper pair number density in a volume V relating to a superconducting current I [50].

2.2. Superconducting microwave resonators as detectors

To employ the change in complex conductivity when Cooper pairs are broken, we can use superconductors to build a microwave resonator circuit. Change in the complex conductivity will then result in a change of the resonator's properties, effectively making it a pair-breaking detector. We can multiplex detectors in frequency space, by designing them at different resonance frequencies and capacitively coupling each of them to a single readout line.

2.2.1. Coplanar waveguides as transmission lines

To build the microwave resonator, we use coplanar waveguides (CPWs), as their geometry is both easy to fabricate and we can accurately describe their microwave properties. A CPW is made by etching two parallel slots in a superconducting film deposited on top of a dielectric substrate. This creates a center line separated from two semi-infinite ground planes by two slots. We can also replace the center line by a different superconducting film to achieve a hybrid structure, of which an example is shown schematically in figure 2.6.

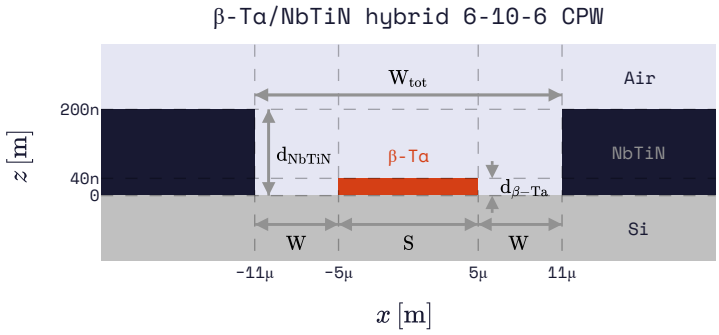

Figure 2.6 – Schematic cross section of a hybrid coplanar waveguide. This CPW is made by making two slots of width W in a NbTiN film of thickness 200nm on a Si substrate. A β-Ta film of thickness 40nm is then deposited to make a center line of width S, making the CPW structure hybrid.

For the electromagnetic field traveling along a CPW, the geometric effective relative permittivity $\epsilon_{\text{eff,geo}}$ can be accurately approximated for thick substrates by the mean of the relative permittivities of the substrate and vacuum surrounding it,

$$\epsilon_{\text{eff,geo}} \approx \frac{1+\epsilon_r}{2}, \tag{2.9}$$

where ϵ_r is the relative permittivity of the substrate. Using this $\epsilon_{\text{eff,geo}}$, we can find the geometric contributions to the capacitance $C_{g,l}$ and inductance $L_{g,l}$, both per unit length [51],

$$C_{g,l} = 4\epsilon_0\epsilon_{\text{eff,geo}}\frac{K(k)}{K(\sqrt{1-k^2})}, \tag{2.10}$$

$$L_{g,l} = \frac{\mu_0}{4}\frac{K(\sqrt{1-k^2})}{K(k)}, \tag{2.11}$$

where K is the complete elliptical integral of the first kind, and $k = \frac{S}{S+2W}$ using S as the width of the central line and W the width of each slot. While the total capacitance per unit length solely consists of the geometric contribution, such that $C_l = C_{g,l}$, we have to take the kinetic inductance of the superconductors into account when evaluating the total inductance per unit length[4]. For this, we consider geometric contributions of the central line g_c and the ground planes g_g, accurate for $d < S/20$ and $W > 0.3S$ [51],

$$g_c = \left(\pi + \ln\frac{4\pi S}{d_g} - k\ln\frac{1+k}{1-k}\right) / \left(4S(1-k^2)K(k)^2\right), \tag{2.12}$$

$$g_g = \left(\pi + \ln\frac{4\pi(S+2W)}{d_c} - \frac{1}{k}\ln\frac{1+k}{1-k}\right) / \left(4S\frac{1-k^2}{k}K(k)^2\right), \tag{2.13}$$

where d is used for the respective film thicknesses.

[4]We have only considered the geometric contribution to the effective relative permittivity. The effect of the kinetic inductance on the effective relative permittivity is elaborated on in Appendix C.

The geometric contributions allow us to find the expressions for total resistance and inductance per unit length,

$$R_l = g_c R_{s,c} + g_g R_{s,g}, \tag{2.14}$$
$$L_l = g_c L_{k,s,c} + g_g L_{k,s,g} + L_{g,l} = L_{k,l} + L_{g,l}, \tag{2.15}$$

from which we use the latter to derive the kinetic inductance fraction α_k,

$$\alpha_k = \frac{L_{k,l}}{L_l} = \frac{L_{k,l}}{L_{k,l} + L_{g,l}}. \tag{2.16}$$

To better analyze a CPW, it is useful to represent it by a transmission line with a characteristic impedance Z_0, propagation constant γ, and a length l[5]. Here, we define the characteristic impedance as [52],

$$Z_0 = \sqrt{\frac{R_l + j\omega L_l}{G_l + j\omega C_l}}. \tag{2.17}$$

and the complex propagation constant as [52],

$$\gamma = \alpha + j\beta = \sqrt{(R_l + j\omega L_l)(G_l + j\omega C_l)}. \tag{2.18}$$

where R_l is the series resistance per unit length of the line, G_l the shunt conductance per unit length due to dielectric loss, L_l the series inductance per unit length, and C_l the shunt capacitance per unit length [52].
The real part of the propagation constant determines the exponential decay of a wave propagating on the transmission line. We can therefore define attenuation as power loss over unit length in the transmission line through α,

$$\text{attenuation} = -\alpha \cdot 20\log_{10}(e). \tag{2.19}$$

where we multiply by $20\log_{10}(e)$ to convert the units of α from Np/m to dB/m. If $\hbar\omega < 2\Delta$, the attenuation is small for superconductors ($R_l \ll \omega L_l$ and $G_l \ll \omega C_l$), see figure 2.5. The imaginary part of the propagation constant, β, determines the phase velocity and thus the wavelength of a propagating wave,

$$v_{\text{phase}} = \lambda f = \frac{\omega}{\beta}. \tag{2.20}$$

We can now continue to use the formalism of transmission lines with Z_0 and γ and a finite length l, by considering a terminated transmission line (see figure 2.7). Its input impedance Z_{in} can be determined by [52],

$$Z_{in} = Z_0 \frac{Z_L + Z_0 \tanh\gamma l}{Z_0 + Z_L \tanh\gamma l}, \tag{2.21}$$

where Z_L represents the load impedance at termination. There are two special cases for the input impedance, namely when the transmission line has either a shorted or open load,

$$Z_{in} = \begin{cases} Z_0 \tanh\gamma l, & \text{if } Z_L = 0 \text{ (shorted)} \\ Z_0 \coth\gamma l, & \text{if } Z_L = \infty \text{ (open)} \end{cases} \tag{2.22}$$

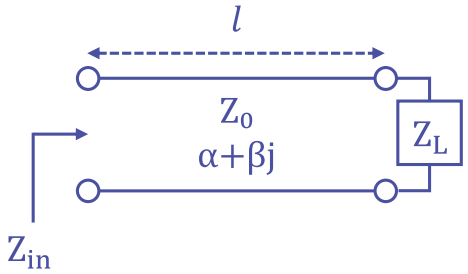

Figure 2.7 – Schematic circuit representation of a terminated transmission line with characteristic impedance Z_0 and a complex propagation constant $\gamma = \alpha + j\beta$. Equivalent input impedance at distance l from its termination in the load impedance Z_L is indicated by Z_{in}.

[5]Transmission line theory used in this thesis is elaborated on in Appendix D.

2.2.2. Quarter-wave resonator

For a terminated transmission line to become a resonator, a wave traveling inside of it needs to be able to reflect at the termination. Consequently, the incident wave and the reflected wave can interfere to form a standing wave. This effect of resonance takes place when the input impedance Z_{in} becomes real (equivalently, zero reactance). This reduces to the following resonance condition for a resonance frequency f_0 [53],

$$\mathrm{Im}\{Z_{in}(f_0)\} = 0. \tag{2.23}$$

For a shorted load and a length $l = \lambda/4$, a standing wave will have an antinode at termination to form a quarter-wave resonator. This makes it simple to approximate the resonance frequency as $f_{1/4} \approx 1/(4\sqrt{LC})$ for small attenuation using equation 2.20.
For the quarter-wave resonator, we can rewrite the expression for a shorted transmission line (equation 2.22),

$$Z_{in}^{\mathrm{res}} = Z_0 \tanh(\alpha l + j\beta l) = Z_0 \frac{1 - j\tanh\alpha l \cot\beta l}{\tanh\alpha l - j\cot\beta l}. \tag{2.24}$$

If we now pick frequencies close to the quarter-wave resonance frequency $f_{1/4}$, for which the resonance condition holds, we can write $\beta l = \frac{2\pi}{4}(1 + \frac{\omega-\omega_{1/4}}{\omega_{1/4}})$. Considering small α and only using small changes $\frac{\omega-\omega_{1/4}}{\omega_{1/4}} \ll 1$, we can approximate the input impedance to find [52, 53],

$$Z_{in}^{\mathrm{res}} \approx Z_0 \frac{1}{\alpha l + j\frac{\pi}{2}\frac{\omega-\omega_{1/4}}{\omega_{1/4}}} = Z_0 \frac{\frac{4}{\pi}Q_i}{1 + 2jQ_i\frac{\omega-\omega_{1/4}}{\omega_{1/4}}}, \tag{2.25}$$

where we substituted the internal quality factor Q_i to represent energy lost through dissipation. We define Q_i as [52],

$$Q_i = \frac{\beta}{2\alpha}. \tag{2.26}$$

To be able to detect changes in the resonator's properties, we capacitively couple it to a readout line. To determine the amount of power lost from the resonator to the readout line through the capacitor, we introduce the coupling quality factor Q_c [43],

$$Q_c = \frac{\pi}{2\left(\omega_{1/4} C_c \sqrt{Z_0 Z_0^{\mathrm{readout}}}\right)^2}, \tag{2.27}$$

where C_c is the coupler capacitance and Z_0^{readout} the characteristic impedance of the readout line.
We can now use figure 2.8 to consider the input impedance of the resonator as seen from the readout line. The coupler capacitance is put in series with the resonator, such that $Z_{in} = 1/(j\omega C_c) + Z_{in}^{\mathrm{res}}$. Note that the coupler capacitance will change the resonance condition of the quarter-wave resonator, changing the resonance frequency $\omega_{1/4}$ slightly to a new, lower, resonance frequency ω_0 [53].

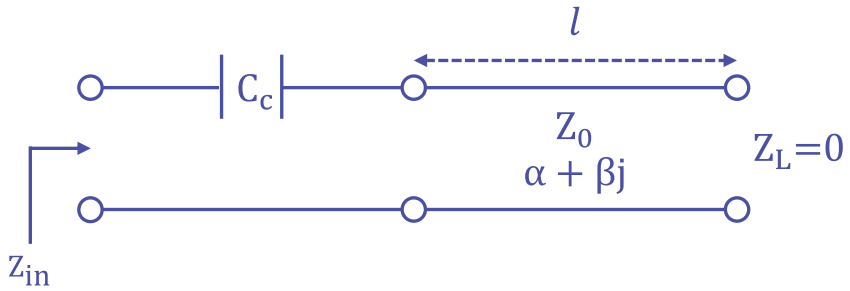

Figure 2.8 – Schematic circuit representation of a quarter-wave resonator, consisting of a capacitor in series with a transmission line with a shorted termination. The input impedance is shunted to a readout line.

As the quarter-wave resonator is coupled in shunt to the readout line, we can use figure 2.9 to represent a section of the readout line. We evaluate the forward transmission between its ports 1 and 2 for small changes $x = \frac{\omega-\omega_0}{\omega_0} \ll 1$ to find [52, 53],

$$S_{21} = \frac{2}{2 + Z_0^{\mathrm{readout}}/Z_{in}} \approx \frac{Q_l/Q_i + 2jxQ_l}{1 + 2jxQ_l}, \tag{2.28}$$

where we combine Q_i and Q_c to define the loaded quality factor,

$$\frac{1}{Q_l} = \frac{1}{Q_i} + \frac{1}{Q_c}. \tag{2.29}$$

The relation of Q_l, Q_i, and Q_c is visualized in figure 2.10a.

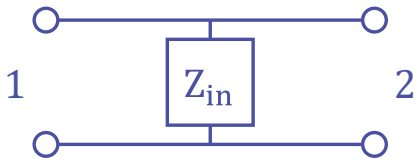

Figure 2.9 – Schematic circuit representation of the input impedance of the resonator, coupled in shunt to the readout line.

In figure 2.10b, we see that the forward transmission S_{21} forms a circle in the complex plane: its radius defined as $r = Q_l/(2Q_c)$, and its center lying on the real axis at $\mathrm{Re}\{S_{21}\} = 1 - r$. The magnitude and phase of S_{21} are shown in figure 2.10c and 2.10d, respectively. The magnitude $|S_{21}|$ creates a Lorentzian profile, for which we can define its linewidth as the full-width at half-maximum ω_0/Q_l. We can use the resonator circle, Lorentzian dip, and changes in phase to characterize the properties of the superconducting microwave resonator.

2.2.3. Detector responsivity

In equations 2.6 and 2.7, we saw how the complex conductivity changes under change of quasiparticle density. This will in turn change both the internal quality factor (through change in R_s), and the resonance condition and thus the resonance frequency (through change in L_s) of the resonator.
From the notion that $\omega_0 \propto 1/\sqrt{L_l C_l}$, we can calculate the change in resonance frequency to first order using equation 2.8 for thin films [43],

$$\frac{\delta\omega_0}{\omega_0} \approx -\frac{\alpha_k}{2}\frac{\delta L_s}{L_s} \approx -\frac{\alpha_k}{2}\frac{\delta\sigma_2}{\sigma_2}, \tag{2.30}$$

where δ denotes a small change. Similarly, for Q_i, we can derive from equation 2.26 [54],

$$Q_i = \frac{\omega L}{R} = \frac{\omega L_{k,s}}{\alpha_k R_s} = \frac{1}{\alpha_k}\frac{\sigma_2}{\sigma_1}, \tag{2.31}$$

to find,

$$\delta\Big(\frac{1}{Q_i}\Big) \approx \alpha_k \frac{\delta\sigma_1}{\sigma_2} \tag{2.32}$$

Using the observation that S_{21} maps to the circle $[\mathrm{Re}\{S_{21}\} - (1-r))]^2 + [\mathrm{Im}\{S_{21}\}]^2 = r^2$ in the complex plane, we translate to a new coordinate system. For this, we define an amplitude A, for which we use the distance to the center of the circle normalized to its radius, and shift it to be 0 at the designed resonance [54],

$$A = 1 - \frac{\sqrt{[\mathrm{Re}\{S_{21}\} - (1-r))]^2 + [\mathrm{Im}\{S_{21}\}]^2}}{r}, \tag{2.33}$$

and a phase θ, defined as the angle made with the negative real axis as seen from the center of the circle [54],

$$\theta = \tan^{-1}\Big(\frac{\mathrm{Im}\{S_{21}\}}{(1-r) - \mathrm{Re}\{S_{21}\}}\Big). \tag{2.34}$$

A and θ relate to change in quasiparticle density through frequency shift and change in the internal quality factor, respectively. We derive their derivatives for thin films [43],

$$\frac{dA}{dn_{qp}} \approx 2Q_l\frac{d(1/Q_i)}{dn_{qp}} \approx 2\frac{\alpha_k Q_l}{\sigma_2}\frac{d\sigma_1}{dn_{qp}}, \tag{2.35}$$

$$\frac{d\theta}{dn_{qp}} \approx -4Q_l\frac{d(\delta\omega_0/\omega_0)}{dn_{qp}} \approx -2\frac{\alpha_k Q_l}{\sigma_2}\frac{d\sigma_2}{dn_{qp}}, \tag{2.36}$$

where we take $T \ll T_c$ and assume that $Q_l \approx Q_c$ such that Q_l is constant.
From the equations for amplitude response (equation 2.35) and phase response (equation 2.36), we see that A probes dissipation (through σ_1) and θ probes kinetic inductance (through σ_2). Therefore, A and θ form appropriate observables for our Kinetic Inductance Detector (KID).

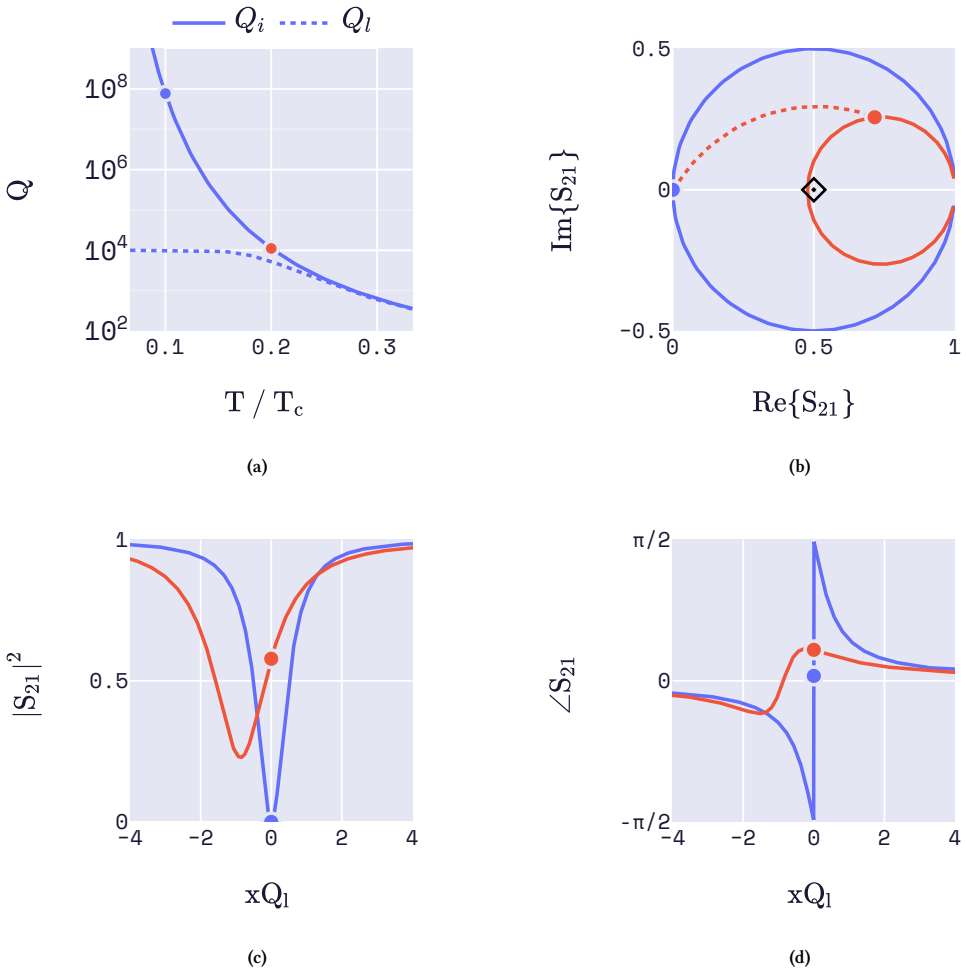

Figure 2.10 – Response of a superconducting microwave resonator to a change in quasiparticle number density. **(a)** The internal quality factor Q_i as a function of temperature. Increasing the temperature increases the number of thermal quasiparticles, therefore lowering Q_i. A coupling quality factor $Q_c = 10^4$ was chosen to dominate the loaded quality factor Q_l at low temperatures. **(b)** The resonator's forward transmission mapped onto the complex plane. The blue curve represents the resonator for frequencies close to its resonant frequency $f_0/f_c = 0.1$ at $T/T_c = 0.1$. The transmission on resonance is indicated using the blue marker, and the center of the resonator circle using the black diamond shape. The red curve represents the resonator for an increase in quasiparticle number equivalent to an increase in temperature to $T/T_c = 0.2$. The red dotted line traces the forward transmission at the design resonance frequency as the quasiparticle number increases, to end at the red marker. For these calculations, we use β-Ta ($T_c = 0.06$K and $\rho = 210\mu\Omega$·cm) and NbTiN ($T_c = 15$K and $\rho = 49\mu\Omega$·cm), and consider the CPW dimensions of figure 2.6. **(c)** and **(d)** show the squared magnitude and the argument for the same two curves as in (b), respectively. Both are plotted as a function of xQ_l.

2.2.4. Noise and losses in a Kinetic Inductance Detector

Thus far, we have only considered an idealized microwave resonator for which thermal equilibrium results in the resonator's properties to be constant. However, there are several sources that cause fluctuations in the response of a KID. We discuss the most important sources of these fluctuations and additional microwave losses.

Generation-recombination noise

Thermal phonons can randomly break Cooper pairs in a superconductor. So, while the time-averaged quasiparticle density can be found through equation 2.1 in thermal equilibrium, when generation and recombination rates are equal, the actual thermal quasiparticle density thus fluctuates over time. The corresponding noise-equivalent power (NEP[6]) of these quasiparticle number fluctuations is defined as [55],

$$\mathrm{NEP}_{\mathrm{g-r}} = \frac{2\Delta}{\eta_{pb}}\sqrt{\frac{N_{qp}^T}{\tau_{qp}}}, \tag{2.37}$$

[6]The noise-equivalent power states the minimum signal power per unit bandwidth to match the power of the noise.

where η_{pb} is the pair-breaking efficiency of pair-breaking photons and τ_{qp} the quasiparticle lifetime. The generation-recombination NEP can be reduced by a reduction in the amount of excess quasiparticles, or by an increase in quasiparticle recombination time [56, 57].

Two-Level-System noise

During fabrication, oxides and other amorphous solids can form on the metal and dielectric surfaces of the resonator's materials. These amorphous solids may contain defects that give rise to two-level systems (TLSs). In a TLS, an atom can be modeled to reside in a double-well potential, where the atom can tunnel between the two minima. These minima differ in energy, such that these random tunneling events cause time-dependent variations in the dielectric constant of the resonator's materials [58]. TLSs cause fluctuations in the resonance frequency and induce additional microwave losses. This noise is primarily visible as $1/f$-noise in the phase response [59].
A way to reduce TLS noise is to increase the total width of the CPW, as it results in more of the electric field being in the vacuum instead of being inside of the amorphous solids [60, 61]. TLSs can also be minimized by using a metal that does not oxidize well, for which Niobium Titanium Nitride (NbTiN) proves to be a good candidate [62, 63].

Amplifier noise

The instruments in a readout system, such as amplifiers and attenuators, give rise to white noise. We can use an equivalent noise temperature of the system T_{sys} to model these noise sources as thermal noise, which we collectively call amplifier noise [50]. Amplifier noise is primarily seen in the amplitude response.

Photon noise

The fundamental limit of a KID used to detect photon radiation, is the noise induced by fluctuations in the photon arrival rate. The noise-equivalent power corresponding to photon noise reads [44, 64],

$$\mathrm{NEP}_{\mathrm{ph}} = \sqrt{2P_{rad}\hbar\omega(1+mB)}, \tag{2.38}$$

where P_{rad} is the absorbed power of the radiation with energy $\hbar\omega$. The term $(1+mB)$ is the correction to the Poisson statistics due to photon bunching [44]. Photon noise is constant over frequency, and is therefore observed as a form of white noise. Ideally, a detector is optimized such that the photon noise limits the total noise-equivalent power, and is then said to have photon-noise-limited performance.

2.2.5. Hybrid Kinetic Inductance Detector

Thus far, we have only considered a microwave resonator built from a single CPW structure. It is highly convenient, however, to combine two connected CPWs in a hybrid KID design.

By carefully choosing two different superconductors with significantly different critical temperatures, the pair-breaking energy will differ for both. Photons with an energy between the two pair-breaking energy levels will therefore only be able to break Cooper pairs within the superconductor with the lower T_c. Consequently, these quasiparticles can only exist within this lower-gap superconductor, and will be confined to its (active) volume; they are effectively trapped by the Andreev barrier due to the difference in gap energies [65].

In previous sections, we considered the effect of quasiparticles to be uniform throughout the entire superconductor. However, the response due to change in quasiparticle density is position dependent, weighted by the square of the current distribution within the resonator [53].
TLS noise is dependent on the electric field driving the tunneling events, and it has a larger contribution on the open end of the resonator. As mentioned in section 2.2.4, TLS noise and losses are suppressed for larger structures, so it is therefore advantageous to use a particularly wide CPW on the open end [61].
The current distribution results in a quarter-wave resonator to be more responsive at its shorted end. For this reason, this end is best to place the lower-gap superconductor to guide pair-breaking photons to [53]. This is also practical for coupling an antenna as a load to make an antenna-coupled KID. In chapter 3, we look at a design method of such an antenna-coupled KID.

Quasiparticles should be confined to a smaller active volume in the detector to increase responsivity, thus requiring the CPW at the shorted end to be narrow. This way, a change in quasiparticle number N_{qp} will lead to a larger change in quasiparticle density n_{qp}. Microwave readout power leads to more excess quasiparticles

in a smaller active volume V [56, 66]. These excess quasiparticles limit the sensitivity, which can only be improved by reducing $\sqrt{V\omega_0}/(Q_l\alpha_k)$ in the KID design and TLS-noise simultaneously [66]. By selecting a superconductor with a large normal state resistivity ρ_N as the lower-gap superconductor, one yields a larger kinetic inductance L_k (see equation 2.8). In that case, the active volume can be reduced while keeping α_k high [30].

In the hybrid KIDs used in this thesis, the wide CPW will be made from the low-noise NbTiN for reduction in TLS noise [62]. With its large normal state resistivity, β-phase Tantalum (β-Ta) is a good candidate for the lower-gap superconductor [32].

2.3. Disordered superconductors

While we have thus far discussed the theory for superconductors based on the description provided by BCS and MB-theory, this only accurately describes superconductivity for weak-coupling superconductors.
For the class of materials that are called disordered superconductors, localization effects due to defects or impurities in their ionic lattice start to play a role in their superconductivity. The gap energy is no longer only dependent on temperature, but also on position in space, which means that we cannot consider a homogeneous gap energy and density of states [67, 68]. Their superconducting state becomes increasingly inhomogeneous for increasing disorder [69]. β-Ta is an example of a disordered superconductor [32].
These local gap inhomogeneities serve as localization sites for the quasiparticles. Absorption of a phonon can delocalize a quasiparticle, after which it can relax and rapidly recombine with another quasiparticle (see figure 2.11). Quasiparticles recombination is thus governed by phonon scattering, which is faster than conventional recombination in ordered superconductors. While this reduces the recombination time of excess quasiparticles, it does induce additional microwave loss and limits the responsivity at low temperature [38]. Namely, for low temperatures, the excess quasiparticles can stay localized, being effectively trapped. By increasing temperature or radiation power, one can convert these quasiparticles from being trapped to being insensitive to the underlying gap inhomogeneity, effectively transitioning to a homogeneous material [69].

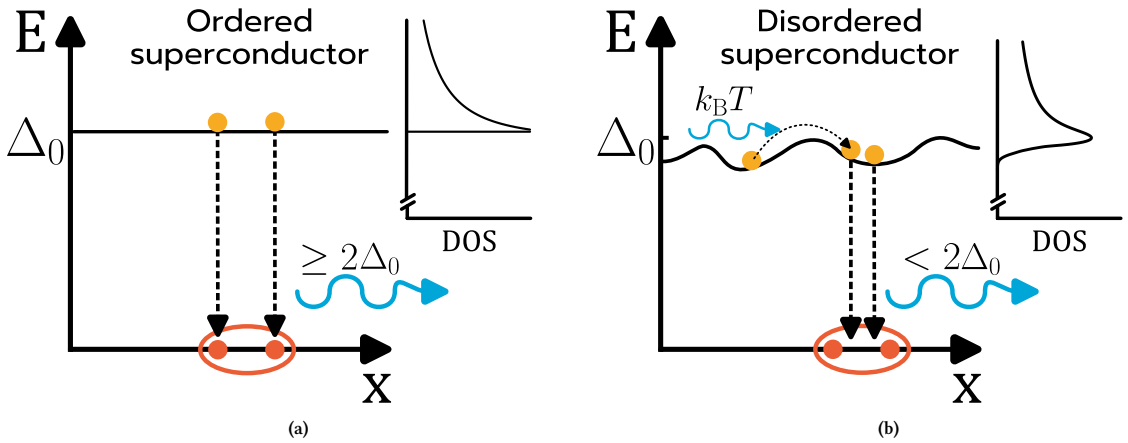

Figure 2.11 – **(a)** Schematic representation of quasiparticle recombination according to BCS, where the phonon with energy $E \geq 2\Delta_0$ emitted can subsequently break a different Cooper pair. The inset shows the BCS density of states, sharing the energy axis with the schematic. **(b)** Schematic representation of quasiparticle recombination in disordered superconductors, where disorder suppresses the energy gap locally. Absorption of a phonon can delocalize a quasiparticle, after which it recombines on-site, emitting a phonon with energy $E \leq 2\Delta_0$. Figures adapted from [38].

While disorder has some implications, their typically high normal state resistivity, causing a high kinetic inductance in their superconducting state, allows for different impedance regimes than ordered superconductors [43]. There is no full description of the density of states of disordered superconductors yet. That is why we will still use the BCS density of states and thus the description provided by MB-theory (equations 2.2 and 2.3) to approximate the complex conductivity of β-Ta in this thesis.

3

Design methods

In this chapter, we cover the methods used to design lens-antenna coupled hybrid KIDs. This type of KID uses a lens antenna to couple incoming radiation to the detector. This allows for mitigation of the reduced sensitivity associated with the disorder of β-Ta through reduction in active volume, as was discussed in chapter 2.
We split this design process in different parts. First, we consider the design of the lens antenna in section 3.1. Next, the essence of impedance matching is discussed in section 3.2. This chapter concludes by looking at how the hybrid KIDs coupled to the antenna can be modeled in section 3.3.

3.1. Lens antenna

To achieve efficient radiation coupling between a source of pair-breaking photons and the antenna, we can use a lens to focus the radiation to the antenna. This section looks into the design of such a lens antenna. We start with the choice of a twin-slot antenna and extended hemispherical lens, and conclude by describing the method used to define their combined performance through beam-pattern analysis.

3.1.1. Twin-slot antenna

For the antenna, we choose to use the simple geometry of a twin-slot antenna. Its planar structure can be made on the front side of a monolithic Silicon (Si) wafer within the NbTiN film used as the ground planes for the CPWs of our detectors. A twin-slot antenna tends to radiate most of its power into the dielectric side of it, which is toward the Si substrate, given its high relative permittivity [70].

For the design and analysis of the twin-slot antenna, we use a setup with open boundary conditions in CST [71]. This setup is shown in figure 3.1a. Altering the dimensions of the antenna result in changes in its characteristics. We define five different parameters (see figure 3.1b), which can be used to optimize the antenna dimensions.

The size of the antenna directly scales with the frequencies it will be sensitive to, making the slot length L_{ant} and slot spacing W_{ant} directly scale with it. That is why we choose to parametrize the antenna's dimensions with respect to the wavelength in vacuum. From this, we derive $L_{ant} = c_1\lambda$ and $W_{ant} = c_2\lambda$. We choose to scale the smaller three dimension parameters with respect to L_{ant} through $W_1 = c_3 L_{ant}$, $W_2 = c_4 L_{ant}$, and $d_{ant} = c_5 L_{ant}$. This way, we can easily scale a design to different design frequencies while keeping all constants c_i the same. We use the design by Filipovic et al. [70] as our starting point and take $L_{ant} = 0.28\lambda$, chosen to maximize the current within the slots, and $W_{ant} = 0.16\lambda$.

3.1.2. Extended hemispherical lens

As we stated that the antenna will have most power coupling toward the side of the substrate, we can conveniently achieve efficient radiation coupling from the lens to the antenna by mounting the lens on the back side of the wafer. We can subsequently use a monolithic Si lens that can be designed to have the antenna in its focus. In this thesis, we use an extended hemispherical lens to synthesize the shape of an elliptical lens.

An extended hemispherical lens has a hemispherical geometry with radius R_{sphere} and an extension chosen to closely recreate the properties of an elliptical lens. These properties entail rays being bent to the broadside

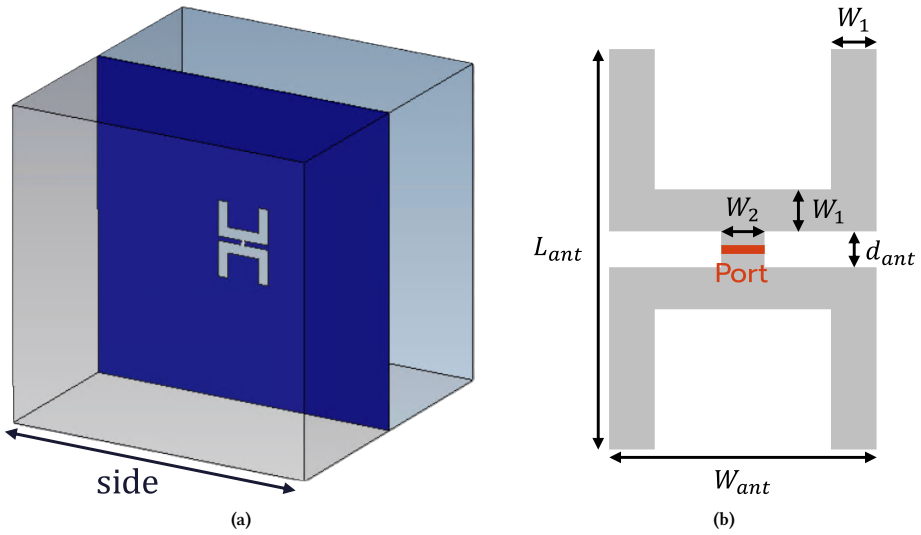

Figure 3.1 – Overview of the setup used to optimize the dimensions of a twin-slot antenna. **(a)** Setup used in CST. A film of NbTiN (dark blue) is contained within the simulated box, a cube with open boundary conditions. On one side, there is Si substrate with $\epsilon_r = 11.44$ (gray and transparent), and on the other side, there is vacuum with $\epsilon_r = 1$ (light blue and transparent). The feed of the antenna is at the center of the antenna, and is thus centered in the cube. The corresponding port is chosen such that its dimensions match that of the narrow CPW. The positive z-axis is defined toward the Si layer. For NbTiN, we use $L_{k,s} = 1.08$pH. **(b)** Definitions of the five parameters defining the dimensions of a twin-slot antenna. The port (orange) is located in the center of the antenna. The port resembles the center line of the narrow CPW which is shorted to ground on one side and connects to the rest of the KID on the other side.

direction of the antenna to obtain a sharpened beam pattern, and the absence of spherical aberrations such that all incident rays focus to one point. The twin-slot antenna should then ideally be in the focus of the lens. This results in the far-field pattern of the antenna to be diffraction limited by the aperture of the lens [70].

The aperture of the lens is defined by a diameter D, which creates a cone with angle θ_0 to the focus of the lens. To increase the optical coupling of the lens antenna, one can adjust the geometry of the lens such that θ_0 matches the beamwidth of the antenna. This way, we can consider the entire main beam to illuminate the lens surface. We define the beamwidth as the angle for which the main beam of the antenna reaches -10dB.

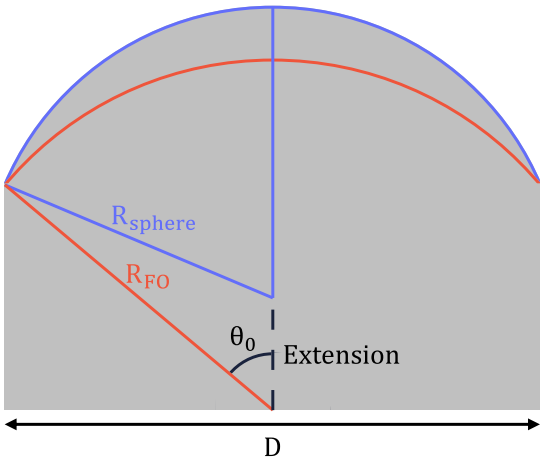

Figure 3.2 – Geometry of an extended hemispherical lens. D denotes the diameter of the aperture of the hemisphere with radius R_{sphere}. The extension length can be chosen such that the lens synthesizes the shape of an elliptical lens. In that case, the focus of the lens is at the center of the sphere with radius R_{FO}, where the antenna is placed. θ_0 then defines the opening angle of the lens aperture.

3.1.3. Beam pattern

It is important to evaluate the beam pattern of the combined lens and antenna, as it gives us insight in how the antenna in our KID will couple to a source. We can simulate the far-field beam pattern of the antenna design using CST (see figure 3.1). In the far field, any spherical waves radiated by a source can be considered to propagate as plane waves. The obtained far field can then be used to evaluate how the beam pattern changes if a lens is added to it. For this, we will use a Physical Optics (PO) technique.

The PO technique uses the reciprocity theorem, which states that the response of a system to a source is equivalent when evaluated in either transmission (Tx) or reception (Rx) modes [72, 73]. We opt for the use of a PO tool in Tx that allows us to directly determine the far field at any distance from the top of a (synthesized) elliptical lens [74]. We can also use the PO tool to check whether the lens and antenna are properly optimized. Namely, we can extract common efficiency terms from its results.

The directivity in a certain direction quantifies how much the lens antenna radiates in that direction with respect to an isotropic source (for which radiation is uniform in all directions). From the maximum obtainable directivity $Dir^{\max}$ and the achieved directivity $Dir^{\text{lens}-\text{antenna}}$, we find the taper efficiency [73],

$$\eta_{tap} = \frac{Dir^{\text{lens}-\text{antenna}}}{Dir^{\max}}. \tag{3.1}$$

The fraction of incoming power (P_{in}) reaching the lens that actually gets absorbed by the antenna (P_{abs}) is defined as the aperture efficiency [73],

$$\eta_{ap} = \frac{P_{abs}}{P_{in}}. \tag{3.2}$$

Combining taper efficiency and aperture efficiency, we yield an expression for the fraction of total power directed to the antenna as opposed to spilling over, or the spillover efficiency [73],

$$\eta_{so} = \frac{P_{abs}/Dir^{\text{lens}-\text{antenna}}}{P_{in}/Dir^{\max}} = \frac{\eta_{ap}}{\eta_{tap}}. \tag{3.3}$$

Together, these three efficiencies quantify the performance of the lens antenna.

3.2. Impedance matching

The narrow CPW within the hybrid KID is connected to the feed of the antenna. We can therefore interpret the input impedance of the antenna to be the load impedance of the terminated transmission line shown in figure 3.3. As the sole purpose of the antenna is to inject pair-breaking radiation into the β-Ta film, it is important that the coupling between these two circuit elements is optimal. To interpret the respective coupling efficiency, we look at the level of mismatch in impedance between the two.
For a voltage wave traveling on a transmission line with a characteristic impedance Z_0, the voltage reflection coefficient at a load impedance Z_L is known to be [52],

$$\Gamma_v = \frac{Z_L - Z_0}{Z_L + Z_0}. \tag{3.4}$$

We observe that $Z_L = Z_0$ is required for minimal voltage wave reflections. For a power wave, the reflection coefficient is defined differently [75],

$$\Gamma_p = \frac{Z_L - Z_0^*}{Z_L + Z_0}. \tag{3.5}$$

For maximal power transfer, we thus have to consider a conjugate match ($Z_L = Z_0^*$). We define $|\Gamma_p|^2$ as the fraction of power reflected, and, equivalently, $1 - |\Gamma_p|^2$ the fraction of power transmitted. The latter is what we use to define the coupling efficiency. These expressions are used to evaluate whether power from the antenna will be able to transmit efficiently to the narrow CPW.

While we approached this through the impedance match between the antenna and the narrow CPW at pair-breaking frequencies, this also applies to any set of circuit element at readout frequencies: from the transmission lines in the detector to coaxial cables in the readout system in an experimental setup. Any impedance mismatch would cause undesired reflection within the detector. In fact, an optimal design is found when all elements are impedance matched at readout frequencies, for which Z_0 is typically real-valued such that one can use equation 3.4. Normally, this is solved by designing all components at the same characteristic impedance of 50Ω at readout frequencies, as this is the standard for coaxial cables used in an experimental setup.

3.3. Modeling an antenna-coupled KID

For the design of our antenna-coupled KIDs, we want to be able to analyze their properties at different temperatures and for different design parameters. We do so using two different methods.

Using network analysis

For the design of a hybrid KID, we use the transmission line representation shown in figure 3.3. The equivalent circuit network of the KID is then formed by cascading the equivalent transmission matrices[1] of the different circuit elements. We acquire their properties using the Mattis-Bardeen equations and description of CPWs from chapter 2. We can subsequently find the forward transmission S_{21} of the KID by using the network's input impedance in the circuit that was shown in figure 2.9.

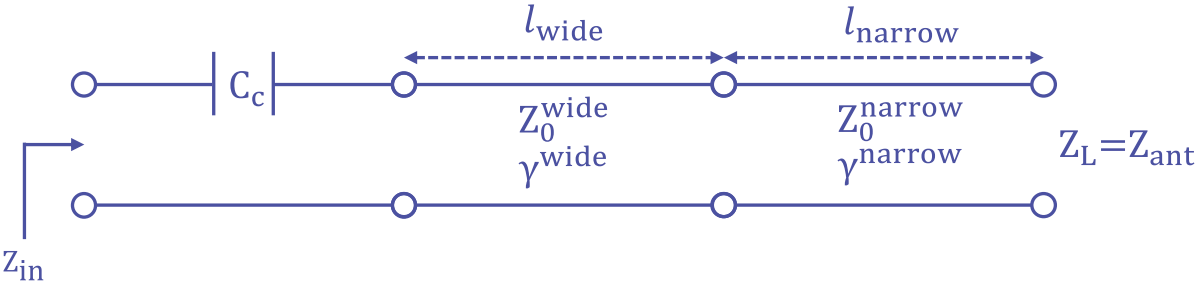

Figure 3.3 – Schematic circuit representation of a hybrid KID consisting of a wide and narrow CPW. The sensitive narrow CPW is terminated in the antenna, functioning as the load. Pair-breaking photons can be injected in the sensitive low-gap superconductor from this antenna. The narrow CPW is placed in series with a wide CPW and a capacitor, through which the resonator is coupled to a readout line. The total length $l_{wide} + l_{narrow}$ can be tuned through the resonance condition to design the resonator at different resonance frequencies.

Using an EM-solver

To show that we can accurately model the quarter-wave hybrid resonators using the theory discussed in chapter 2, antenna-coupled KID structures can be simulated using Sonnet [76]. A schematic representation of the structure used in Sonnet is shown in figure 3.4. We perform such a simulation in two parts. The first contains the open end of the resonator structure, coupled to the readout line using a coupler. For the shorted end, we place a component in Sonnet containing the simulation result of the second part. The second part contains the narrow CPW with the antenna structure at its termination. We keep the length of the narrow CPW fixed, such that we can reuse the simulation result of the second part when varying the length of the wide CPW or the coupler. The advantage of using the EM-solver over the network analysis method is that it can more accurately simulate the properties of the CPW and antenna structures, at the cost of computation time.

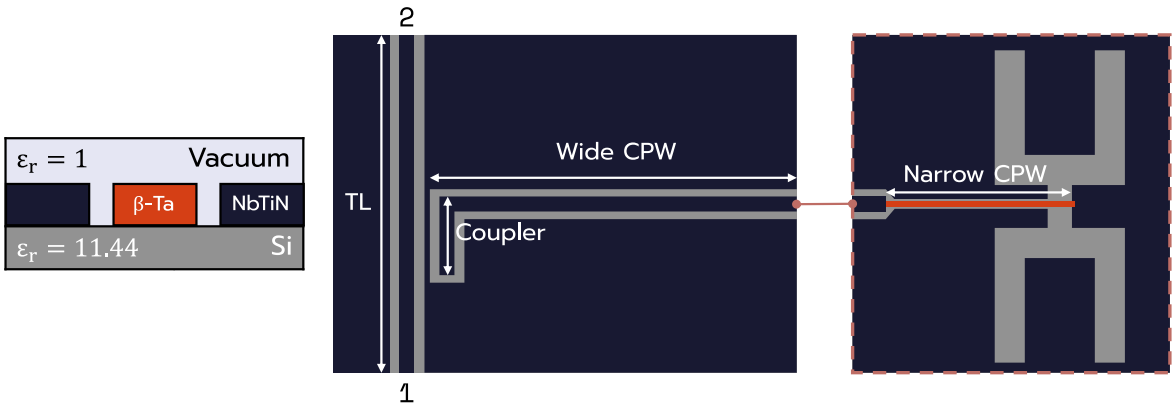

Figure 3.4 – Schematic representation of the single KID structure in Sonnet. A simulation is done looking at ports 1 and 2, on either side of the readout line (TL). We can vary the length of the coupler to obtain different coupling quality factors. We can also change the length of the wide CPW. A Sonnet component is added to the open end of the wide CPW. This component contains the result of a single simulation of the narrow CPW with the antenna at the load. The corresponding stratification is shown on the left. The sheet impedances for NbTiN and β-Ta are determined using Mattis-Bardeen theory.

[1] Network analysis using transmission matrices is elaborated on in Appendix D.3. See Appendix A for the associated Python model.

4

Lens-antenna coupled KIDs

Using a lens antenna to couple radiation to a β-Ta film inside of a hybrid KID, would enable us to detect $50 - 90$GHz radiation. To be able to perform experiments to evaluate this, we design lens-antenna coupled KIDs to detect in the center of this frequency range, at 70GHz. We use the methods described in chapter 3 to achieve this.

For the radiation to efficiently couple from the antenna to the narrow CPW containing the β-Ta film, it is crucial that we reach a sufficient impedance match between them (as discussed in section 3.2). The large normal state resistivity of β-Ta ultimately leads to a large characteristic impedance for the narrow CPW. Consequently, there will be a significant impedance mismatch if the antenna is simply designed to have an impedance of $Z_{\text{ant}} = 50\Omega$. For this reason, we reverse the order in which we design the different elements. Only after we have optimized the dimensions of the narrow CPW in section 4.1, we will start to design the lens antenna and evaluate its performance in section 4.2.
This chapter concludes by modeling the designed KIDs and the influence of the antenna impedance on them in section 4.3.

4.1. Quarter-wave resonator design

In section 2.2, it was covered how CPWs can be used as transmission lines to design a hybrid KID. In this section, we use that concept to optimize the cross-sectional dimensions of both the narrow and wide CPWs.

For the dielectric substrate, we will use a monolithic Si wafer ($\epsilon_r = 11.44$) of thickness $t_{\text{wafer}} = 350\mu$m. The properties of NbTiN and β-Ta are obtained from previous experiments. These properties are summarized in table 4.1.

Table 4.1 – Material properties used in this thesis, obtained from previous experiments.

	T_c [K]	ρ_N [μΩ·cm]	d [nm]
NbTiN	15	217	200
β-Ta	0.6	210	40
β-Ta	0.6	49	100

4.1.1. Narrow CPW

A commonly used way to improve the coupling between two elements is by inserting a transmission line of length $\lambda/4$ and designing that element to have a characteristic impedance equal to the geometric mean $Z_t = \sqrt{Z_0 Z_L}$ [52]. This transmission line, placed between the antenna feed and the narrow CPW, would then function as an impedance transformer. However, the large resistivity of β-Ta also leads to large attenuation, resulting in most of the radiation being attenuated within the length of the quarter-wave impedance transformer, making it ineffective for our application. Additionally, this would result in the β-Ta film having a large active volume.

For the narrow CPW design, we thus have to consider two constraints. On the one hand, we have to reduce its characteristic impedance, allowing us to find a matching antenna impedance for optimal power coupling. On the other hand, we want to minimize its active volume to maximize the responsivity of the KIDs.

To be able to further quantify the constraints affecting volume, we define the volume necessary to achieve a certain level of attenuation. We deem -10dB to be the minimum required attenuation, and use the attenuation per unit length (equation 2.19) to find the corresponding length l_{narrow}. This yields the respective β-Ta volume,

$$V = d_{\beta\text{-Ta}} \cdot S \cdot l_{\text{narrow}}. \tag{4.1}$$

There is a lower limit to the dimensions of the CPW due to limitations in fabrication using UV lithography, where we can not make the central line width S and gap width W smaller than approximately $2 - 3$µm.

We will now perform sweeps in the three defining dimensions of the narrow CPW, S, W, and $d_{\beta\text{-Ta}}$, and look at their effect on Z_0 and V. Based on the constraints, this will thus allow us to find an optimized design. Because ρ_N depends on thickness d, we use the two data points from table 4.1 and interpolate for other thicknesses.

We start by looking at the central line width S and gap width W in figure 4.1.

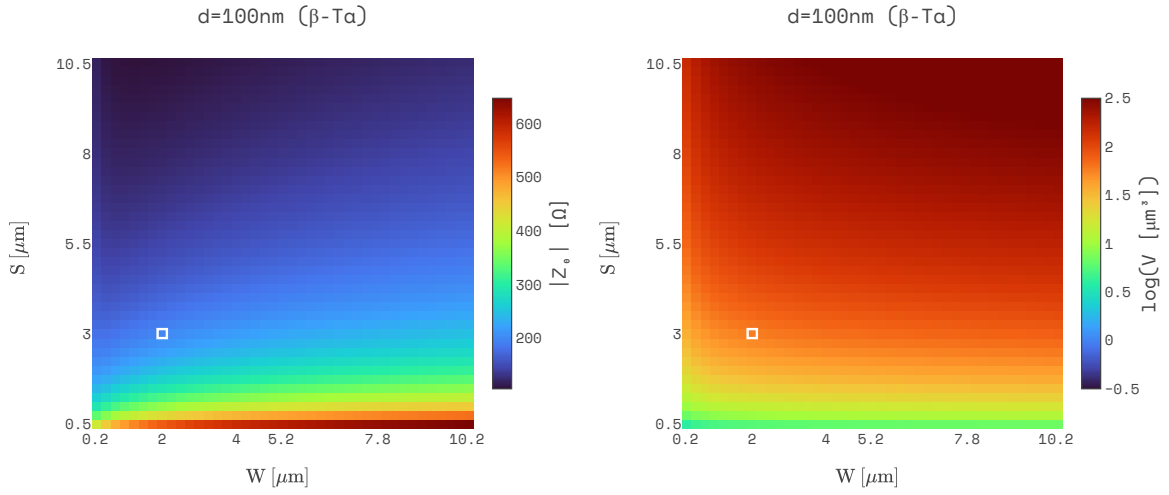

(a) **(b)**

Figure 4.1 – Analysis of tuning the gap width W and central line width S for a β-Ta/NbTiN hybrid CPW, evaluated at $f = 70$GHz and $T = 0.06$K. We use the normal state resistivity for $d_{\beta-\text{Ta}} = 100$nm (see table 4.1). **(a)** The magnitude of the characteristic impedance Z_0, and **(b)** the required volume V to attain -10dB attenuation, are given for varying W and S. The white markers are used to indicate a 2-3-2 CPW.

We notice that changes in W do not seem to have as much effect on both Z_0 and V as changes in S. For smaller W, it allows for reduction in impedance and volume, so we can simply take the minimized $W = 2\mu$m, which is now only constrained by fabrication limitations.
Before choosing a value for S, we also need to look at the effect of changing $d_{\beta\text{-Ta}}$, which is visible in figure 4.2. The magnitude of the characteristic impedance mostly scales with S and $d_{\beta\text{-Ta}}$: the larger these two dimensions, the smaller the impedance will be. This directly contradicts the goal of minimizing the volume, and we will have to find a compromise. We settle on a 2-3-2 design, using $d_{\beta\text{-Ta}} = 100$nm, limited by the fabrication limit for S. A schematic cross-section of this design for the narrow CPW is shown in figure 4.3a.
Figure 4.4 shows the corresponding frequency dependencies of the characteristic impedance and attenuation. For $f = 70$GHz, we find $Z_0 = (179 - 87.3j)\ \Omega$. Given these dimensions, we find $l_{\text{narrow}} \approx 189.2$µm to correspond to -10dB attenuation. The active volume of β-Ta now minimizes to $V \approx 56.8\mu\text{m}^3$.

4.1.2. Wide CPW

For the wide CPW we use a 8-20-8 CPW, of which we find that it closely matches the characteristic impedance of the coaxial cables used for readout ($Z_0 \approx 50\Omega$, see figure 4.4). See figure 4.3b for a schematic of the cross section of the wide CPW. We use the same dimensions for the readout line, to which all MKIDs will be capacitively coupled.

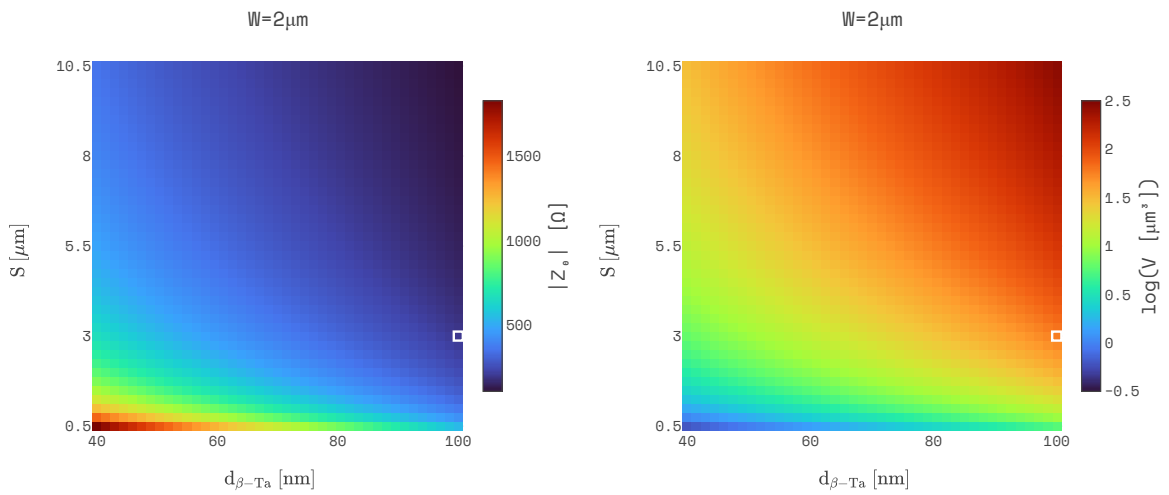

(a) (b)

Figure 4.2 – Analysis of tuning film thickness $d_{\beta-\mathrm{Ta}}$ and central line width S for a β-Ta/NbTiN hybrid CPW, evaluated at $f = 70$GHz and $T = 0.06$K. For the gap width, we use $W = 2$μm. **(a)** The magnitude of the characteristic impedance Z_0, and **(b)** the required volume V to attain -10dB attenuation, are given for varying $d_{\beta-\mathrm{Ta}}$ and S. To approximate the dependence on $d_{\beta-\mathrm{Ta}}$, we use a first-order interpolation between $\rho_N = 210\mu\Omega$·cm for $d_{\beta-\mathrm{Ta}} = 40$nm and $\rho_N = 49\mu\Omega$·cm for $d_{\beta-\mathrm{Ta}} = 100$nm. The white markers are used to indicate a 2-3-2 CPW with $d_{\beta-\mathrm{Ta}} = 100$nm.

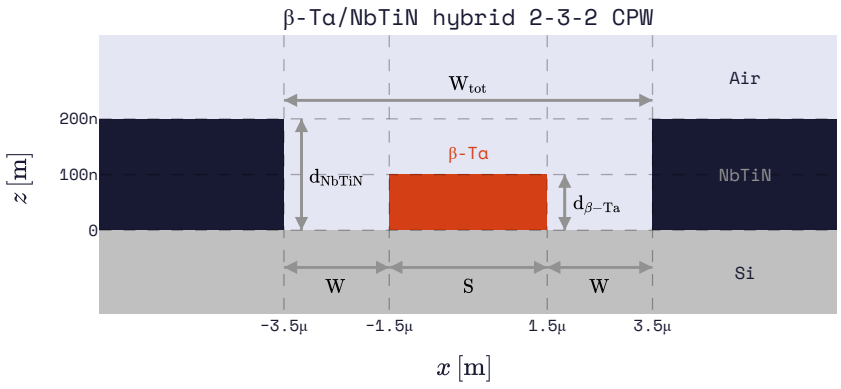

(a)

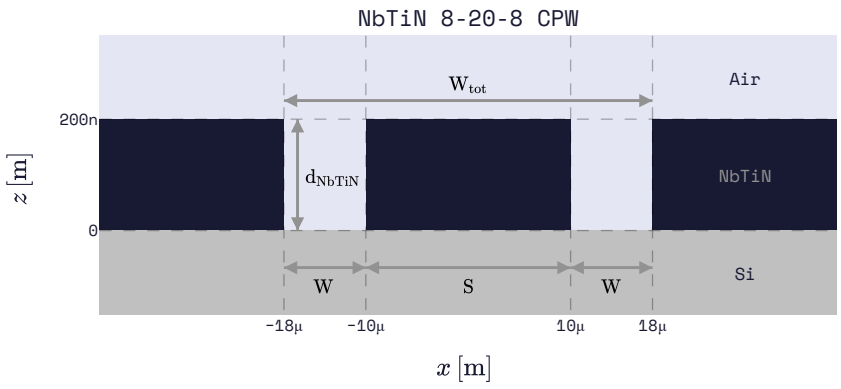

(b)

Figure 4.3 – Schematic cross-sections of the **(a)** hybrid 2-3-2 (narrow) and **(b)** 8-20-8 (wide) coplanar waveguides.

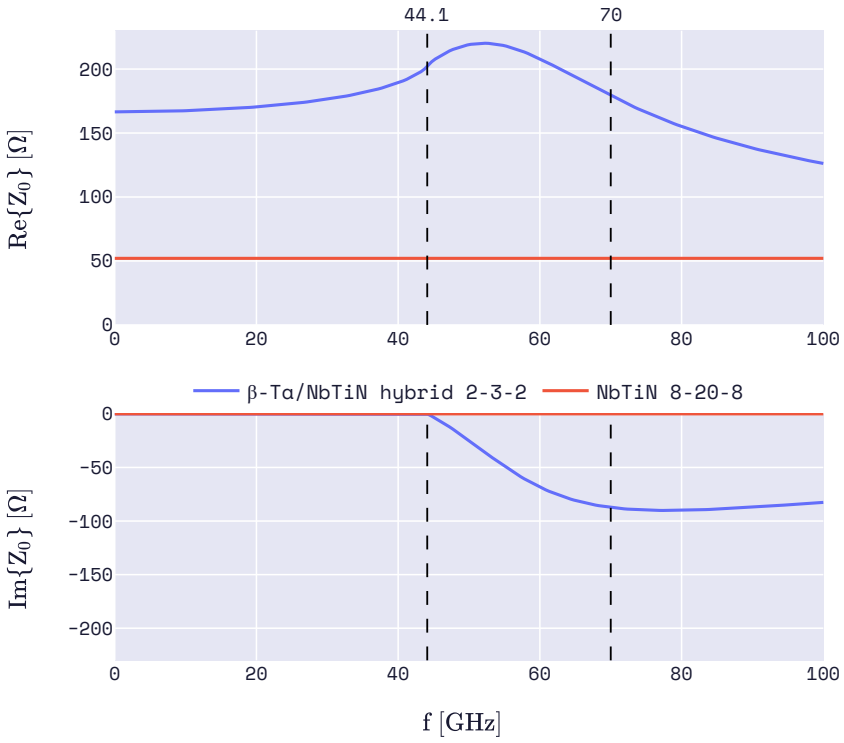

(a)

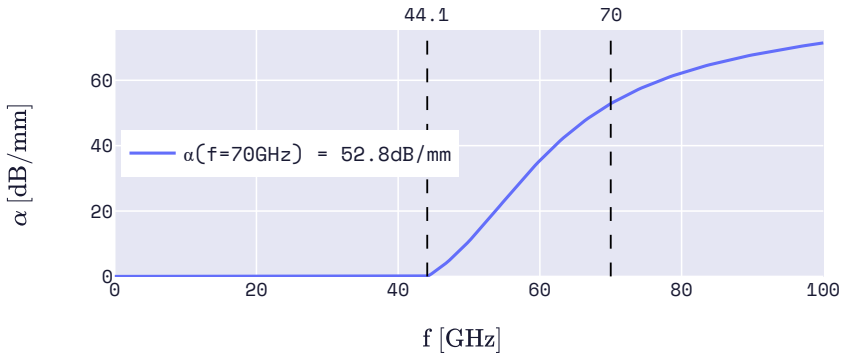

(b)

Figure 4.4 – **(a)** Real and imaginary parts of the characteristic impedance Z_0 for the narrow (blue) and wide (red) CPW designs. **(b)** Real part of the propagation constant within the narrow CPW. Converting to attenuation, we observe that we only need a length of $l_{\text{narrow}} \approx 189.2\mu\text{m}$ to attain attenuation $= -10\text{dB}$ at $f = 70\text{GHz}$ within the narrow CPW. Figure 4.3 shows the dimensions of each, and table 4.1 can be used for corresponding material properties used.

4.2. Lens antenna design

With the cross-sectional dimensions of the CPWs in the resonator found in the previous section, we can design the rest of the lens-antenna coupled KID. This section starts by looking at the cryogenic setup that will be used for experimental evaluation of our design, as it will impose constraints on the dimensions of the lens. Next, we will design the twin-slot antenna, considering the band-pass filter in the setup and the CPW designs. We conclude by evaluating the performance of the lens antenna by simulating its beam pattern.

4.2.1. Cryogenic setup

An experiment with KIDs is typically performed at an operating temperature of $T = T_c/10$, with T_c being the critical temperature of the active superconductor. Furthermore, we require the KIDs to be in an environment that is as light tight as possible, such that the detectors are protected from stray light. These conditions can be met by containing the KIDs in a light-tight box, and mounting them in an adiabatic demagnetization refrigerator (ADR).

The setup meant for experiments at 70GHz and its relevant dimensions is shown in figure 4.5. Radiation emitted by a blackbody source, which emits a blackbody spectrum, is filtered to be only within a defined bandwidth around 70GHz before reaching the chip in the sample holder.

The box containing the blackbody can be moved vertically, relative to the light-tight box. This allows the distance to the detector to be minimized, therefore maximizing the achievable opening angle of the blackbody to the sample (see θ_0 in figure 4.5). As we use a lens antenna to couple incoming radiation to the β-Ta film, the top of the lens is used as the reference for this opening angle. The space between sample holder and band-pass filter limits the height from the bottom of the substrate (the position of the antenna) to the top of the lens to approximately 10mm. This limits us in the choice of a lens.

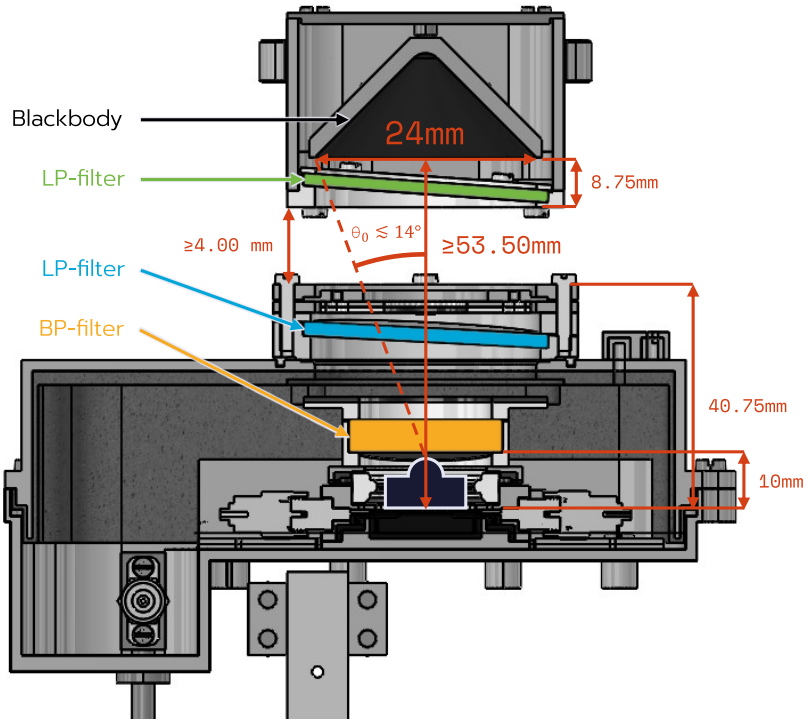

Figure 4.5 – CAD schematic with dimensions of the ADR setup for measurements at 70GHz (adapted from [77]). Radiation coupling between the blackbody and the lens antenna of the chip pass two low-pass filters, $f = 210$GHz (green) and $f = 190$GHz (blue), and a band-pass filter centered at $f = 70$GHz (yellow). Each of the three filters is placed at slight angles to mitigate any standing waves caused by reflections of the filters. The chip is mounted in a sample holder inside of a light-tight box. The maximum for the opening angle θ_0 is determined for a lens height of approximately 6.61mm.

4.2.2. Lens geometry

We see the geometry of the $D = 8.995$mm extended hemispherical lens we choose for our design in figure 4.6. While this diameter is quite small compared to the size of our antenna, we can not increase it much more

before we reach the maximum available height between the sample holder and the band-pass filter in our setup (see figure 4.5). The lens, fabricated for a previous project [77], requires an additional $850\mu m$ extension to the antenna to synthesize an elliptical lens shape. Given our wafer thickness $t_{wafer} = 350\mu m$ and the use of another (spacer) wafer with thickness $t_{spacer} = 350\mu m$, we can still approximate this extension.
Given the height of the lens, we obtain a maximum opening angle within the setup of $\theta_0 \leq 14.35°$.

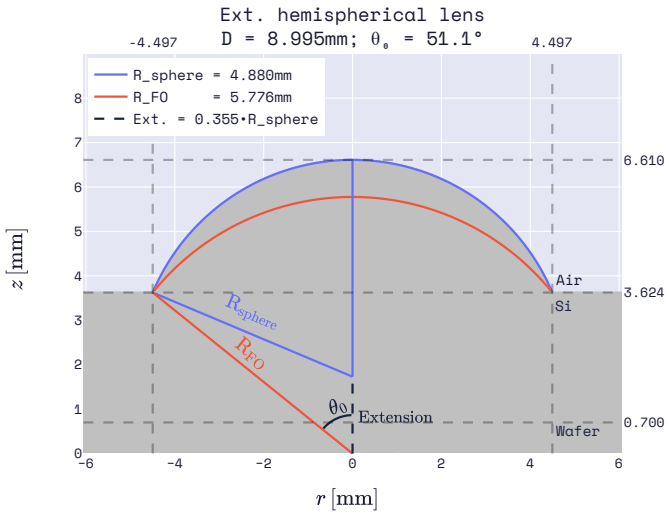

Figure 4.6 – Available extended hemispherical lens which will be mounted on the back side of the substrate, and aligned to the antenna. The antenna is therefore centered in the origin of this figure. We use two wafers of equal thickness $t_{wafer} = 350\mu m$ to obtain $t_{wafer} = 700\mu m$.

4.2.3. Twin-slot antenna optimization

The transmission profile of the band-pass filter in the setup is shown in figure 4.7.
The bandwidth of the band-pass filter, which is defined by the frequencies for which its transmission is larger than $-3dB$, should ideally be smaller than the bandwidth of the antenna we design.

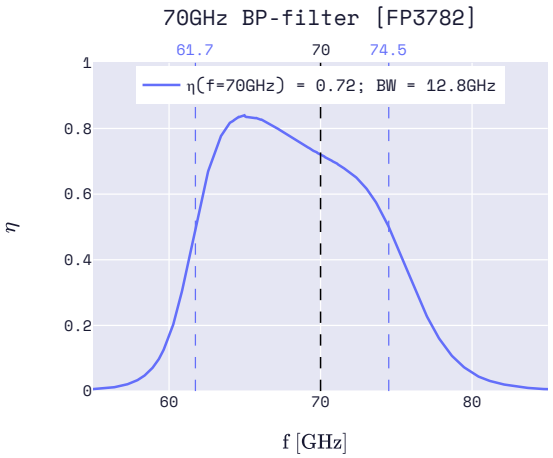

Figure 4.7 – Power transmission of the band-pass filter used for a frequency range centered at 70GHz. We define the bandwidth (BW) of the band-pass filter as the range in which the transmission is larger than 50%, or $-3dB$.

For sufficient coupling between the narrow CPW and the antenna, we deem a power reflection of less than $-10dB$ to be sufficient. We therefore define the bandwidth of the antenna as the frequency range in which the power reflection is less than $-10dB$. This way, the band-pass filter will limit the bandwidth of the total system used for radiation coupling from the blackbody source to the narrow CPW. This condition translates to the desire for a sufficient impedance match across the entire bandwidth of the band-pass filter. We choose dimensions for which the antenna impedance does not change too much around 70GHz, as the impedance of the CPW also does not change too much around $f = 70GHz$ (see figure 4.4).

The narrow CPW will have to fit inside of the gap in the structure of the twin-slot antenna for it to be able to connect to its feed, and thus $d_{ant} > W_{\text{tot}}^{\text{narrow}} = 7\mu\text{m}$. Given that the length of the narrow CPW is shorter than the available width inside of the antenna for an attenuation of -10dB ($l_{\text{narrow}} \approx 189.2\mu\text{m} < W_{ant}/2$), we will have to further constrain d_{ant}. Now, the total width of the wide CPW will have to fit inside of the gap in the antenna slot, and thus $d_{ant} > W_{\text{tot}}^{\text{wide}} = 36\mu\text{m}$. Most of the current in a CPW flows at the edges of the central line and ground planes [78]. So, for the antenna and CPW to not interfere significantly, we therefore consider a minimum size of twice the total width of the wide CPW, and thus $d_{ant} > 72\mu\text{m}$.

We now perform parameter sweeps in c_3, c_4, and c_5. Within the band-pass filter's bandwidth, we observe that

- increasing $W_1 = c_3 L_{ant}$ increases $\text{Re}\{Z_{ant}\}$ and decreases $\text{Im}\{Z_{ant}\}$,
- decreasing $W_2 = c_4 L_{ant}$ decreases $\text{Im}\{Z_{ant}\}$, and
- decreasing $d_{ant} = c_5 L_{ant}$ is most effective for our case, as it increases $\text{Re}\{Z_{ant}\}$ significantly.

We find that we can realistically only achieve a perfect impedance match by making d_{ant} really narrow. Therefore, we choose to use the minimum we set for d_{ant}. We choose a large W_1 and a small W_2 to complete the dimensions of our twin-slot antenna. For the dimensions of the twin-slot antenna design, see figure 4.8. The antenna impedance as a function of frequency is shown in figure 4.9a.

Implication of used reflection coefficient definition

The antenna design presented is optimized for minimal voltage reflection (equation 3.4). We obtain a -10dB bandwidth encompassing the bandwidth of the band-pass filter (see figure 4.9b). However, we realize that for efficient power coupling, minimal power reflection should have been considered (equation 3.5), and thus a conjugate match. The design's reflection at 70GHz increases from -12.5dB to -5.86dB if we account for the correct definition of power reflection, see figure 4.9b. For an experiment, this decrease in coupling would not be detrimental. Furthermore, we realize that the method presented would not change under this different condition for an impedance match.

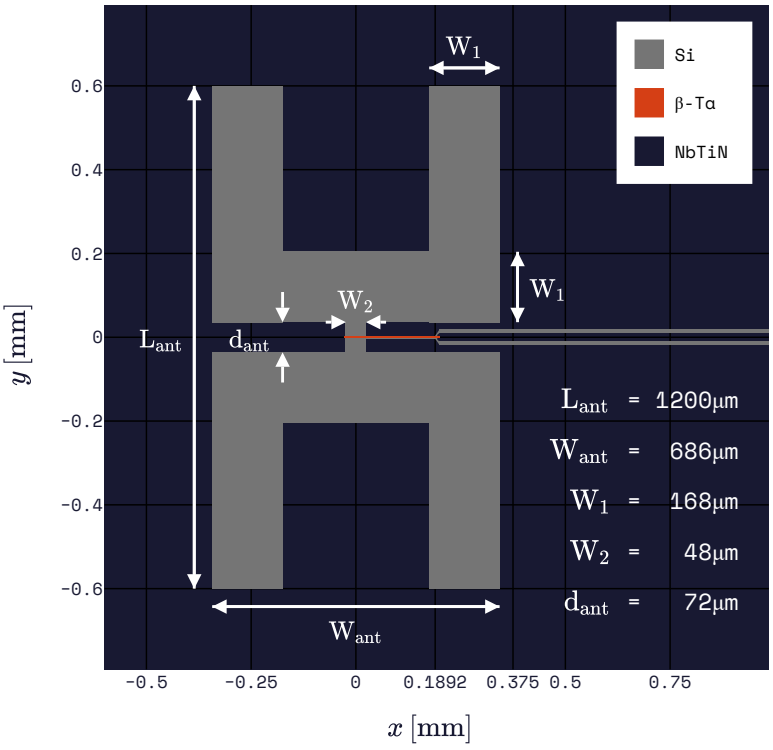

Figure 4.8 – Schematic representation of the twin-slot antenna design for 70GHz with its five determining dimensions listed. For reference, the hybrid KID structure has been drawn as well, with the β-Ta (orange) in the narrow CPW stretching from the NbTiN ground (dark blue) on the left of the origin to the wide CPW at $x \approx 189.2\mu\text{m}$, which corresponds to an attenuation of approximately -10dB. The areas without superconducting film will have the Si substrate directly exposed (gray).

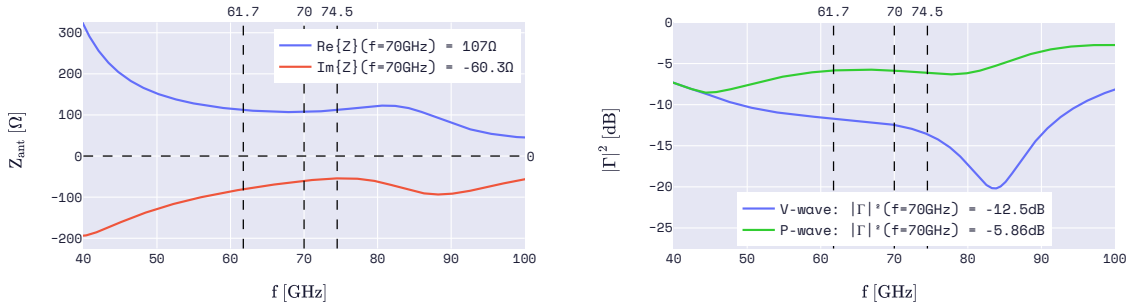

(a) (b)

Figure 4.9 – Impedance match between the optimized twin-slot antenna and the narrow CPW design. **(a)** The antenna input impedance Z_{ant}, determined at its port. **(b)** The power reflection, for both voltage and power wave definitions, between the coupled antenna impedance from (a) and the narrow CPW characteristic impedance from figure 4.4. If voltage wave reflection is considered, we obtain a -10dB bandwidth ranging $50 - 90$GHz. Vertical black dashed lines are used to show the bandwidth of the band-pass filter in the cryogenic setup (see figure 4.7).

4.2.4. Beam pattern analysis

Given the obtained design for the lens-antenna, we proceed to analyze its performance through its beam pattern.

Far field of the lens antenna

We show the obtained normalized far-field beam pattern at different azimuthal angles φ in figure 4.10.

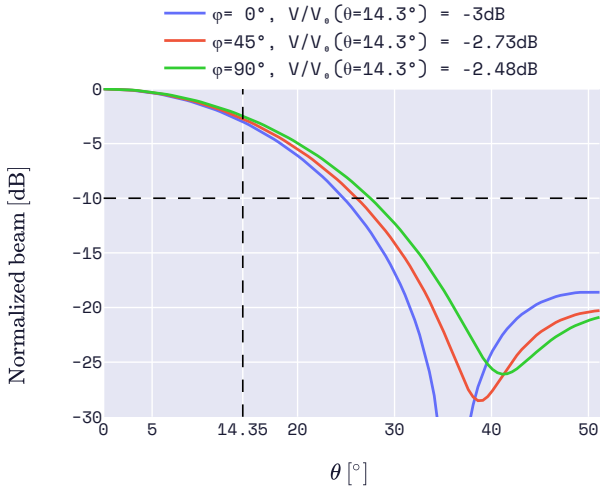

Figure 4.10 – (Normalized) beam pattern for the lens-antenna consisting of the lens in figure 4.6 coupled to the antenna in figure 4.8. Three different azimuthal angles φ are shown (i.e., $\varphi = 0$ along the x-axis in figure 4.8). A vertical dashed line is used to indicate the opening angle within the setup given the source at minimum distance from the top of the lens (see figure 4.5).

Using the PO tool, we find $\eta_{tap} = 0.958$, $\eta_{ap} = 0.517$, and $\eta_{so} = 0.540$. While we thus find that the directivity of the lens antenna is quite optimal, we expect the lens to not be able to couple incident power to the antenna efficiently, which leads to a large spillover.
In the far field, the -10dB angle to define the main beam of the twin-slot antenna within the Si substrate is found to be $\theta \approx 50°$, therefore matching the angle θ_0 of the lens (see figure 4.6) and illuminating its entire surface. This is reflected in the taper efficiency we find.

The main beam of the lens antenna reaches -10dB for $\theta_0 \approx 25°$, which is larger than the maximum obtainable opening angle in the setup of $\theta_0 \approx 14.5°$ (see figure 4.5). This means that the main beam of the lens antenna will also illuminate the side walls in the cryogenic setup. We attribute this limited bending to the broadside of the antenna to the size of our lens, which is small with respect to the wavelength at $f = 70$GHz. In fact, the diameter of the lens aperture is just a little bit larger than twice the wavelength in vacuum ($2\lambda \approx 8.57$mm).

There are some implications of the PO technique that we have to keep in mind. Firstly, the PO tool uses the approximation that the incident field on the lens is locally a plane wave and the lens locally flat, such that they can use Snell's law to determine the transmission angles for the refraction at the surface of the lens [74]. While this holds in the limit for small curvature, errors start to appear once the curvature of the lens is too large. Secondly, we are now assuming that the source can be considered to be in the far field such that the source propagates as plane waves, which might not always be an accurate assumption. When the distance to the source is large enough, the incident electromagnetic field across the lens may be considered to be in the far field. For this, we turn to the Rayleigh range used when considering a Gaussian beam coupled to the lens. We find the Rayleigh range then through the Gaussian beam's waist size w_0,

$$z_R = \frac{\pi w_0^2}{\lambda}, \tag{4.2}$$

where λ is the wavelength of the radiation. In the case of a synthesized elliptical lens, the lens aperture limits the size of the beam, so $w_0 = D$ [70]. We find $z_R \approx 59.3$mm, which is larger than the minimal achievable distance between the source and our lens ($z \geq 53.5$mm, see figure 4.5), such that the black body source is at $z < z_R$ and thus in the near field. The results from the PO tool will thus only be accurate for larger distances.

Near field of the antenna

Designing at $f = 70$GHz meant that our twin-slot antenna design is exceptionally large. We are therefore also interested in the near field of the antenna within the substrate. Figure 4.11 shows the electric field evaluated at the backside of the $t_{\text{wafer}} = 350\mu$m wafer.

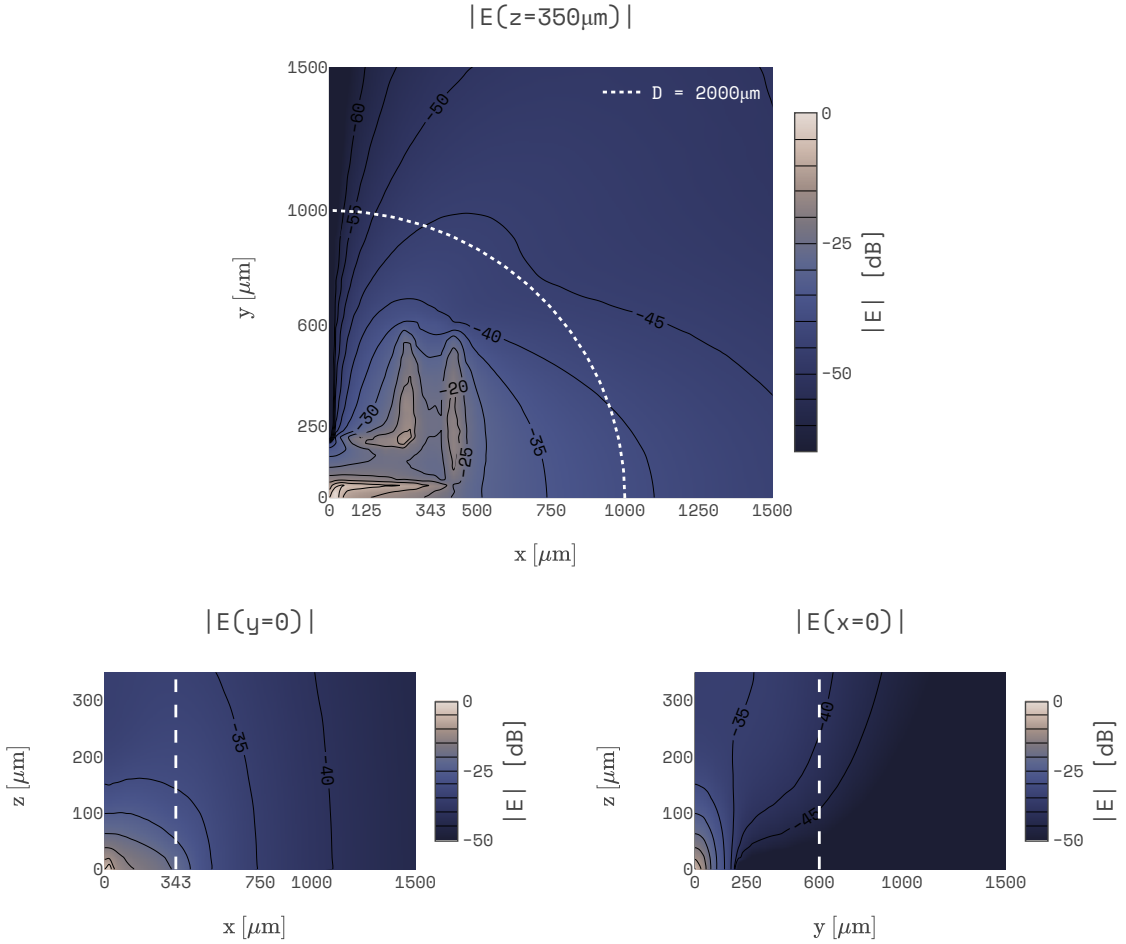

Figure 4.11 – Cross-sections of the magnitude of the normalized electric field as transmitted by the antenna (centered in origin), shown in three planes: **(top)** the x-y plane at $z = 350\mu$m, equivalent to the back side of the antenna's Si substrate, **(bottom left)** the x-z plane, and **(bottom right)** the y-z plane. Each figure only shows the first quadrant of the plane and can be extrapolated for $z > 0$ using the symmetries of the antenna. The bottom figures have vertical dashed lines to indicate $W_{ant}/2$ and $L_{ant}/2$ in the x-z plane and y-z plane, respectively. The top figure has an indicator for a circle of diameter $D = 2$mm.

4.3. Effects of antenna impedance at readout

Given the twin-slot antenna design, we want to analyze the full antenna-coupled KIDs. We do so using the two methods described in section 3.3.
We simulate the antenna-coupled KIDs in Sonnet for five different wide CPW lengths l_{wide} at $T = 0.1\text{K}$. We do the same simulations for five different lengths without the antenna structure, so with a shorted load. From these simulations, we determine the resonance frequency using curve-fitting to equation 2.28 and compare those results to what we expect from network analysis. To incorporate the impedance of the antenna when applying the resonance condition for the latter method, we use the impedance at its port (similar to the CST antenna simulation of figure 3.1). The results are shown in figure 4.12. Between the cases where the antenna is and is not added as a load, we observe that the reactance of the antenna at these readout frequencies causes the required KID length to scale down. A black dashed curve is also added to the figure to show the difference between shorted KIDs using Perfect Electric Conductors (PEC) and using NbTiN and β-Ta. In the case of using PECs, the resonator structure has no kinetic inductance. The wavelength inside of it is therefore larger, requiring longer KID lengths for the same resonance frequency.

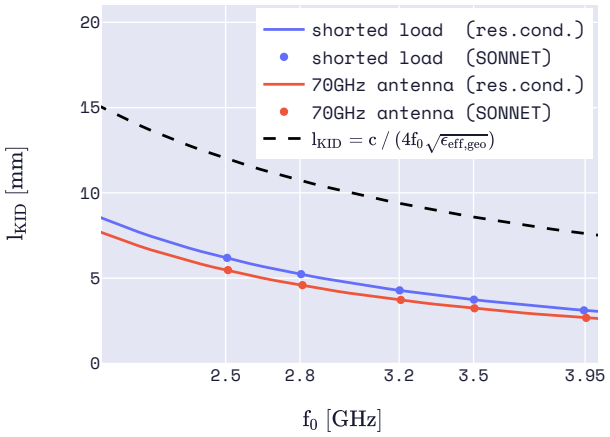

Figure 4.12 – Total KID length l_{KID} as determined through the resonance condition for different design resonance frequencies f_0 evaluated for KIDs with either a shorted load (blue) or termination in the antenna design (red). Simulations for five different total KID lengths were performed using Sonnet and the results of their fitted resonance frequencies were plotted. A dashed curve was added to represent the equivalent shorted resonator without kinetic inductance. Standard deviations in fitted resonance frequencies are smaller than markers used.

We notice that there is a significant difference in the internal quality factor between the cases with and without the antenna. With the antenna, we find $Q_i \sim 2 \cdot 10^3 - 4 \cdot 10^3$. Without the antenna, these values are at least a factor 10 larger. Somehow, the antenna is causing significant losses in the KID at readout frequencies. We want to investigate whether this is due to the way we simulate the antenna structure.

Within CST, we increase the box size and look at what that would do to the antenna impedance at readout frequencies. We observe that the box size has a significant effect on the real part of the impedance, while the imaginary part is unchanged. This is in line with what we expected. For larger box sizes, the real part of the impedance decreases, visible in figure 4.13a. However, we also see that there is apparently a limit in this decrease. While increasing the box size, this limit appears first for larger frequencies. We extend the range of box sizes and visualize the impedance as a heatmap in figure 4.13b.
For box sizes larger than approximately a quarter wavelength in vacuum, indicated by the white dotted line in the figure, we clearly observe this limit: further increase in box size has no longer effect on the impedance. We conclude that we require the simulation box size to be larger than quarter wavelength to make sure unwanted modes in the antenna are eliminated.

We use the obtained antenna impedance as the load impedance in the network analysis method from section 3.3. Using the defining features of the forward transmission S_{21} (equation 2.28), we can subsequently analyze the resonance frequency and internal quality factor of the resonator.
We plot Q_i as a function of the length of the narrow CPW, which is equivalent to the length of the β-Ta strip $l_{\beta-\text{Ta}}$. We consider different design resonance frequencies and evaluate at $T = 0.1\text{K}$. The results of the different cases are shown in figure 4.14.

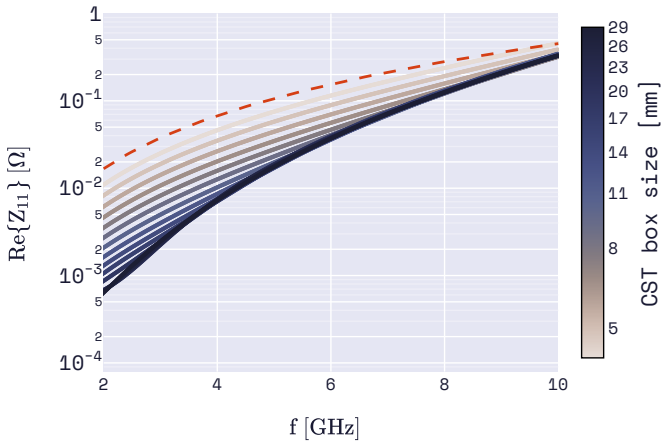

(a)

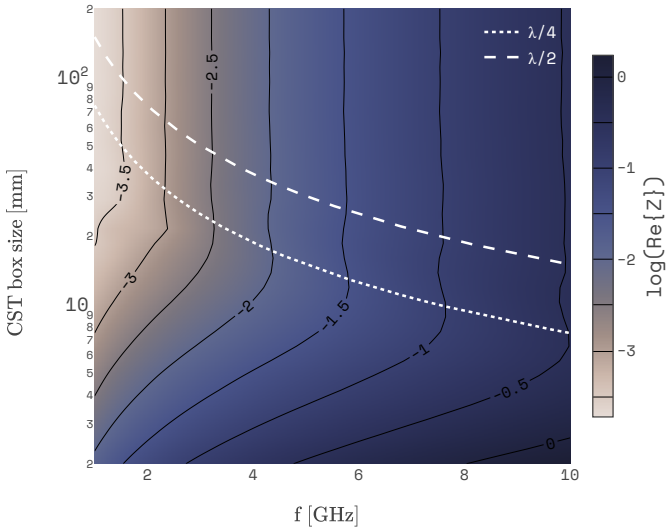

(b)

Figure 4.13 – **(a)** The real part of the antenna impedance for the 70GHz antenna design at readout frequencies. Different box dimensions in the setup in CST were used to determine the antenna impedance. The box size represents the side of the cubic box in which the antenna is centered (see figure 3.1). An orange dashed line is added to show the respective antenna impedance found in a Sonnet simulation with a square area of 2×2mm. **(b)** A larger range in box sizes shown as a heatmap with the box size on the y-axis. A white dotted line is added showing the quarter wavelength $\lambda/4 = c/4f$ and a dashed line showing half-wave length $\lambda/2 = c/2f$ at these readout frequencies.

For each case, smaller resonance frequencies result in larger internal quality factors. This is in line with what we expect: the radiative losses in the antenna is seen to decrease for smaller frequencies (see 4.13b), and we know from chapter 2 that dissipation due to the quasiparticle system decreases for smaller frequencies as well (see figure 2.5).
If we use the result for a sufficiently large box size in CST, we find internal quality factors that are the same order of magnitude as the ones originally observed when analyzing the KID simulations in Sonnet without the use of an antenna.
Nevertheless, it is clearly visible that the antenna impedance still dominates the dissipation due to the quasiparticle system, as an increase in length of the β-Ta line also increases the internal quality factor. If we isolate the Q_i due to the quasiparticle system, equal to only using the imaginary part of the antenna impedance at the load, we yield figure 4.14b. We now see the effect we would initially expect: for larger $l_{\beta-\mathrm{Ta}}$, we have more resistance within the resonator and thus more dissipation, translating to smaller internal quality factors.

As the dissipation due to the quasiparticle system depends on the quasiparticle density, and thus also on the temperature, we can show how the internal quality factor is dominated by the losses through the antenna for low temperatures. Q_i for our antenna-coupled hybrid KID with and without the antenna is shown in figure

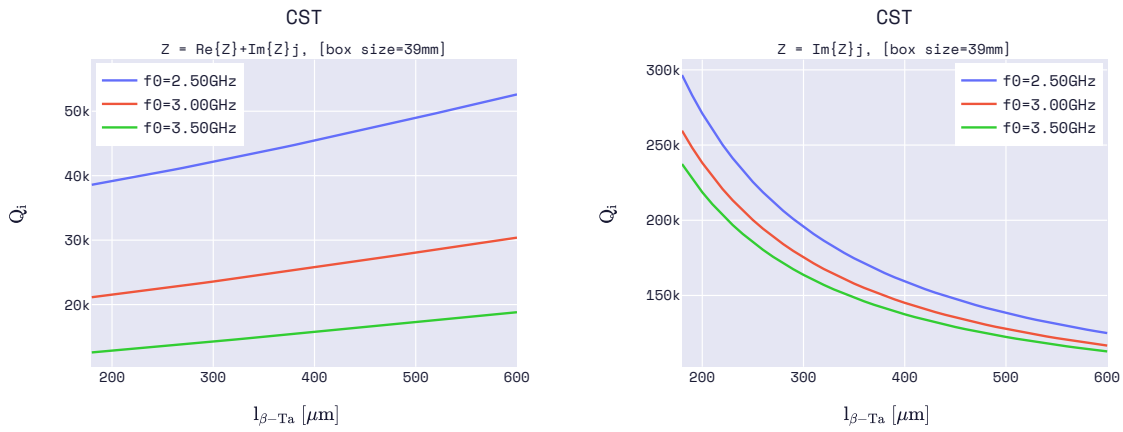

(a) (b)

Figure 4.14 – Internal quality factor Q_i of the antenna-coupled hybrid KIDs as a function of the length of the β-Ta central line of the narrow CPW, plotted for different resonance frequencies f_0 at $T = T_c^{\beta-\mathrm{Ta}}/6 = 0.1\mathrm{K}$. Q_i was obtained using the network analysis method. For figure **(a)**, the antenna impedance was found in CST using a box size of 39mm, which is larger than the quarter wavelength of the frequencies considered. Figure **(b)** uses only the imaginary part of the antenna impedance from (a). The range in lengths $l_{\beta-\mathrm{Ta}}$ linearly translates to approximately -10dB to -30dB in attenuation of $f = 70$GHz radiation inside of the narrow CPW.

4.15a. We see that at around $T \gtrsim 0.15\mathrm{K}$, the Q_i is dominated by the dissipation in β-Ta. Note that the curves do not perfectly converge to the same values for higher T, as the total KID length to reach the same f_0 is different.

Next to the antenna impedance affecting the Q_i, it also affects the kinetic inductance fraction α_k. For the determination of α_k, we can look at the shift in f_0 when replacing the active superconductor β-Ta by a PEC ($R_s = 0$ and $L_{k,s} = 0$). Namely, $f_0 \propto \sqrt{1-\alpha_k}$ and $\alpha_k = 0$ when using a PEC. Now, we may consider $f_0 = f_0^{\mathrm{PEC}}\sqrt{1-\alpha_k}$. This yields,

$$\alpha_k = 1 - (f_0/f_0^{\mathrm{PEC}})^2. \tag{4.3}$$

We evaluate the kinetic inductance fraction at different resonance frequencies using the model for our hybrid KIDs, shown in figure 4.15b. Conclusively, the antenna impedance is seen to dominate the radiation loss predicted using Mattis-Bardeen theory, and it lowers the kinetic inductance fraction due to its added inductance.

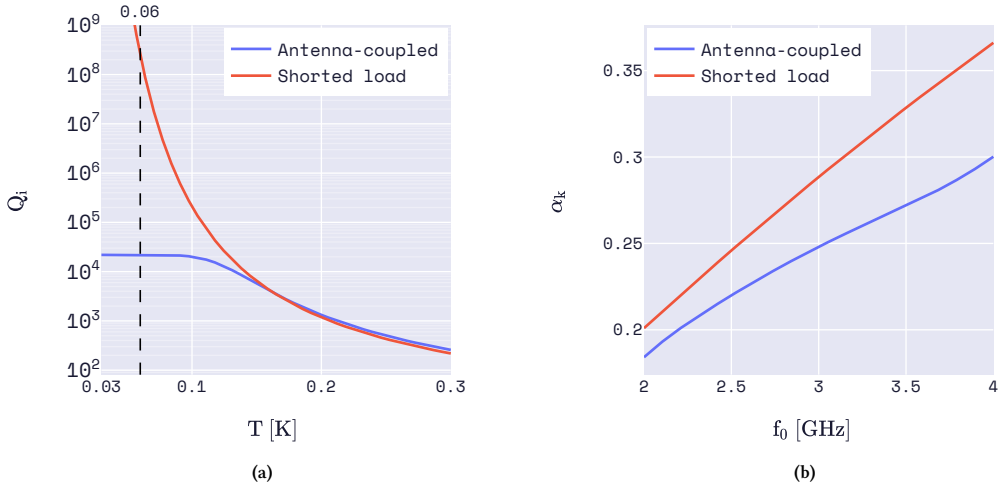

(a) (b)

Figure 4.15 – Effect of adding the 70GHz antenna design to the load of the hybrid KID. l_{narrow} is chosen such that attenuation of -10dB is achieved for 70GHz radiation, and l_{wide} is adjusted to attain the desired resonance frequency. For both figures, the cases with the antenna as the load and a shorted load are considered. **(a)** The internal quality factor Q_i as a function of temperature T of the KID with $f_0 = 3$GHz. A vertical guideline is added at $T = T_c^{\beta-\mathrm{Ta}}/10 = 0.06\mathrm{K}$. **(b)** The kinetic inductance fraction as a function of resonance frequency.

5

Chip design

In this chapter, we combine the obtained CPW dimensions with the lens antenna design from chapter 4 to create masks. These masks can be used for fabrication of chips. We start by looking at the chip designs and discuss their respective design parameters in section 5.1. In section 5.2, we go over the different steps used to generate their respective masks.

5.1. Design parameters

For fabrication, a mask containing nine unique chips was designed. In this section, we discuss their configuration and defining properties.

All of the 20×20mm chip designs are placed in a 3×3 grid in a full wafer design, see figure 5.1. The result of the mask generation of a single chip is shown in figure 5.2.

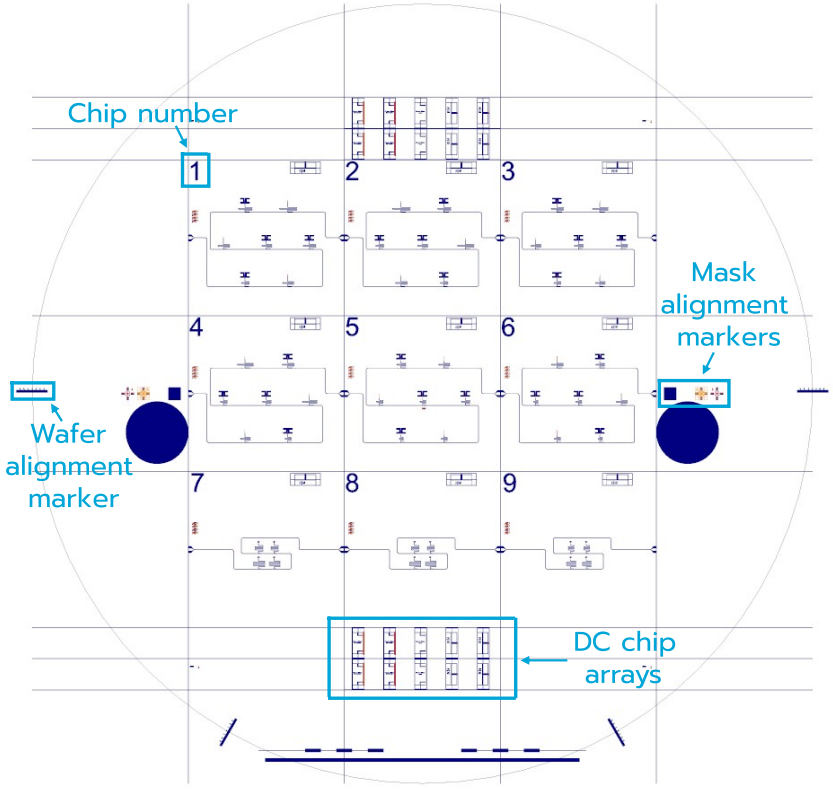

Figure 5.1 – The front side of the full wafer design, containing the nine (numbered) chips.

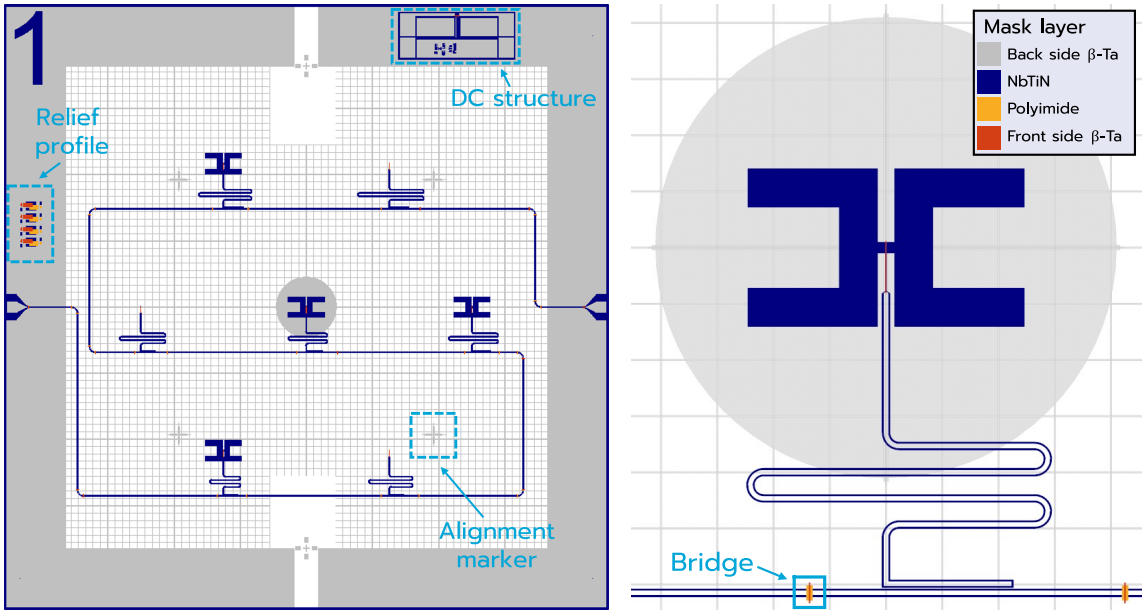

(a) (b)

Figure 5.2 – **(a)** Generated 20×20mm mask for chip design 1. The dark blue layer is a negative mask for NbTiN, yellow a positive mask for polyimide, and orange a positive mask for β-Ta on the front side. The gray layer is used to show the negative mask of β-Ta on the back side of the chip, where a mesh structure and alignment markers are. The center KID is the only detector to have a 2mm hole in the back side mesh. The surrounding KIDs alternate in having the antenna design at their shorted end. **(b)** A zoom-in of the center KID, which is designed for $f_0 = 3$GHz.

Six out of nine chips were designed for 70GHz (chips 1-6). These six chips are designed in pairs, with each pair having a different length of the narrow CPW used for all of their KIDs. These lengths relate to different levels of attenuation of 70 GHz radiation inside the CPW (see figure 5.3). As a result, each pair will have KIDs with a different volume of β-Ta. This would allow us to compare the effect and difference in performance of different volumes.

The remaining three chips were similarly designed for 350GHz[1] (chips 7-9), such that their performance can be benchmarked against previous experiments using Al instead of β-Ta. In this chapter, we continue to focus on the 70GHz designs.

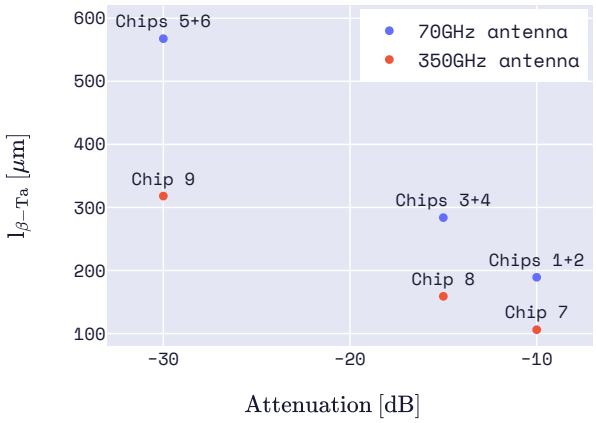

Figure 5.3 – Different lengths of the β-Ta strips, contained in the center line of the narrow CPW, based on the achievable level of attenuation of the radiation frequency its corresponding antenna-coupled KIDs were designed for. For the chips designed for 70 GHz (blue markers), three pairs of chips were designed for attenuation levels of -10dB, -15dB, and -30dB. The same levels of attenuation were used for the three chips designed for 350 GHz (red markers).

[1] Details on the design for the chips designed for 350GHz are given in Appendix E. For these chips, we design KIDs in the same $2.50 - 3.50$GHz frequency range and use $Q_c = 3 \cdot 10^4$.

Given the available area on a chip, for which the used monolithic Si substrates have dimensions 20×20mm, we can only fit seven KIDs on each chip. These KIDs are placed on a hexagonal grid with 5.5mm spacing between the center points of each antenna (or the equivalent coordinate when the KID has a shorted load). That way, we allow for enough space between the antennas and mitigate the interference of their fields.

The seven KIDs are designed to be within a frequency range of $2.50 - 3.50$GHz. For every chip, the center KID is designed at $f_0 = 3$GHz with 0.4GHz spacing to its frequency-neighboring KIDs, such that it is properly isolated from the other KIDs in frequency space. This results in seven different design resonance frequencies $[2.50, 2.55, 2.60, 3.00, 3.40, 3.45, 3.50]$GHz. Only the center KID is aligned with the lens, and will be properly illuminated by the source within the cryogenic setup; the other KIDs will not have a lens, and will therefore be considered dark.

While both chips in a pair will have exactly the same center KID design, the other six KIDs will either have an antenna as the load of the resonator, or have a shorted load instead. The two chips within a pair differentiate in the sense that the KIDs with (or without) an antenna are 'mirrored' in frequency space. This alternating pattern allows us to directly compare the effect of the antenna at each of the design resonance frequencies. Additionally, in case one of the two in a pair of chips shows any defects during fabrication, we will still be able to obtain results over the same frequency range for a certain level of attenuation. This alternating pattern in having an antenna at the load and its induced alternating pattern in KID lengths is shown for chips 1 and 2 in figure 5.4. Corresponding expected differences in Q_i and α_k are shown in figure 5.5. As was discussed in section 4.3, we expect the radiative losses in the antenna at readout frequencies to dominate the Q_i. Figure 5.5a shows that this is more apparent for the 70GHz than for the 350GHz, which we account to the difference in size of the dimensions of the antenna structure. Note that the larger attenuation at $f = 350$GHz leads to shorter l_{narrow} for the design with the 350GHz antenna (see figure 5.3). This leads to the larger Q_i observed at high temperatures ($T \gtrsim 0.15$K), which is limited by dissipation due to the quasiparticle system, and a smaller kinetic inductance fraction (see figure 5.5, corresponding to chip 7).

For all KIDs, we use a design coupling quality factor $Q_c = 10^4$. Q_c is deliberately chosen smaller than the $Q_i(f_0)$ from figure 5.5a, to make sure that it will slightly dominate, yet not significantly reduce the loaded quality factor.

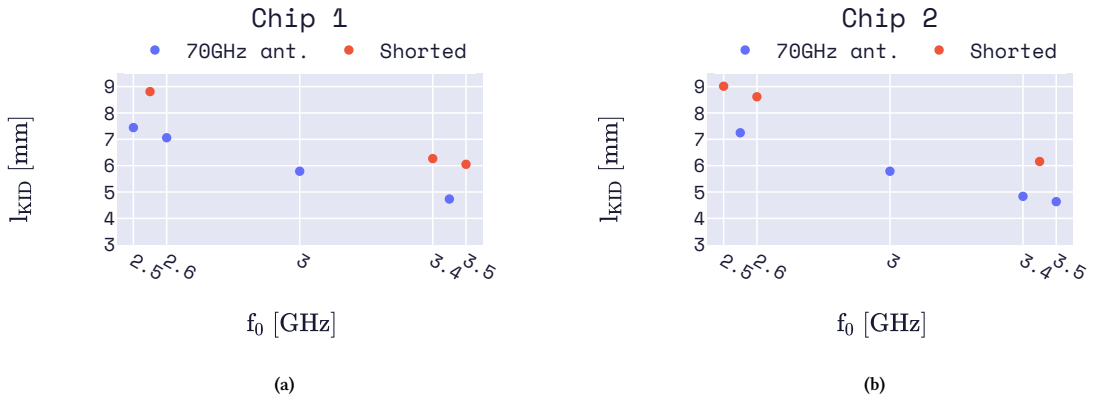

Figure 5.4 – Total KID length $l_{\text{KID}} = l_{\text{wide}} + l_{\text{narrow}}$ as a function of the design center frequencies for each of the KIDs on **(a)** chip 1 and **(b)** chip 2. The blue markers depict the KIDs that are coupled to an antenna at the shorted end of the resonator. The red markers depict the KIDs that are terminated in a shorted load (without antenna). Chips 1 and 2 have the exact same design for the center KID, which is designed at $f_0 = 3$GHz, but the arrangement of the other KIDs is exactly inverted in terms of whether they have an antenna or not.

5.2. Mask design generation

The mask design generation itself is based on an existing mask generation code for an array of lens-antenna coupled KIDs [79]. Using the design input parameters, the mask code builds each chip in CIF format [80]. Each material used is assigned a separate layer to correspond to a different mask layer used in fabrication.

Resonance frequency tuning

For the determination of the required length for the wide NbTiN CPW, we can use the resonance condition from equation 2.23 for the simplified representation of the quarter-wave resonator shown in figure 5.6.

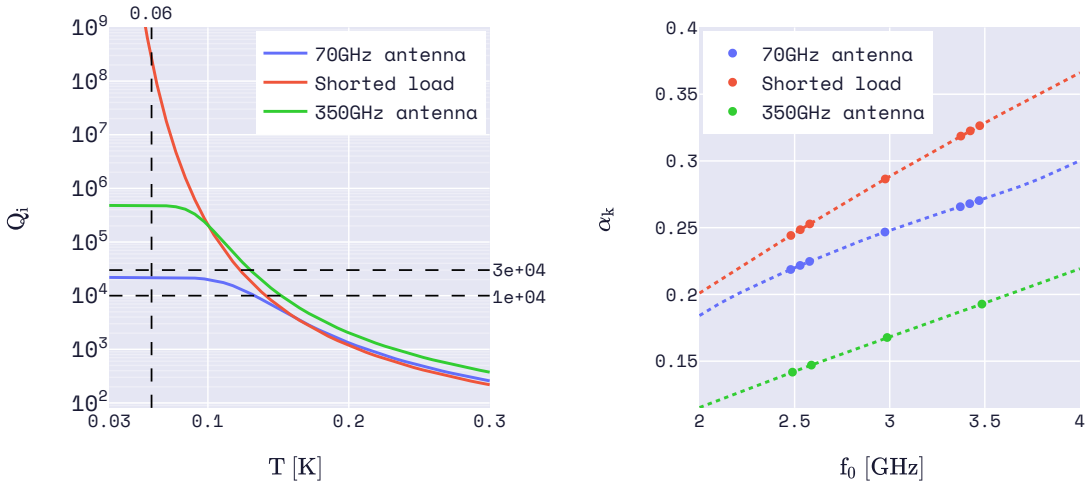

(a) (b)

Figure 5.5 – Effect of adding the two different antenna designs to the load of the hybrid KID. l_{narrow} is chosen such that attenuation of -10dB is achieved for the radiation frequency their respective antenna is designed for, and l_{wide} is tuned to obtain the desired resonance frequency. For both figures, the cases with the 70GHz antenna as the load (blue) and a shorted load (red) are considered (corresponding to both chip 1 and 2). **(a)** The internal quality factor Q_i as a function of temperature T of the KID when designed for $f_0 = 3$GHz. Vertical guidelines are added at $T = T_c^{\beta-\text{Ta}}/10 = 0.06$K. Horizontal guidelines are added to show $Q_c = 10^4$ for the 70GHz design and $Q_c = 3 \cdot 10^4$ for the 350GHz design. **(b)** The kinetic inductance fraction as a function of the different design resonance frequencies. The continuous dependence is visualized by dashed lines.

The resonance condition results in $\text{Im}\{Z_{in}^{\text{wide}}\} = -\text{Im}\{Z_{in}^{\text{narrow}}\}$. As the load impedance will be fixed for the two cases on each chip (either the antenna impedance or a shorted load), $\text{Im}\{Z_{in}^{\text{narrow}}\}$ can be found using the input impedance for a terminated transmission line. For the superconducting lines, we can consider the loss terms R_l and G_l to be relatively small at readout frequencies, such that we can approximate them as lossless lines with $Z_0 = \sqrt{L_l/C_l} = \sqrt{L/C}$ and $\gamma = j\omega\sqrt{L_l C_l} = j\omega\sqrt{LC}/l$. This reduces equation 2.21,

$$Z_{in} = \frac{Z_L + j\sqrt{\frac{L}{C}}\tan(\omega\sqrt{LC})}{1 + jZ_L\sqrt{\frac{C}{L}}\tan(\omega\sqrt{LC})}. \tag{5.1}$$

We can use this equation for input impedance to find the length of the wide CPW l_{wide} to achieve a design resonance frequency f_0,

$$l_{\text{wide}} = \frac{v_{\text{phase, NbTiN}}}{2\pi f_0}\cot^{-1}\left(\frac{\text{Im}\{Z_{in}^{\text{narrow}}\}}{Z_0^{\text{NbTiN}}}\right). \tag{5.2}$$

Note that using this equation, we expect to see a slight shift in f_0, as we simplify and choose not to use a compensation for shift due to the coupler capacitance[2]. We can observe this expected shift in figure 5.5b, which is insignificant compared to the effect of possible changes in material properties due to fabrication conditions.

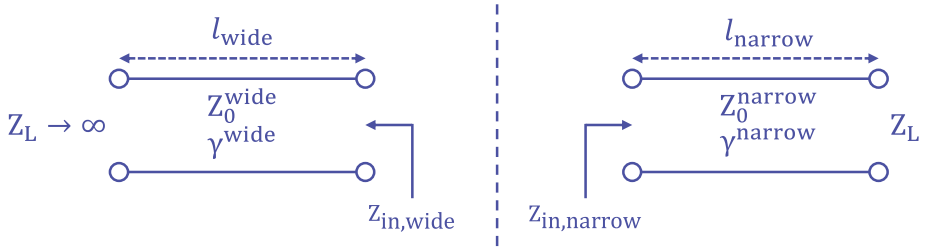

Figure 5.6 – Schematic circuit representation of a quarter-wave hybrid KID. The load impedance of the wide CPW is approximated to be that of an open load. The narrow CPW is terminated in a load impedance Z_L, which is either the antenna impedance or a shorted load.

[2]This change in the resonance condition caused by the coupler capacitance is elaborated on in Appendix A.2.

Coupler length determination

For each detector to reach the designed coupling quality factor Q_c, we have to consider a certain length of the coupler l_{coupler} to reach the required capacitance C_c (see equation 2.27). Both the readout and wide CPWs are chosen to be NbTiN 8-20-8 CPWs, so we can conveniently reuse data from previous simulations [79]. This data was retrieved by performing Sonnet simulations for different l_{coupler} evaluated at different f_0, to find the respective Q_c. By 2D spline interpolation of the simulation data, we yield l_{coupler} for each of the designs. This is visualized in figure 5.7.

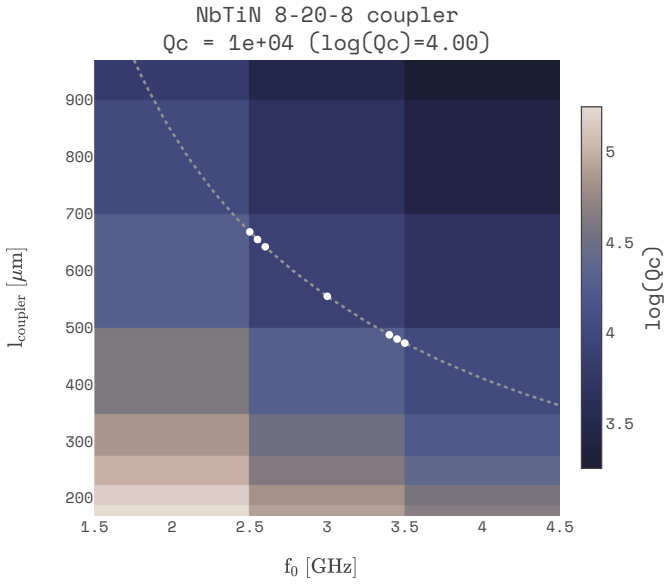

Figure 5.7 – l_{coupler} as a function of f_0 given $Q_c = 10^4$ for a NbTiN 8-20-8 coupler, shown as a gray dotted line. For design resonance frequencies, the corresponding lengths on this curve are highlighted using white markers. The 2D spline interpolation uses data points in the $f_0 - l_{\text{coupler}}$ plane (indicated as the center of the tiles in the figure). Each data point corresponds to a different value for $\log(Q_c)$, indicated using the heatmap.

Aperture in back side mesh

On the back side of the chip, we create a mesh structure. This mesh acts as an absorber for high energy phonons resulting from cosmic ray interactions [19], and it also absorbs any radiation that is not coupled to the antenna, but can scatter into the chip and couple to other KIDs [41].

We reuse a mesh design which was originally optimized for 150GHz [77]. This design would still absorb around 60% and transmit around 25% of radiation within the bandwidth of our band-pass filter, while it is almost transparent for readout frequencies. Its dimensions are defined as $w = 237\mu\text{m}$ and $g = 7\mu\text{m}$, using the definition for dimensions shown in figure 5.8. Normally, the mesh should be made from a superconductor with a T_c lower than that of the active superconductor, in our case β-Ta, to down-convert incident photons to phonon energies lower than the pair-breaking energy [40]. The back side mesh will be made of a 36nm β-Ta layer, likely making this down-conversion less effective.

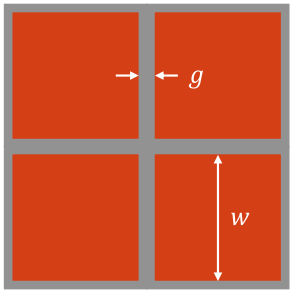

Figure 5.8 – Four neighbouring unit cells of the back side mesh. Orange shows where Ta squares of width w are located on the back side of a Si substrate. The squares have a spacing g between them.

Because the mesh acts as a shield on the back side of the chip, we will have to leave a circular aperture in the mesh for radiation to still couple from the lens to the antenna of the center KID. Usually, this is simply done by making the aperture slightly larger than the intersection of the plane at the back side of the substrate (at $z = t_{\text{wafer}}$) and the cone made by the angle θ_0 of the lens diameter to its focus point. This results in $D_{\text{aperture}} = 2t_{\text{wafer}} \tan\theta_0 \approx 868\mu\text{m}$.
Since we stated that our lens is relatively small for the size of the antenna, the beam pattern of the antenna will be affected by the mesh structure if we use this aperture diameter, and the aperture will have to be larger to mitigate this. A better way to determine the diameter is thus to look at the magnitude of the electric field of the antenna at the back side of the substrate, for which we turn to the electric field in the near field (see figure 4.11). The diameter of the aperture is then found by choosing the minimal diameter for which the magnitude of the electric field is considered negligible. Looking at figure 4.11, we choose a safe $D_{\text{aperture}} = 2\text{mm}$ to be at magnitudes that are close to 20dB lower than the magnitude within the projection of the antenna in the x-z plane.

6 Conclusion

In this thesis, we investigate the design of Microwave Kinetic Inductance Detectors for the $50-90$GHz range. These superconducting pair-breaking detectors are applicable to the next generation of Cosmic Microwave Background missions, where this frequency range is important for measurement of spectral distortions and B-mode polarization patterns in the CMB. The conventionally used Aluminum ($T_c = 1.2 - 1.4$K) would not be able to reach frequencies below 90GHz. However, breaking of Cooper-pairs within β-phase Tantalum (β-Ta, $T_c = 0.6 - 1.0$K) is possible for radiation as low as $f = 45$GHz. This thesis therefore investigates the use of the low-T_c superconductor β-Ta as the active superconductor in hybrid MKIDs designed for $50 - 90$GHz.

Certain challenges in using β-Ta were identified.
Firstly, β-Ta is characterized as a disordered superconductor, and therefore reduces detector responsivity due to the effect of quasiparticle trapping. To mitigate this effect, we require the volume of β-Ta to be decoupled from incoming radiation frequency. We solve this by designing lens-antenna coupled KIDs. The lens antenna features an extended hemispherical lens that is coupled to a twin-slot antenna optimized for optical coupling at these radiation frequencies.
Additionally, we require efficient power coupling at 70GHz from the antenna to the volume of β-Ta. Considering the large normal state resistivity of β-Ta, the characteristic impedance of the narrow CPW in the resonator shows both a large real and imaginary part at 70GHz.
We have identified two connected constraints on β-Ta. We present a method to tune the dimensions of the narrow CPW, and find a compromise which optimizes for minimization of characteristic impedance and volume, simultaneously. The twin-slot antenna design is subsequently also optimized for a sufficient coupling, yielding a bandwidth stretching $50 - 90$GHz.
For this prototype, we considered voltage wave reflection for the impedance match. We realize that for power coupling, however, one would have to consider impedance matching for power waves. The corresponding required conjugate impedance match does not change the methodology proposed.
We identify that the addition of the antenna structure limits the achievable internal quality factor and reduces the kinetic inductance fraction of the antenna-coupled KIDs.

Conclusively, we have presented a methodology allowing for MKID technology to be used for future CMB missions in the $50 - 90$GHz range using β-Ta, while optimizing for radiative coupling and sensitivity of the detectors.

Future work

We identified multiple aspects which have to be further investigated or can be further improved using different engineering approaches in future work.

The prototype designs presented in chapter 5 are currently being fabricated. In the near future, their detector sensitivity and optical coupling efficiency can be experimentally evaluated.
We identified that the large antenna design poses limitations to the internal quality factor. Other loss sources, such as the increased microwave loss due to quasiparticle trapping in β-Ta, potentially dominate the internal quality factor instead. It should be examined whether the radiative losses can be seen in our prototype.

Experiments to show photon-noise-limited sensitivity are also of interest for the presented prototype designs for 350GHz, for which we can benchmark the sensitivity limits and achieved optical efficiency.

We require further decoupling of the volume of β-Ta and the design of the antenna, as their dimension optimizations are currently still entangled through the conjugate impedance match. Only then can we reduce the volume of β-Ta even further, and have more engineering freedom in optimizing the lens antenna for high optical coupling efficiency. It should be investigated whether the choice of a twin-slot antenna is still best for this decoupling, or whether a different option like a leaky-wave antenna would offer more engineering freedom.
We could solve this matching issue by considering the use of different microwave impedance matching structures. Examples would entail matching using lumped elements, or tuning using stubs. These and other options should be investigated.

BCS and MB-theory were used to approximate the complex conductivity of β-Ta. However, these theories do not incorporate the effect of disorder in the density of states of disordered superconductors like β-Ta. This could mean that the characteristic impedance of the narrow CPW at pair-breaking frequencies deviates from the approximations used in the design. Therefore, a better description of the density of states of disordered superconductors is required to obtain the complex conductivity of β-Ta accurately.
Depending on the lithography and etching techniques applied in fabrication, there could be deviations from the dimensions we use in the design for the CPW structures. For example, overetching could create different thicknesses. Changes in thickness result in different values for sheet resistances, critically affecting the impedance matching between the narrow CPW and the antenna. Tolerances to changes in the sheet impedances should thus be examined.

We determined that we are in the near field of the lens antenna for the minimal distance between the blackbody source and the lens in the presented design. A simulation of the lens antenna using CST would obtain a more accurate near-field representation of the beam pattern. Given that we had to minimize the gap d_{ant}, this would also allow us to investigate the effect of the CPW line on the beam pattern and better define the constraint on d_{ant}.

References

[1] A. A. Penzias and R. Wilson. "A Measurement of Excess Antenna Temperature at 4080 Mc/s". In: *Astrophysical Journal* 142 (1965), pp. 419–421. ISSN: 0004-637X, 1538-4357. DOI: 10.1086/148307.

[2] D. J. Fixsen. "The Temperature of the Cosmic Microwave Background". en. In: *The Astrophysical Journal* 707.2 (2009). arXiv:0911.1955 [astro-ph], pp. 916–920. ISSN: 0004-637X, 1538-4357. DOI: 10.1088/0004-637X/707/2/916. URL: http://arxiv.org/abs/0911.1955.

[3] Planck Collaboration. "*Planck* 2018 results: I. Overview and the cosmological legacy of *Planck*". In: *Astronomy & Astrophysics* 641 (2020), A1. ISSN: 0004-6361, 1432-0746. DOI: 10.1051/0004-6361/201833880. URL: https://www.aanda.org/10.1051/0004-6361/201833880.

[4] J. Silk and J. Chluba. "Next Steps for Cosmology". en. In: *Science* 344.6184 (2014), pp. 586–588. ISSN: 0036-8075, 1095-9203. DOI: 10.1126/science.1252724. URL: https://www.science.org/doi/10.1126/science.1252724.

[5] J. Chluba et al. "New Horizons in Cosmology with Spectral Distortions of the Cosmic Microwave Background". en. In: *Experimental Astronomy* 51.3 (2021). arXiv:1909.01593 [astro-ph], pp. 1515–1554. ISSN: 0922-6435, 1572-9508. DOI: 10.1007/s10686-021-09729-5. URL: http://arxiv.org/abs/1909.01593.

[6] Y. B. Zeldovich and R. A. Sunyaev. "The interaction of matter and radiation in a hot-model universe". en. In: *Astrophysics and Space Science* 4.3 (1969), pp. 301–316. ISSN: 0004-640X, 1572-946X. DOI: 10.1007/BF00661821. URL: http://link.springer.com/10.1007/BF00661821.

[7] R. A. Sunyaev and Y. B. Zel'dovich. "Microwave Background Radiation as a Probe of the Contemporary Structure and History of the Universe". en. In: *Annual Review of Astronomy and Astrophysics* 18.1 (1980), pp. 537–560. ISSN: 0066-4146, 1545-4282. DOI: 10.1146/annurev.aa.18.090180.002541. URL: https://www.annualreviews.org/doi/10.1146/annurev.aa.18.090180.002541.

[8] J. P. Ostriker and E. T. Vishniac. "Generation of microwave background fluctuations from nonlinear perturbations at the ERA of galaxy formation". en. In: *The Astrophysical Journal* 306 (1986), p. L51. ISSN: 0004-637X, 1538-4357. DOI: 10.1086/184704. URL: http://adsabs.harvard.edu/doi/10.1086/184704.

[9] M. Birkinshaw. "The Sunyaev-Zel'dovich Effect". en. In: *Physics Reports* 310.2-3 (1999). arXiv:astro-ph/9808050, pp. 97–195. ISSN: 03701573. DOI: 10.1016/S0370-1573(98)00080-5. URL: http://arxiv.org/abs/astro-ph/9808050.

[10] S. A. Balashev et al. "Spectral distortions of the CMB dipole". en. In: *The Astrophysical Journal* 810.2 (2015). arXiv:1505.06028 [astro-ph], p. 131. ISSN: 1538-4357. DOI: 10.1088/0004-637X/810/2/131. URL: http://arxiv.org/abs/1505.06028.

[11] M. Kamionkowski and E. D. Kovetz. "The Quest for B Modes from Inflationary Gravitational Waves". en. In: *Annual Review of Astronomy and Astrophysics* 54.1 (2016). arXiv:1510.06042 [astro-ph], pp. 227–269. ISSN: 0066-4146, 1545-4282. DOI: 10.1146/annurev-astro-081915-023433. URL: http://arxiv.org/abs/1510.06042.

[12] A. Lewis and A. Challinor. "Weak Gravitational Lensing of the CMB". In: *Physics Reports* 429.1 (2006). arXiv:astro-ph/0601594, pp. 1–65. ISSN: 03701573. DOI: 10.1016/j.physrep.2006.03.002. URL: http://arxiv.org/abs/astro-ph/0601594.

[13] U. Seljak and M. Zaldarriaga. "Signature of Gravity Waves in Polarization of the Microwave Background". en. In: *Physical Review Letters* 78.11 (1997). arXiv:astro-ph/9609169, pp. 2054–2057. ISSN: 0031-9007, 1079-7114. DOI: 10.1103/PhysRevLett.78.2054. URL: http://arxiv.org/abs/astro-ph/9609169.

[14] Voyage 2050 Senior Committee. *Voyage 2050 - The ESA Science Programme for 2035-2050*. 2021. URL: https://www.cosmos.esa.int/web/voyage-2050.

[15] N. Krachmalnicoff et al. "Characterization of foreground emission at degree angular scale for CMB B-modes observations. Thermal Dust and Synchrotron signal from Planck and WMAP data". In: (2015). Version Number: 1. DOI: 10.48550/ARXIV.1511.00532. URL: https://arxiv.org/abs/1511.00532.

[16] K. Irwin and G. Hilton. "Transition-Edge Sensors". en. In: *Cryogenic Particle Detection*. Ed. by C. E. Ascheron et al. Vol. 99. Series Title: Topics in Applied Physics. Berlin, Heidelberg: Springer Berlin Heidelberg, 2005, pp. 63–150. ISBN: 978-3-540-20113-7, 978-3-540-31478-3. DOI: 10.1007/10933596_3. URL: http://link.springer.com/10.1007/10933596_3.

[17] P. A. R. Ade et al. "Improved Constraints on Primordial Gravitational Waves using *Planck* , WMAP, and BICEP/ *Keck* Observations through the 2018 Observing Season". en. In: *Physical Review Letters* 127.15 (2021), p. 151301. ISSN: 0031-9007, 1079-7114. DOI: 10.1103/PhysRevLett.127.151301. URL: https://link.aps.org/doi/10.1103/PhysRevLett.127.151301.

[18] J. Van Rantwijk et al. "Multiplexed Readout for 1000-Pixel Arrays of Microwave Kinetic Inductance Detectors". en. In: *IEEE Transactions on Microwave Theory and Techniques* 64.6 (2016), pp. 1876–1883. ISSN: 0018-9480, 1557-9670. DOI: 10.1109/TMTT.2016.2544303. URL: http://ieeexplore.ieee.org/document/7445881/.

[19] J. J. A. Baselmans et al. "A kilo-pixel imaging system for future space based far-infrared observatories using microwave kinetic inductance detectors". In: (2016). Version Number: 2. DOI: 10.48550/ARXIV.1609.01952. URL: https://arxiv.org/abs/1609.01952.

[20] J. J. A. Baselmans et al. "Ultra-sensitive THz microwave kinetic inductance detectors for future space telescopes". In: *Astronomy & Astrophysics* 665 (2022), A17. ISSN: 0004-6361, 1432-0746. DOI: 10.1051/0004-6361/202243840. URL: https://www.aanda.org/10.1051/0004-6361/202243840.

[21] B. A. Steinbach et al. "Thermal Kinetic Inductance Detectors for Ground-Based Millimeter-Wave Cosmology". en. In: *Journal of Low Temperature Physics* 193.3-4 (2018), pp. 88–95. ISSN: 0022-2291, 1573-7357. DOI: 10.1007/s10909-018-2016-y. URL: http://link.springer.com/10.1007/s10909-018-2016-y.

[22] A. Wandui et al. "Thermal kinetic inductance detectors for millimeter-wave detection". en. In: *Journal of Applied Physics* 128.4 (2020), p. 044508. ISSN: 0021-8979, 1089-7550. DOI: 10.1063/5.0002413. URL: https://pubs.aip.org/jap/article/128/4/044508/563372/Thermal-kinetic-inductance-detectors-for.

[23] A. Taniguchi et al. "DESHIMA 2.0: Development of an Integrated Superconducting Spectrometer for Science-Grade Astronomical Observations". en. In: *Journal of Low Temperature Physics* 209.3-4 (2022), pp. 278–286. ISSN: 0022-2291, 1573-7357. DOI: 10.1007/s10909-022-02888-5. URL: https://link.springer.com/10.1007/s10909-022-02888-5.

[24] K. Kohno et al. "Sub/millimeter-Wave Dual-Band Line Intensity Mapping Using the Terahertz Integral Field Units with Universal Nanotechnology (TIFUUN) for the Atacama Submillimeter Telescope Experiment (ASTE)". In: *Millimeter, Submillimeter, and Far-Infrared Detectors and Instrumentation for Astronomy XII*. Ed. by J. Zmuidzinas and J.-R. Gao. Yokohama, Japan: SPIE, 2024, p. 14. ISBN: 978-1-5106-8258-0. DOI: 10.1117/12.3021109. URL: https://www.spiedigitallibrary.org/conference-proceedings-of-spie/PC13102/3021109/Sub-millimeter-Wave-Dual-Band-Line-Intensity-Mapping-Using-the/10.1117/12.3021109.full.

[25] L. Ciesla et al. "PRIMA: PRIMAger, a far-infrared hyperspectral and polarimetric instrument". en. In: *Journal of Astronomical Telescopes, Instruments, and Systems* 11.03 (2025). arXiv:2509.01727 [astro-ph]. ISSN: 2329-4124. DOI: 10.1117/1.JATIS.11.3.031625. URL: http://arxiv.org/abs/2509.01727.

[26] M. Tsujii et al. "Commissioning the CMB polarization telescope GroundBIRD with the full set of detectors". en. In: *Millimeter, Submillimeter, and Far-Infrared Detectors and Instrumentation for Astronomy XII*. Ed. by J. Zmuidzinas and J.-R. Gao. Yokohama, Japan: SPIE, 2024, p. 7. DOI: 10.1117/12.3019544. URL: https://www.spiedigitallibrary.org/conference-proceedings-of-spie/13102/3019544/Commissioning-the-CMB-polarization-telescope-GroundBIRD-with-the-full-set/10.1117/12.3019544.full.

[27] N. Aghanim. *FOSSIL space mission proposal to ESA-M7 call*. 2022. URL: https://www.ias.u-psud.fr/sites/default/files/FOSSIL-web_0.pdf.

[28] J. Bardeen, L. N. Cooper, and J. R. Schrieffer. "Theory of Superconductivity". en. In: *Physical Review* 108.5 (1957), pp. 1175–1204. ISSN: 0031-899X. DOI: 10.1103/PhysRev.108.1175. URL: https://link.aps.org/doi/10.1103/PhysRev.108.1175.

[29] J. Baselmans. "Kinetic Inductance Detectors". en. In: *Journal of Low Temperature Physics* 167.3-4 (2012), pp. 292–304. ISSN: 0022-2291, 1573-7357. DOI: 10.1007/s10909-011-0448-8. URL: http://link.springer.com/10.1007/s10909-011-0448-8.

[30] P. De Visser. "Quasiparticle dynamics in aluminium superconducting microwave resonators". PhD thesis. Delft University of Technology, 2014. DOI: 10.4233/UUID:EAE4C9FC-F90D-4C12-A878-8428EE4ADB4C. URL: http://resolver.tudelft.nl/uuid:eae4c9fc-f90d-4c12-a878-8428ee4adb4c.

[31] N. Schwartz et al. "Temperature coefficient of resistance of beta-tantalum films and mixtures with b.c.c.-tantalum". en. In: *Thin Solid Films* 14.2 (1972), pp. 333–346. ISSN: 00406090. DOI: 10.1016/0040-6090(72)90433-6. URL: https://linkinghub.elsevier.com/retrieve/pii/0040609072904336.

[32] B. A. Mazin. *Superconducting Materials for Microwave Kinetic Inductance Detectors*. en. arXiv:2004.14576 [astro-ph]. 2020. DOI: 10.48550/arXiv.2004.14576. URL: http://arxiv.org/abs/2004.14576.

[33] D. W. Face and D. E. Prober. "Nucleation of body-centered-cubic tantalum films with a thin niobium underlayer". en. In: *Journal of Vacuum Science & Technology A: Vacuum, Surfaces, and Films* 5.6 (1987), pp. 3408–3411. ISSN: 0734-2101, 1520-8559. DOI: 10.1116/1.574203. URL: https://pubs.aip.org/jva/article/5/6/3408/246650/Nucleation-of-body-centered-cubic-tantalum-films.

[34] P. T. Mosely and C. J. Seabrook. "The crystal structure of β-tantalum". In: *Acta Crystallogr B Struct Sci* 29 (1973), pp. 1170–1171. DOI: 10.1107/S0567740873004140.

[35] J. J. Colin et al. "On the origin of the metastable beta-Ta phase stabilization in tantalum sputtered thin films". en. In: *Acta Materialia* 126 (2017), pp. 481–493. ISSN: 13596454. DOI: 10.1016/j.actamat.2016.12.030. URL: https://linkinghub.elsevier.com/retrieve/pii/S1359645416309661.

[36] A. Jiang et al. "Investigation of the structure of β-tantalum". en. In: *Thin Solid Films* 437 (2003), pp. 116–122. ISSN: 00406090. DOI: 10.1016/S0040-6090(03)00702-8.

[37] M. Tinkham. *Introduction to superconductivity*. eng. 2 ed. Dover books on physics. Mineola, NY: Dover Publ, 2015. ISBN: 978-0-486-43503-9.

[38] S. A. H. d. Rooij et al. *Recombination of localized quasiparticles in disordered superconductors*. en. arXiv:2410.18802 [cond-mat]. 2025. DOI: 10.48550/arXiv.2410.18802. URL: http://arxiv.org/abs/2410.18802.

[39] N. Zobrist et al. "Design and Performance of Hafnium Optical and Near-IR Kinetic Inductance Detectors". In: (2019). Version Number: 1. DOI: 10.48550/ARXIV.1911.06434. URL: https://arxiv.org/abs/1911.06434.

[40] K. Karatsu et al. "Mitigation of Cosmic Ray Effect on Microwave Kinetic Inductance Detector Arrays". en. In: *Applied Physics Letters* 114.3 (2019). arXiv:1901.02387 [astro-ph], p. 032601. ISSN: 0003-6951, 1077-3118. DOI: 10.1063/1.5052419. URL: http://arxiv.org/abs/1901.02387.

[41] S. J. C. Yates et al. *Surface wave control for large arrays of microwave kinetic inductance detectors*. en. arXiv:1707.02142 [astro-ph]. 2017. DOI: 10.48550/arXiv.1707.02142. URL: http://arxiv.org/abs/1707.02142.

[42] K. Kouwenhoven et al. "Resolving Power of Visible-To-Near-Infrared Hybrid beta-Ta / NbTiN Kinetic Inductance Detectors". en. In: *Physical Review Applied* 19.3 (2023), p. 034007. ISSN: 2331-7019. DOI: 10.1103/PhysRevApplied.19.034007. URL: https://link.aps.org/doi/10.1103/PhysRevApplied.19.034007.

[43] S. de Rooij. "Quasiparticle Dynamics in Disordered Superconductors". PhD thesis. Delft University of Technology, 2026. DOI: 10.4233/UUID:4E4A4BC3-C313-4EDB-BEE5-D5B4DD98026E. URL: https://resolver.tudelft.nl/uuid:4e4a4bc3-c313-4edb-bee5-d5b4dd98026e.

[44] R. W. Boyd. "Photon bunching and the photon-noise-limited performance of infrared detectors". en. In: *Infrared Physics* 22.3 (1982), pp. 157–162. ISSN: 00200891. DOI: 10.1016/0020-0891(82)90034-3. URL: https://linkinghub.elsevier.com/retrieve/pii/0020089182900343.

[45] L. N. Cooper. "Bound Electron Pairs in a Degenerate Fermi Gas". en. In: *Physical Review* 104.4 (1956), pp. 1189–1190. ISSN: 0031-899X. DOI: 10.1103/PhysRev.104.1189. URL: https://link.aps.org/doi/10.1103/PhysRev.104.1189.

[46] A. L. Fetter and J. D. Walecka. *Quantum theory of many-particle systems*. eng. International series in pure and applied physics. New York, NY: McGraw-Hill, 1971. ISBN: 978-0-07-020653-3.

[47] D. C. Mattis and J. Bardeen. “Theory of the Anomalous Skin Effect in Normal and Superconducting Metals”. en. In: *Physical Review* 111.2 (1958), pp. 412–417. ISSN: 0031-899X. DOI: 10.1103/PhysRev.111.412. URL: https://link.aps.org/doi/10.1103/PhysRev.111.412.

[48] J. Gao et al. “Equivalence of the Effects on the Complex Conductivity of Superconductor due to Temperature Change and External Pair Breaking”. en. In: *Journal of Low Temperature Physics* 151.1-2 (2008), pp. 557–563. ISSN: 0022-2291, 1573-7357. DOI: 10.1007/s10909-007-9688-z. URL: http://link.springer.com/10.1007/s10909-007-9688-z.

[49] R. L. Kautz. “Picosecond pulses on superconducting striplines”. en. In: *Journal of Applied Physics* 49.1 (1978), pp. 308–314. ISSN: 0021-8979, 1089-7550. DOI: 10.1063/1.324387. URL: https://pubs.aip.org/jap/article/49/1/308/9410/Picosecond-pulses-on-superconducting-striplines.

[50] K. Kouwenhoven. “Visible to Near-Infrared Kinetic Inductance Detectors”. en. PhD thesis. Delft University of Technology, 2024. DOI: 10.4233/UUID:9CC06B76-63B6-46F4-A5EB-0A965B562C2E. URL: http://resolver.tudelft.nl/uuid:9cc06b76-63b6-46f4-a5eb-0a965b562c2e.

[51] R. E. Collin. *Foundations for microwave engineering*. 2nd ed. IEEE Press series on electromagnetic wave theory. New York: IEEE Press, 2001. ISBN: 978-0-7803-6031-0.

[52] D. M. Pozar. *Microwave engineering*. eng. Fourth edition. Hoboken, NJ: John Wiley & Sons, Inc, 2012. ISBN: 978-0-470-63155-3.

[53] B. A. Mazin. “Microwave Kinetic Inductance Detectors”. en. PhD thesis. California Institute of Technology, 2004. DOI: 10.1142/9789811203787_0002. URL: https://www.worldscientific.com/doi/abs/10.1142/9789811203787_0002.

[54] R. Barends. *Photon-detecting superconducting resonators*. en. OCLC: 839642173. S.l.: s.n., 2009. ISBN: 978-90-8593-052-5.

[55] P. J. De Visser et al. “Generation-Recombination Noise: The Fundamental Sensitivity Limit for Kinetic Inductance Detectors”. en. In: *Journal of Low Temperature Physics* 167.3-4 (2012), pp. 335–340. ISSN: 0022-2291, 1573-7357. DOI: 10.1007/s10909-012-0519-5. URL: http://link.springer.com/10.1007/s10909-012-0519-5.

[56] P. J. De Visser et al. “Microwave-induced excess quasiparticles in superconducting resonators measured through correlated conductivity fluctuations”. en. In: *Applied Physics Letters* 100.16 (2012), p. 162601. ISSN: 0003-6951, 1077-3118. DOI: 10.1063/1.4704151. URL: https://pubs.aip.org/apl/article/100/16/162601/126067/Microwave-induced-excess-quasiparticles-in.

[57] P. J. De Visser et al. “Number Fluctuations of Sparse Quasiparticles in a Superconductor”. en. In: *Physical Review Letters* 106.16 (2011), p. 167004. ISSN: 0031-9007, 1079-7114. DOI: 10.1103/PhysRevLett.106.167004. URL: https://link.aps.org/doi/10.1103/PhysRevLett.106.167004.

[58] W. A. Phillips. “Two-level states in glasses”. In: *Reports on Progress in Physics* 50.12 (1987), pp. 1657–1708. ISSN: 0034-4885, 1361-6633. DOI: 10.1088/0034-4885/50/12/003. URL: https://iopscience.iop.org/article/10.1088/0034-4885/50/12/003.

[59] S. Kogan. *Electronic Noise and Fluctuations in Solids*. 1st ed. Cambridge University Press, 1996. ISBN: 978-0-511-55166-6. DOI: 10.1017/CBO9780511551666. URL: https://www.cambridge.org/core/product/identifier/9780511551666/type/book.

[60] O. Noroozian et al. “Two-level system noise reduction for Microwave Kinetic Inductance Detectors”. In: Stanford (California), 2009, pp. 148–151. DOI: 10.1063/1.3292302. URL: https://pubs.aip.org/aip/acp/article/1185/1/148-151/692603.

[61] J. Gao et al. “A semi-empirical model for two-level system noise in superconducting microresonators”. en. In: *Applied Physics Letters* 92.21 (2008). arXiv:0804.0467 [cond-mat], p. 212504. ISSN: 0003-6951, 1077-3118. DOI: 10.1063/1.2937855. URL: http://arxiv.org/abs/0804.0467.

[62] R. Barends et al. “Noise in NbTiN, Al, and Ta Superconducting Resonators on Silicon and Sapphire Substrates”. In: *IEEE Transactions on Applied Superconductivity* 19.3 (2009), pp. 936–939. ISSN: 1051-8223, 1558-2515. DOI: 10.1109/TASC.2009.2018086. URL: http://ieeexplore.ieee.org/document/5067054/.

[63] A. Bruno et al. “Reducing intrinsic loss in superconducting resonators by surface treatment and deep etching of silicon substrates”. en. In: *Applied Physics Letters* 106.18 (2015), p. 182601. ISSN: 0003-6951, 1077-3118. DOI: 10.1063/1.4919761. URL: https://pubs.aip.org/apl/article/106/18/182601/27784/Reducing-intrinsic-loss-in-superconducting.

[64] S. J. C. Yates et al. “Photon noise limited radiation detection with lens-antenna coupled microwave kinetic inductance detectors”. en. In: *Applied Physics Letters* 99.7 (2011), p. 073505. ISSN: 0003-6951, 1077-3118. DOI: 10.1063/1.3624846. URL: https://pubs.aip.org/aip/apl/article/122752.

[65] A. F. Andreev. “The Thermal Conductivity of the Intermediate State in Superconductors”. In: *Soviet Physics-JETP* 19.5 (1964), pp. 1228–1232.

[66] S. A. De Rooij et al. “Volume dependence of microwave-induced excess quasiparticles in superconducting resonators”. en. In: *Physical Review Applied* 24.2 (2025), p. 024007. ISSN: 2331-7019. DOI: 10.1103/6h78-ypgn. URL: https://link.aps.org/doi/10.1103/6h78-ypgn.

[67] B. Sacépé et al. “Disorder-Induced Inhomogeneities of the Superconducting State Close to the Superconductor-Insulator Transition”. en. In: *Physical Review Letters* 101.15 (2008), p. 157006. ISSN: 0031-9007, 1079-7114. DOI: 10.1103/PhysRevLett.101.157006. URL: https://link.aps.org/doi/10.1103/PhysRevLett.101.157006.

[68] M. V. Feigel’man and M. A. Skvortsov. “Universal Broadening of the Bardeen-Cooper-Schrieffer Coherence Peak of Disordered Superconducting Films”. en. In: *Physical Review Letters* 109.14 (2012), p. 147002. ISSN: 0031-9007, 1079-7114. DOI: 10.1103/PhysRevLett.109.147002. URL: https://link.aps.org/doi/10.1103/PhysRevLett.109.147002.

[69] J. Bueno et al. “Anomalous response of superconducting titanium nitride resonators to terahertz radiation”. en. In: *Applied Physics Letters* 105.19 (2014), p. 192601. ISSN: 0003-6951, 1077-3118. DOI: 10.1063/1.4901536. URL: https://pubs.aip.org/apl/article/105/19/192601/596555/Anomalous-response-of-superconducting-titanium.

[70] D. Filipovic, S. Gearhart, and G. Rebeiz. “Double-slot antennas on extended hemispherical and elliptical silicon dielectric lenses”. en. In: *IEEE Transactions on Microwave Theory and Techniques* 41.10 (1993), pp. 1738–1749. ISSN: 00189480. DOI: 10.1109/22.247919. URL: http://ieeexplore.ieee.org/document/247919/.

[71] Dassault Systèmes. *CST Studio Suite*. 2025. URL: https://www.3ds.com/products/simulia/cst-studio-suite.

[72] S. Dabironezare. “Fourier Optics Field Representations for the Design of Wide Field-of-View Imagers at Sub-millimetre Wavelengths”. PhD thesis. Delft University of Technology, 2020. DOI: 10.4233/UUID:23C845E1-9546-4E86-AE77-E0F14272517B. URL: http://resolver.tudelft.nl/uuid:23c845e1-9546-4e86-ae77-e0f14272517b.

[73] H. Zhang. “A GO/FO Tool for Analyzing Quasi-optical Systems in Reception”. PhD thesis. Delft University of Technology, 2018. URL: https://resolver.tudelft.nl/uuid:997558e6-7f32-493a-9f84-57895636db28.

[74] S. Dabironezare. *Private Communication*. 2025.

[75] J. Rahola. “Power Waves and Conjugate Matching”. In: *IEEE Transactions on Circuits and Systems II: Express Briefs* 55.1 (2008), pp. 92–96. ISSN: 1549-7747, 1558-3791. DOI: 10.1109/TCSII.2007.905420. URL: http://ieeexplore.ieee.org/document/4358636/.

[76] Sonnet Software. *Sonnet*. 2025. URL: https://www.sonnetsoftware.com/.

[77] K. Karatsu. *Private Communication*. 2026.

[78] J. R. Clem. “Inductances and attenuation constant for a thin-film superconducting coplanar waveguide resonator”. en. In: *Journal of Applied Physics* 113.1 (2013), p. 013910. ISSN: 0021-8979, 1089-7550. DOI: 10.1063/1.4773070. URL: https://pubs.aip.org/jap/article/113/1/013910/139968/Inductances-and-attenuation-constant-for-a-thin.

[79] J. J. A. Baselmans. *Private Communication*. 2025.

[80] R. Sproull, R. Lyon, and S. Trimberger. “The Caltech Intermediate Form for LSI Layout Description”. In: (1980). Version Number: Submitted. DOI: 10.7907/JMRGC-2F168. URL: https://authors.library.caltech.edu/doi/10.7907/jmrgc-2f168.

[81] MatthijsRoos. 2026. URL: https://github.com/MatthijsRoos/superconducting-detector.

[82] G. Rickayzen. *Theory of Superconductivity*. Interscience monographs and texts in physics and astronomy. Interscience Publishers, 1965. ISBN: 978-0-470-72050-9. URL: https://books.google.nl/books?id=PSIML4IxVrIC.

[83] R. M. J. Janssen et al. "High optical efficiency and photon noise limited sensitivity of microwave kinetic inductance detectors using phase readout". en. In: *Applied Physics Letters* 103.20 (2013), p. 203503. ISSN: 0003-6951, 1077-3118. DOI: 10.1063/1.4829657. URL: https://pubs.aip.org/aip/apl/article/130528.

[84] L. Ferrari et al. "Antenna Coupled MKID Performance Verification at 850 GHz for Large Format Astrophysics Arrays". en. In: *IEEE Transactions on Terahertz Science and Technology* 8.1 (2018), pp. 127–139. ISSN: 2156-342X, 2156-3446. DOI: 10.1109/TTHZ.2017.2764378. URL: http://ieeexplore.ieee.org/document/8123515/.

[85] C. M. Wilson and D. E. Prober. "Quasiparticle number fluctuations in superconductors". en. In: *Physical Review B* 69.9 (2004), p. 094524. ISSN: 1098-0121, 1550-235X. DOI: 10.1103/PhysRevB.69.094524. URL: https://link.aps.org/doi/10.1103/PhysRevB.69.094524.

A

Python model

The Python code used throughout this thesis is available at [81]. This appendix elaborates on two concepts applied in the code that are not yet addressed in this thesis.

A.1. Numerical derivation of $\Delta(T)$

The expression of gap energy as a function of temperature T is found by solving for Δ in the BCS self-consistency equation [28, 37]. Using $E = \sqrt{\xi^2 + \Delta^2}$, $d\xi = \frac{E}{\sqrt{E^2-\Delta^2}} dE$, and $\tanh \frac{E}{2k_B T} = 1 - 2f(E)$ with $f(E)$ being the Fermi function, we can rewrite to get,

$$\frac{1}{N_0 V_{sc}} = \int_0^{\hbar\omega_D} \frac{\tanh \frac{\sqrt{\xi^2+\Delta^2}}{2k_B T}}{\sqrt{\xi^2 + \Delta^2}} d\xi = \int_\Delta^{\hbar\omega_c} \frac{1 - 2f(E)}{\sqrt{E^2 - \Delta^2}} dE, \tag{A.1}$$

where V_{sc} is the potential energy corresponding to BCS electron-phonon interaction. The cut-off energy $\hbar\omega_c = \sqrt{(\hbar\omega_D)^2 + \Delta^2}$ is dominated by the Debye energy $\hbar\omega_D$, which is the maximum phonon energy. If we solve for $T = 0$, part of the integral vanishes as $f(E) \to 0$ in this limit. Therefore, we can find an expression for $\frac{1}{N_0 V_{sc}}$,

$$\int_{\Delta_0}^{\hbar\omega_c} \frac{1}{\sqrt{E^2 - \Delta_0^2}} dE = \ln \left| E + \sqrt{E^2 + \Delta_0^2} \right| \Bigg|_{\Delta_0}^{\hbar\omega_c} = \frac{1}{N_0 V_{sc}}. \tag{A.2}$$

Rewriting equation A.1 using this $T = 0$ term, we find,

$$\int_\Delta^{\hbar\omega_c} \frac{2f(E)}{\sqrt{E^2 - \Delta^2}} dE = \ln \left| E + \sqrt{E^2 + \Delta^2} \right| \Bigg|_\Delta^{\hbar\omega_c} - \ln \left| E + \sqrt{E^2 + \Delta_0^2} \right| \Bigg|_{\Delta_0}^{\hbar\omega_c}, \tag{A.3}$$

$$= \ln \frac{\Delta_0}{\Delta} - \ln \frac{\hbar\omega_c + \sqrt{(\hbar\omega_c)^2 + \Delta^2}}{\hbar\omega_c + \sqrt{(\hbar\omega_c)^2 + \Delta_0^2}}. \tag{A.4}$$

For weak-coupling superconductors, we can take $\hbar\omega_c \gg k_B T_c$ to find an approximation independent of material properties,

$$\ln \frac{\Delta(T)}{\Delta_0} + \int_{\Delta(T)}^\infty \frac{2f(E)}{\sqrt{E^2 - \Delta(T)^2}} dE = 0. \tag{A.5}$$

Switching to the normalized variables $\tilde{\Delta} = \Delta(T)/\Delta_0$ (where $\Delta_0 = \pi e^{-\gamma_E} k_B T_c$ with γ_E being the Euler gamma) and $\tilde{T} = T/T_c$, we yield the following that we can numerically solve to find $\Delta(T)$ [82],

$$\ln \tilde{\Delta} + 2 \int_0^\infty \left[\left(1 + \exp \left\{ \frac{-\pi^{-\gamma_E}}{\tilde{T}} \sqrt{\xi^2 + \tilde{\Delta}^2} \right\} \right) \sqrt{\xi^2 + \tilde{\Delta}^2} \right]^{-1} d\xi = 0. \tag{A.6}$$

A.2. Resonance condition change due to coupler capacitance

In section 2.2.2, we have introduced the theoretical description of a quarter-wave resonator. This section takes a closer look at how one can compensate for the change in resonance condition by adding the coupler capacitance. Using the definition of Q_c (equation 2.27), we can now define C_c as,

$$C_c = \frac{1}{\sqrt{\frac{2}{\pi} Q_c \omega_{1/4}^2 Z_0 Z_0^{\text{readout}}}} \overset{Z_0^{\text{readout}} = Z_0}{=\!=\!=} \frac{\sqrt{\frac{2}{\pi Q_c}}}{4 f_{1/4} Z_0}. \tag{A.7}$$

The quarter-wave resonator is capacitively coupled to the readout line, which means that the input impedance seen from the readout line converts to [53],

$$Z_{in} = \frac{1}{j\omega C_c} + Z_{in,\text{TL}} = \frac{4 Z_0 \frac{Q_i}{\pi}}{1 + 4Q_i^2 \left(\frac{\omega - \omega_{1/4}}{\omega_{1/4}}\right)^2} - j\left(\frac{1}{\omega C_c} + \frac{8 Z_0 \frac{Q_i^2}{\pi} \frac{\omega - \omega_{1/4}}{\omega_{1/4}}}{1 + 4Q_i^2 \left(\frac{\omega - \omega_{1/4}}{\omega_{1/4}}\right)^2}\right). \tag{A.8}$$

Applying the resonance condition from equation 2.23, we find two solutions for $\omega = \omega_0$ given large Q_i,

$$\frac{w_0 - w_{1/4}}{w_{1/4}} \approx -\sqrt{\frac{2}{\pi Q_c}} \sqrt{\frac{Z_0}{Z_0^{\text{readout}}}} \vee 0. \tag{A.9}$$

The first solution yields an effective shift in resonance frequency relative to the quarter-wave resonator due to the coupling capacitor. One can thus accurately compensate for the frequency shift by designing the quarter-wave resonator at a larger frequency. The effect of this resonance frequency shift and the resonance condition is visualized in figure A.1.
The second solution, $\omega_0 \approx \omega_{1/4}$, yields $\text{Re}\{Z_{in}\} = \text{Re}\{Z_0\} \frac{4Q_i}{\pi}$, which is too large to load the readout line [53].

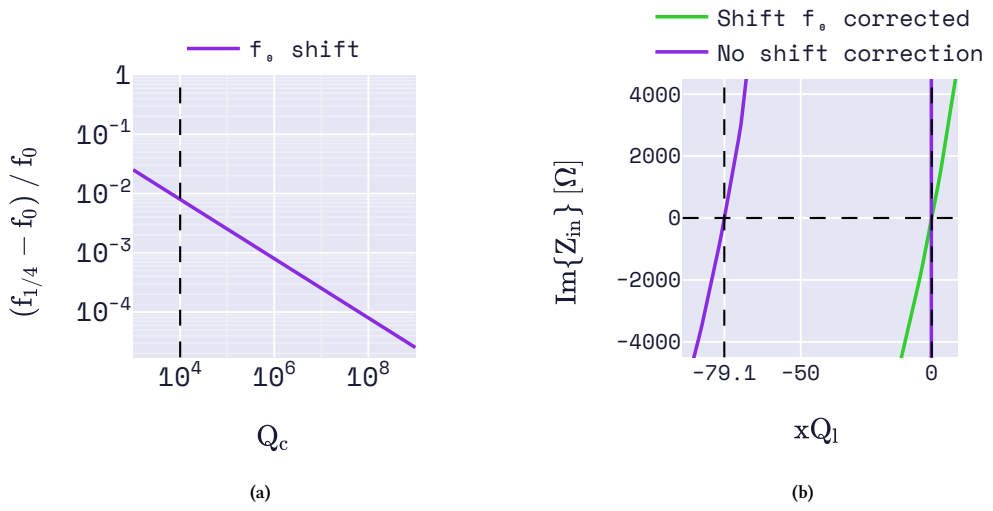

Figure A.1 – **(a)** The resonance frequency shift with respect to the quarter-wave resonance frequency due to the coupler capacitor. **(b)** The imaginary part of the input impedance of a capacitively coupled quarter-wave resonator, with and without compensation for the resonance frequency shift. The resonance condition $\text{Im}\{Z_{in}\} = 0$ is met for two frequencies, as is visible for the purple line (without compensation for shift). The solution at higher frequency (close to $xQ_l = 0$) has a large real input impedance, which therefore does not load the readout line. For these calculations, we use β-Ta ($T_c = 0.06$K and $\rho = 210\mu\Omega$·cm) and NbTiN ($T_c = 15$K and $\rho = 49\mu\Omega$·cm), and consider the CPW dimensions of figure 2.6. The resonance frequency is designed to be $f_0/f_c = 0.1$ at $T/T_c = 0.1$, and we use a coupling quality factor of $Q_c = 10^4$.

B

Interpretation of Mattis-Bardeen

In section 2.1.2, we introduced the Mattis-Bardeen description of complex conductivity (see equations 2.2 and 2.3). This appendix takes a closer look at the different parts of this equation. So, while this does not involve the direct derivations presented by Bardeen, Cooper, and Schrieffer [28] and Mattis and Bardeen [47], it does present a way to interpret their equations.
We can extend the quasiparticle density of states used in equation 2.1 to also incorporate superconducting electrons bound in Cooper-pairs, by converting to the (complex) superconducting density of states $\tilde{N}_s(E)$,

$$\frac{\tilde{N}_s(E)}{N_0} = \frac{E}{\sqrt{E^2 - \Delta^2}}. \tag{B.1}$$

Note that $\tilde{N}_s$ will be imaginary for $|E| < \Delta$, depicting the Cooper-paired superconducting electrons (see figure B.1a). This will eventually give rise to the imaginary part of σ.
The probability that a quasiparticle is excited in thermal equilibrium is described by the Fermi function, $f(E) = (1 + e^{E/k_B T})^{-1}$. When all electrons are in the ground state, for which $T = 0$, the Fermi function turns into a step function; going up to $T \geq T_c$, $\Delta = 0$ and the Fermi function becomes constant (see figure B.1b).

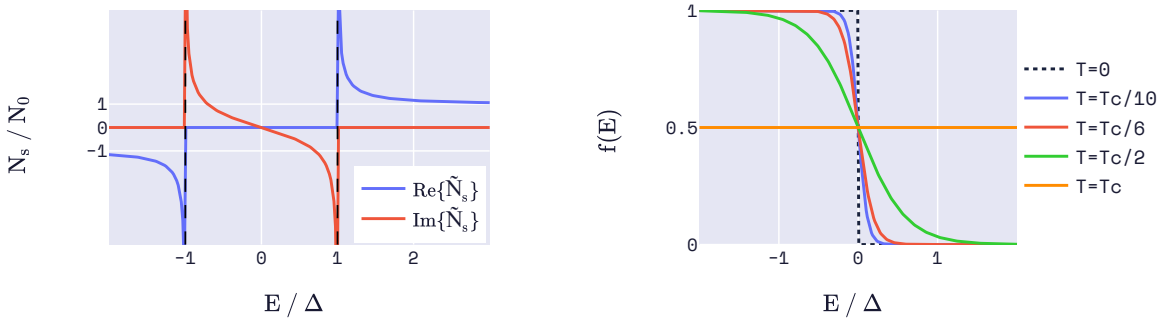

Figure B.1 – **(a)** The superconducting density of states. **(b)** The Fermi function for different temperatures T.

We estimate the transition rates between states at E and $E' = E + \hbar\omega$ as transitions for individual Cooper-pairs and quasiparticles (holds for the so-called dirty or the extremely anomalous limits). Written in a more general form, and not yet looking at different energy regimes, we find,

$$\frac{\sigma}{\sigma_N} \sim \frac{1}{\hbar\omega} \int \left(1 + \frac{\Delta^2}{EE'}\right) \Big[F(1 - F') - F'(1 - F)\Big] \frac{\tilde{N}_s(E)}{N_0} \frac{\tilde{N}_s(E')}{N_0} dE. \tag{B.2}$$

Here, $1 + \Delta^2/(EE')$ is the BCS coherence factor, $[F(1 - F') - F'(1 - F)] = [F - F']$ represents the net absorption, and $\tilde{N}_s(E)\tilde{N}_s(E')/(N_0)^2$ the product of the density of states at E and E'. We have to add the $1/\hbar\omega$ term in front of the integral to make sure we will normalize to σ_N.

For the net absorption, F represents the distribution of the electron-like quasiparticles and $1-F$ the distributions of hole-like quasiparticles. For an excited state, we can simply use $F = f(E)$ and $F' = f(E')$ for each of the two quasiparticles. For the ground state, we use $F = 1$ and $F' = 0$ for the Cooper-pair. Therefore, the transition from Cooper-pair to two quasiparticles turns into $[1 - 2f(E+\hbar\omega)]$, and the transition from two quasiparticles to a higher energy state turns into $[2f(E) - 2f(E+\hbar\omega)]$.
We can bundle the coherence factor and the density of states to create an effective density of states, which we denote by $g(E)$,

$$g(E) = \left(1 + \frac{\Delta^2}{EE'}\right)\frac{\tilde{N}_s(E)}{N_0}\frac{\tilde{N}_s(E')}{N_0} = \frac{E(E+\hbar\omega)+\Delta^2}{\sqrt{E^2-\Delta^2}\sqrt{(E+\hbar\omega)^2-\Delta^2}}. \tag{B.3}$$

The effective density of states is visualized for different photon energies in figure B.2. For us to properly set up equations 2.2 and 2.3, we have to realize that,

- $g(E) = \mathrm{Im}\{g(E)\}$ for $E \in [\max(\Delta - \hbar\omega;\ -\Delta), \Delta]$, and we can use a sign change to take a factor $-j$ out of $1/\sqrt{E^2-\Delta^2}$, which is the one used to complete the formulation $\sigma = \sigma_1 - j\sigma_2$;
- $g(E) < 0$ for $E \in [\min(\Delta - \hbar\omega; -\Delta),\ -\Delta]$, so to get the increase in σ_1 we need to redefine the real part of $\tilde{N}_s$ to be an even function, as it is now odd, or simply multiply by -1 in this interval.

This completes the formulation, and we can summarize the interpretation of equations 2.2 and 2.3:

- the first integral of σ_1 relates to absorption of photons by thermally excited electrons;
- the second integral of σ_1 depicts pair-breaking of Cooper-pairs ($\hbar\omega \geq 2\Delta$);
- σ_2 describes the reactive response, rather than the dissipative response depicted by σ_1.

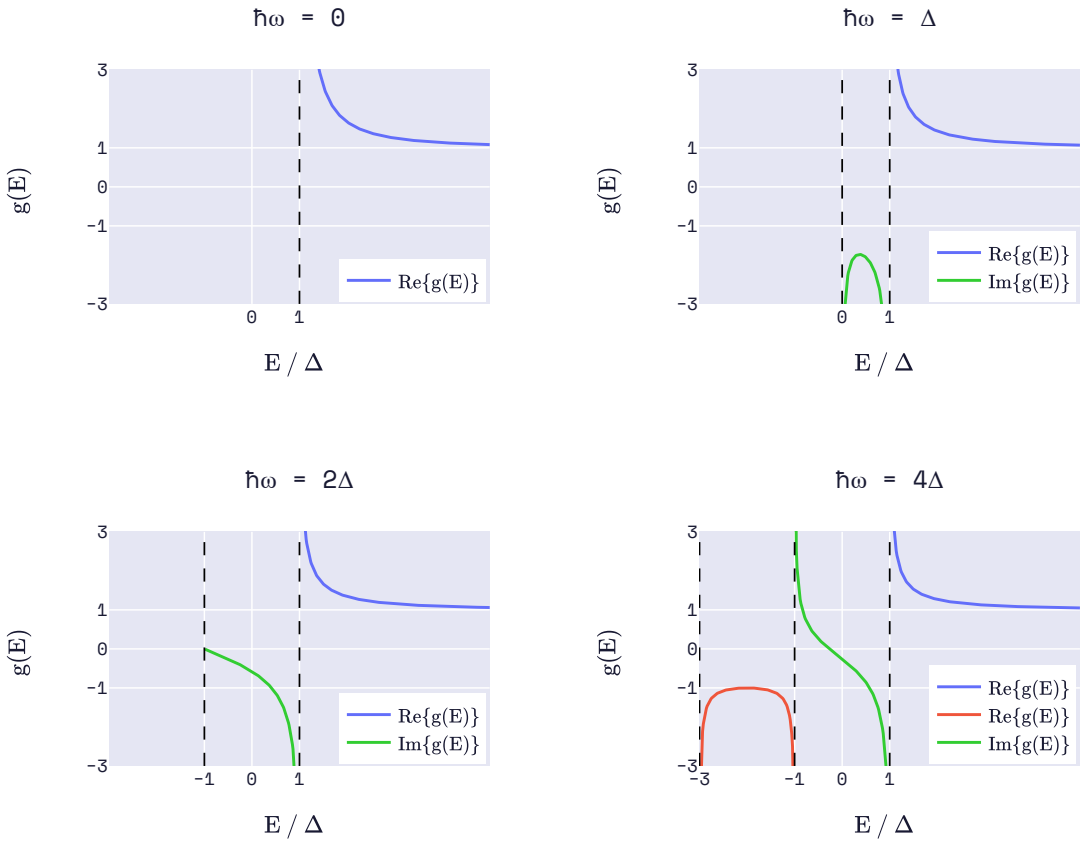

Figure B.2 – The behavior of $g(E)$ for different photon energies $\hbar\omega$. The blue curve represents any quasiparticles that exist for $E > \Delta$, where $g(E) = \mathrm{Re}\{g(E)\}$. The green curve represents the inductive effect of the Cooper-pairs for $E \in [\max(\Delta - \hbar\omega;\ -\Delta), \Delta]$, where $g(E) = \mathrm{Im}\{g(E)\}$. Only for $\hbar\omega > 2\Delta$, the green curve shows an energy region $E \in [-\Delta, (-\hbar\omega/2\Delta + \sqrt{(\hbar\omega/2\Delta)^2 - 1})\Delta]$ in which $g(E)$ is positive and imaginary, showing the effect of Cooper-pairs being broken. This is why only for $\hbar\omega > 2\Delta$ the red curve starts to appear, representing quasiparticles existing because of pair-breaking for $E \in [\min(\Delta - \hbar\omega; -\Delta),\ -\Delta]$, where $g(E) = \mathrm{Re}\{g(E)\}$.

C

Effective relative permittivity of a superconducting CPW

We defined the effective relative permittivity of a CPW due to the geometry of a coplanar waveguide as $\epsilon_{\text{eff,geo}} \approx (1+\epsilon_r)/2$ (see equation 2.9). However, this definition does not contain the effect kinetic inductance of the transmission line has on the effective relative permittivity.

For the wavelength inside of a transmission line, we can use $\lambda = v_{\text{phase}}/f$. This wavelength is reduced with a factor $\sqrt{\epsilon_{\text{eff}}} = c/v_{\text{phase}}$ compared to the wavelength in vacuum. For a lossless CPW, $v_{\text{phase}} = 1/\sqrt{L_l C_l}$ such that we can define $\epsilon_{\text{eff}} = c^2 L_l C_l$. So, the effective relative permittivity for a superconducting CPW is a function of frequency. We can continue to substitute the kinetic inductance fraction (as defined in equation 2.16) to find a redefinition for a lossless CPW,

$$\epsilon_{\text{eff}} = c^2(L_{g,l} + L_{k,l})C_l = c^2\Big(\frac{L_{k,l} + L_{g,l}}{L_{g,l}}\Big)L_{g,l}C_l = \frac{\epsilon_{\text{eff,geo}}}{1-\alpha_k}. \tag{C.1}$$

This implies that f_0 becomes smaller for larger α_k. Namely, ϵ_{eff} affects the resonance frequency of a superconducting quarter-wave resonator as it is defined through $f_0 \propto v_{\text{phase}}/4l \propto \sqrt{1-\alpha_k}$. This is also used in equation 4.3 to find α_k.

D

Transmission line theory

For the analysis of microwave circuits, it is useful to use transmission line theory. To understand how the standard equations from this theory are used throughout this thesis, we explain and derive the basics in this appendix based on methods described in [52].

D.1. Propagating waves

A transmission line can be schematically represented by a two-wire line. We consider a line of length Δz containing lumped elements R, L, G, and C, for which an equivalent circuit is shown in figure D.1. Here, L represents the self-inductance of the two conducting lines. The lines, being in proximity of each other, also induce a shunt capacitance C. R and G represent the loss in the line: R is the series resistance, and G the shunt conductance due to dielectric loss in the material between the lines.

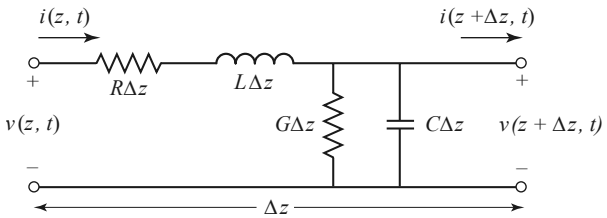

Figure D.1 – Circuit representation of a transmission line of length Δz, including its voltage and current definitions. Quantities for R, L, G, and C are given per unit length. Image taken from [52].

To emphasize that the quantities are given per unit length, we switch to using R_l, L_l, G_l, and C_l. Applying the Kirchoff's voltage and current laws to the circuit representation, dividing by Δz and taking the limit of $\Delta z \to 0$ yields the well-known telegrapher equations,

$$\frac{\partial v(z,t)}{\partial z} = -R_l i(z,t) - L_l \frac{\partial i(z,t)}{\partial t}, \tag{D.1}$$

$$\frac{\partial i(z,t)}{\partial z} = -G_l v(z,t) - C_l \frac{\partial v(z,t)}{\partial t}. \tag{D.2}$$

The telegrapher equations reduce to wave equations for $V(z)$ and $I(z)$ when we consider a sinusoidal steady-state condition with cosine phasors,

$$\frac{d^2V(z)}{dz^2} - \gamma^2 V(z) = 0, \tag{D.3}$$

$$\frac{d^2I(z)}{dz^2} - \gamma^2 I(z) = 0, \tag{D.4}$$

where we define the complex propagation constant as in equation 2.18.

Now, we can evaluate solutions of these wave equations as the sum of two traveling waves, one in the $+z$ and one in the $-z$ direction,

$$V(z) = V_0^+ e^{-\gamma z} + V_0^- e^{\gamma z}, \tag{D.5}$$
$$I(z) = I_0^+ e^{-\gamma z} + I_0^- e^{\gamma z}. \tag{D.6}$$

One can show that we can rewrite the current to be $I(z) = \frac{\gamma}{R+j\omega L}(V_0^+ e^{-\gamma z} - V_0^- e^{\gamma z})$, which allows us to introduce the characteristic impedance Z_0 as in equation 2.17. The characteristic impedance thus relates the voltage and current factors in the equations for traveling waves D.5 and D.6. Equation D.6 can be rewritten as,

$$I(z) = \frac{V_0^+}{Z_0} e^{-\gamma z} - \frac{V_0^-}{Z_0} e^{\gamma z}. \tag{D.7}$$

Any transmission line can be built from a cascade of the infinitesimal line sections considered in figure D.1. Subsequently, we can continue to use the representation of a transmission line given a propagation constant γ and a characteristic impedance Z_0.

D.2. Termination and reflection of waves

Consider the terminated transmission line (see figure 2.7). We use the traveling waves from equations D.5 and D.7, with the $+z$ direction being toward the load impedance Z_L, where we will also put the origin.
At the origin, we can find the amplitude ratio between the incident (V_0^+) and the reflected (V_0^-) wave. First, we express the load impedance in terms of the total voltage and current,

$$Z_L = \frac{V(z=0)}{I(z=0)} = \frac{V_0^+ + V_0^-}{V_0^+ - V_0^-} Z_0. \tag{D.8}$$

Rewriting to find the ratio between V_0^- and V_0^+, which we define as the voltage reflection coefficient Γ_v, yields,

$$\Gamma_v = \frac{V_0^-}{V_0^+} = \frac{Z_L - Z_0}{Z_L + Z_0}. \tag{D.9}$$

Considering power waves, we find a different expression. We refer to the derivation in [75], to obtain,

$$\Gamma_p = \frac{V - Z_0^* I}{V + Z_0 I} = \frac{Z_L - Z_0^*}{Z_L + Z_0}, \tag{D.10}$$

which is the same as equation D.9 for real-valued Z_0.
The ratio of incident to reflected power equals $|\Gamma|^2$, to become the power reflection. Equivalently, power transmitted to the load P_L is now,

$$\frac{P_L}{P_i} = 1 - |\Gamma|^2 \tag{D.11}$$

Γ_v, obtained through voltage reflection, can be generalized to any z along the line. For instance, at the input impedance Z_{in}, which is at $z = -l$, we find,

$$\Gamma_v(z=-l) = \frac{V_0^- e^{-\gamma l}}{V_0^+ e^{\gamma l}} = \Gamma_v(0) e^{-2\gamma l}. \tag{D.12}$$

Similarly, we can find the expression for Z_{in},

$$Z_{in} = \frac{V(z=-l)}{I(z=-l)} = Z_0 \frac{e^{\gamma l} + \frac{V_0^-}{V_0^+} e^{-\gamma l}}{e^{\gamma l} - \frac{V_0^-}{V_0^+} e^{-\gamma l}} = Z_0 \frac{Z_L + Z_0 \tanh \gamma l}{Z_0 + Z_L \tanh \gamma l}. \tag{D.13}$$

Where we rewrote Z_{in} in the last step to the form of equation 2.21 by substitution of the voltage reflection coefficient from equation D.9.

D.3. Network analysis using matrices

It is rather convenient to evaluate transmission lines as transmission matrices, otherwise known as ABCD-matrices (see figure D.2). In a two-port network, an ABCD-matrix relates how voltage and current transmits from port 1 to port 2,

$$\begin{cases} V_1 = AV_2 + BI_2 \\ I_1 = CV_2 + DI_2 \end{cases} \quad \Rightarrow \quad \begin{bmatrix} V_1 \\ I_1 \end{bmatrix} = \begin{bmatrix} A & B \\ C & D \end{bmatrix} \begin{bmatrix} V_2 \\ I_2 \end{bmatrix} \tag{D.14}$$

As we want to be able to put different circuit elements in series, we can simply cascade the respective matrices to find the transmission matrix corresponding to the entire network.

Figure D.2 – ABCD-matrix representation of a two-port network.

Three useful ABCD-matrices, corresponding to the components in figure D.3,

$$\begin{bmatrix} A & B \\ C & D \end{bmatrix} = \begin{cases} \text{Series impedance Z} & \begin{bmatrix} 1 & Z \\ 0 & 1 \end{bmatrix} \\ \text{Shunt admittance Y} & \begin{bmatrix} 1 & 0 \\ Y & 1 \end{bmatrix} \\ \text{Transmission line} & \begin{bmatrix} \cosh \gamma l & Z_0 \sinh \gamma l \\ \frac{\sinh \gamma l}{Z_0} & \cosh \gamma l \end{bmatrix} \end{cases} \tag{D.15}$$

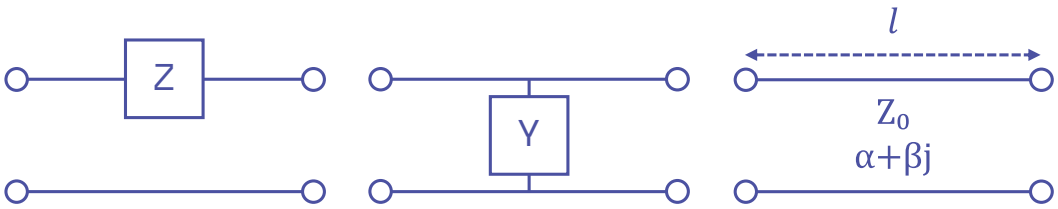

Figure D.3 – Different circuit components. From left to right: a series impedance Z, a shunt admittance Y (reciprocal of shunt impedance Z), and a transmission line of length l.

Two other useful network representations are the impedance matrix Z_{ij} and the scattering matrix S_{ij}. For a two-port network, these are defined as,

$$\begin{bmatrix} V_1 \\ V_2 \end{bmatrix} = \begin{bmatrix} Z_{11} & Z_{12} \\ Z_{21} & Z_{22} \end{bmatrix} \begin{bmatrix} I_1 \\ I_2 \end{bmatrix} \tag{D.16}$$

$$\begin{bmatrix} V_1^- \\ V_2^- \end{bmatrix} = \begin{bmatrix} S_{11} & S_{12} \\ S_{21} & S_{22} \end{bmatrix} \begin{bmatrix} V_1^+ \\ V_2^+ \end{bmatrix} \tag{D.17}$$

The scattering matrix shows how waves are exchanged between the ports: S_{11} and S_{22} representing the signal reflected back to its own port; S_{12} and S_{21} representing signal transmitted from one to the other port.
Using the impedance matrix, one can easily determine the input impedance given a load impedance Z_L,

$$Z_{in} = Z_{11} - \frac{Z_{12}Z_{21}}{Z_{22} + Z_L}. \tag{D.18}$$

S_{11} directly relates to the input impedance, equating to the reflection coefficient of equation D.9 and D.10 for voltage and power waves, respectively,

$$S_{11} \overset{V}{=} \frac{Z_{in} - Z_0}{Z_{in} + Z_0}, \qquad S_{11} \overset{P}{=} \frac{Z_{in} - Z_0^*}{Z_{in} + Z_0} \tag{D.19}$$

E

Lens antenna design for 350GHz

Besides the chip designs for 70GHz, we did an analysis similar to the one in chapter 5 to create designs for 350 GHz. We have already shown how we found a compromise in the different design constraints by choosing a β-Ta/NbTiN hybrid 2-3-2 CPW design (see section 4.1.1). While it was mostly the large magnitude of the characteristic impedance that was causing issues in finding this compromise, we do not really have the same issue at higher frequencies. One can see in figure E.1 how the characteristic impedance of the CPW is evaluated at different frequencies, which results in the cases shown in figure E.2 for both 70GHz and 350GHz, where we clearly see that we found a closer impedance match for the antenna design at 350GHz.
This appendix is a collection of figures meant to show all necessary information to get to the antenna design shown in figure E.6, which collectively follow an analysis completely equivalent to the one performed for 70GHz. Similarly to the presented design for 70GHz, the 350GHz design was optimized for power transmission from the antenna to the narrow CPW through the use of the voltage wave definition, whereas the power wave definition should have been considered instead (see equation 3.5).

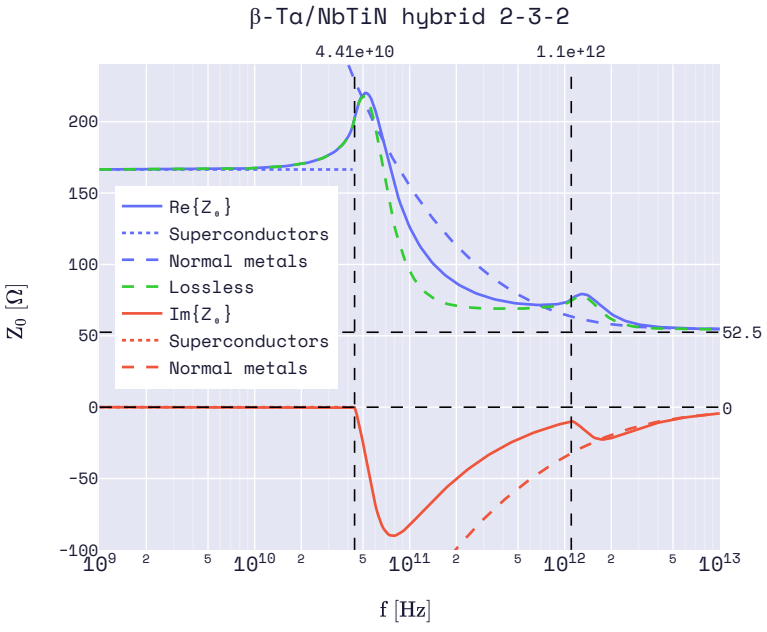

Figure E.1 – Characteristic impedance of a β-Ta/NbTiN hybrid 2-3-2 CPW over several order of magnitude in frequency at $T = 0.06$K. Superconducting (dotted) and normal metal limits (dashed), as well as the lossless approximation (green dashed) are plotted alongside the Z_0 found using the Mattis-Bardeen equations (solid lines). For the lossless approximation in particular, we take $Z_0 = \sqrt{L/C}$, which is real-valued. In this figure, we used β-Ta with $d = 100$nm and $\rho_N = 49\mu\Omega\cdot$cm, and NbTiN with $d = 200$nm and $\rho_N = 217\mu\Omega\cdot$cm. Vertical dashed lines were added for the frequencies corresponding to the minimum energy required for breaking Cooper-pairs ($f_c \approx 44.1$GHz for β-Ta; $f_c \approx 1.1$THz for NbTiN). Horizontal dashed lines were added for the high-frequency limits.

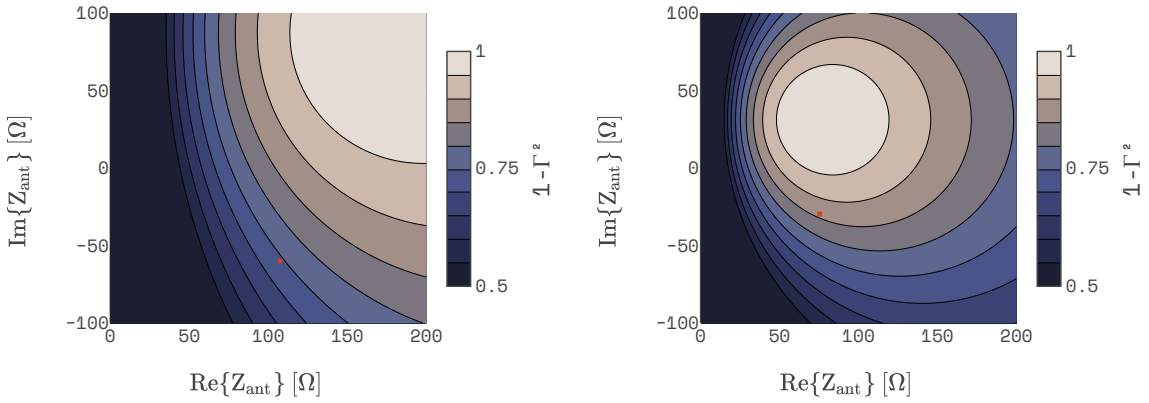

(a) 70GHz **(b)** 350GHz

Figure E.2 – Contour plots of the power transmission between antenna input impedance (Z_{ant}) and the characteristic impedance of the CPW (see figure E.1). Given the CPW characteristic impedance at **(a)** 70GHz and **(b)** 350GHz, the transmission is plotted in the complex plane of Z_{ant}. $Z_{ant}[f = 70\text{GHz}] = 108 - 60.3j\ \Omega$ and $Z_{ant}[f = 350\text{GHz}] = 75.8 - 29.3j\ \Omega$ are respectively added to (a) and (b) as orange markers to show the input impedance of the chosen antenna designs. This figure uses equation 3.5.

For the 350GHz design, we have the band-pass filter shown in figure E.3a available. Additionally, we have a 2×2 lens array consisting of $D = 2$mm elliptical lenses (with 2mm spacing between the midpoints of each lens), of which a single lens profile is shown in figure E.3b.

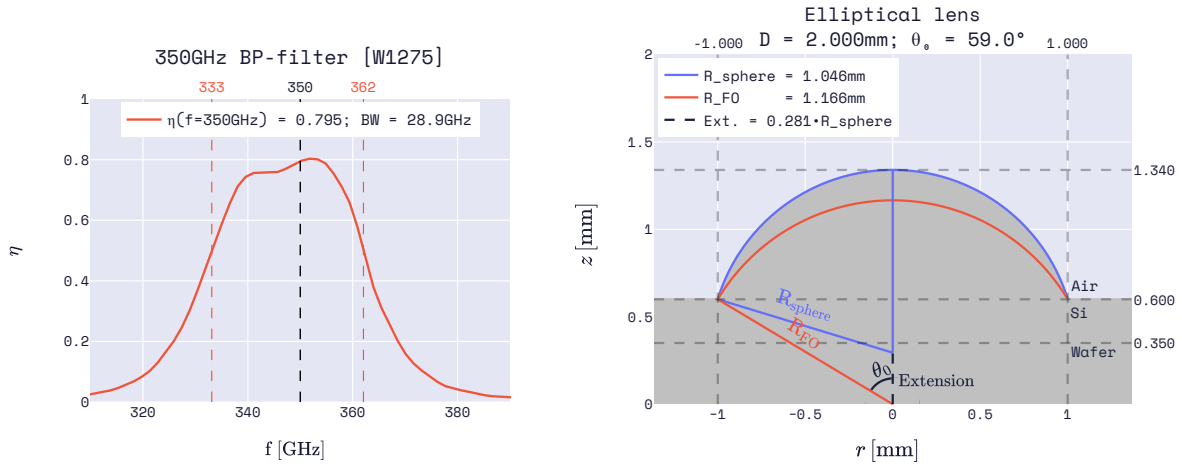

(a) **(b)**

Figure E.3 – **(a)** Power transmission as a function of frequency for the band-pass filter used for the frequency range centered at 350GHz. The bandwidth of the band-pas filter is defined by the range in which the power transmitted is larger than 50% or -3dB. **(b)** The elliptical lens used and the geometry of its equivalent extended hemispherical lens mounted on the backside of the chip's wafer ($t_{wafer} = 350\mu$m). The antenna will be centered in the origin.

We performed the same impedance matching analysis (see the subfigures in figure E.4) and used similar reasoning as in section 4.1.1 to get to the hybrid 2-3-2 design. Closely matching the characteristic impedance of the CPW, we find a twin-slot antenna design shown in figure E.6. As the width of the antenna will be shorter than the minimum attenuation length that we will use (at -10dB), we do not have too much of a constraint on the gap size defined by d_{ant}. Namely, for an attenuation of -10dB at $f = 350$GHz, we need $l_{narrow} \approx 106\mu$m. Given the bandwidth defined by the band-pass filter, we obtain the coupling shown in figure E.5.
For the optimized antenna design shown in figure E.6a, the far-field beam pattern is evaluated for the corresponding lens antenna, see figure E.6b. Additionally, the near-field electric field is evaluated at different cross sections of the beam, shown in figure E.7. The real part of the antenna impedance is determined in CST for different box sizes, shown in figure E.8. Here, the same effect as in figure 4.13 is visible where the effects of box

dimensions start to become insignificant once they surpass a quarter wavelength in vacuum. In figure E.9, we see one of the three chip designs for 350GHz, namely that of chip 7 which is designed for −10dB attenuation (see figure 5.3).

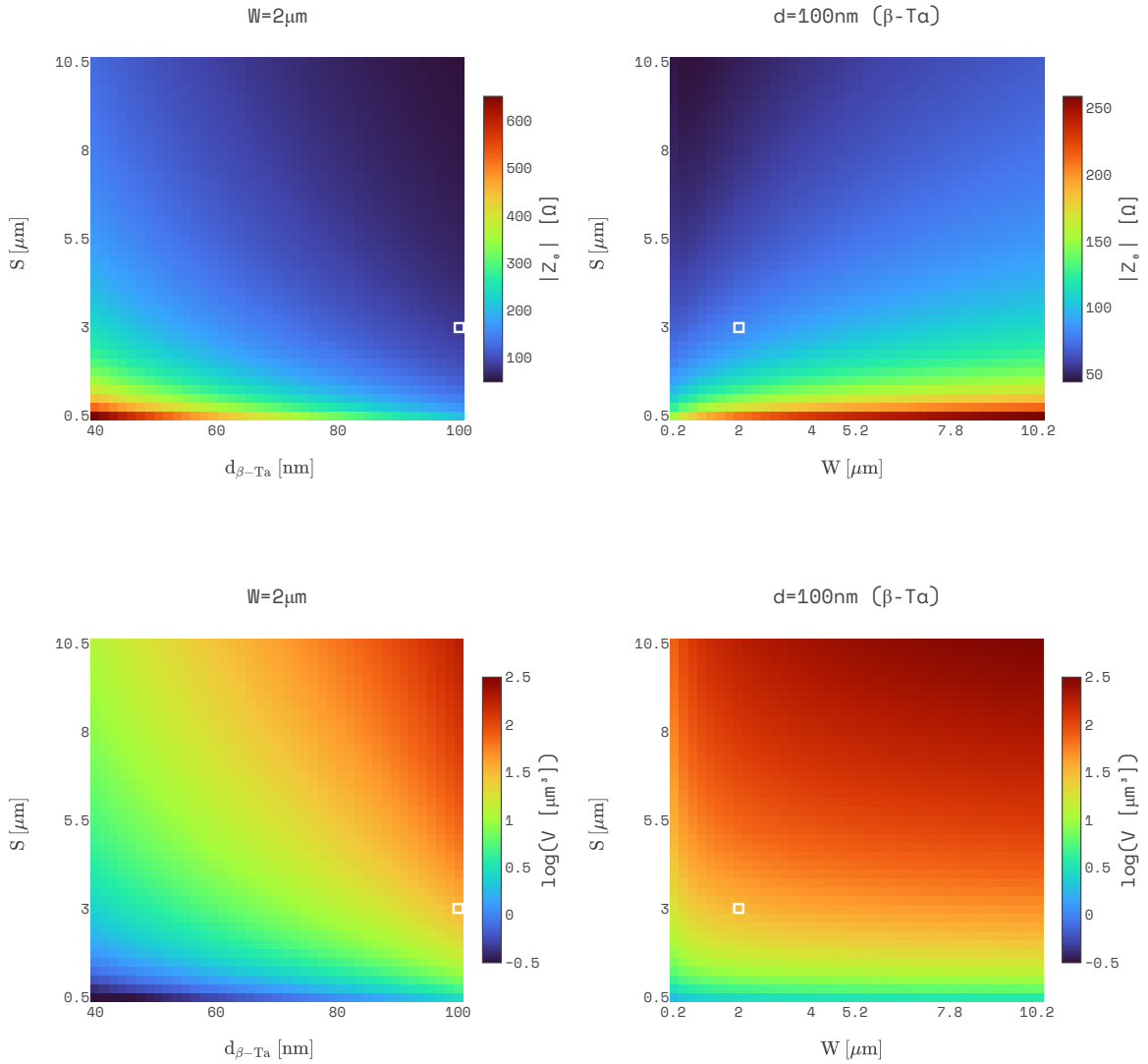

Figure E.4 – Analysis of CPW dimensions for a β-Ta/NbTiN hybrid CPW, evaluated at $f = 350$GHz and $T = 0.06$K. The magnitude of the characteristic impedance Z_0 (top row), and the required volume V to attain −10dB attenuation (bottom row), all given varying film thicknesses $d_{\beta-\mathrm{Ta}}$ and central line widths S (left column) and varying gap W and central line widths S (right column). For the left column, we use a first-order interpolation between $\rho_N = 210\mu\Omega\cdot$cm for $d_{\beta-\mathrm{Ta}} = 40$nm and $\rho_N = 49\mu\Omega\cdot$cm for $d_{\beta-\mathrm{Ta}} = 100$nm. For NbTiN ($d = 200$nm), we use $\rho_N = 217\mu\Omega\cdot$cm. Orange markers are used to indicate the 2-3-2 CPW using $d_{\beta-\mathrm{Ta}} = 100$nm.

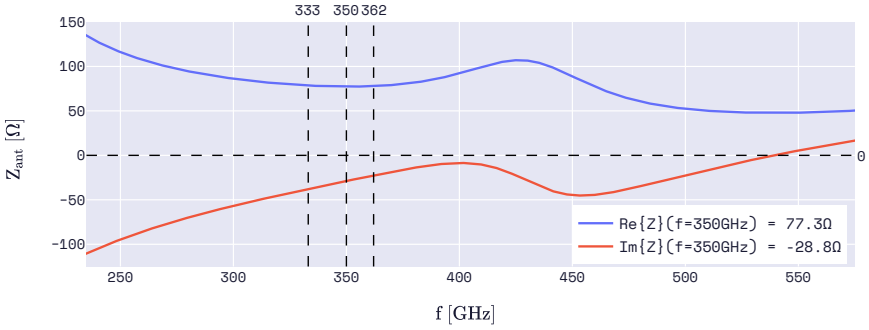

(a)

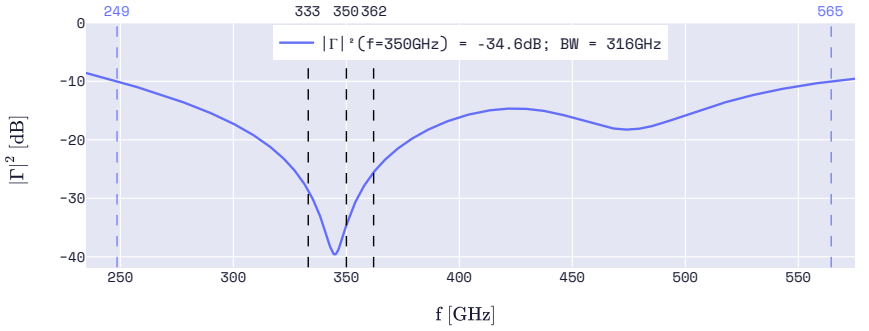

(b)

Figure E.5 – **(a)** Antenna impedance at its port, and **(b)** the reflection defining the scattering between the CPW and antenna impedances, evaluated using the voltage wave definition. Vertical dashed lines are used to indicate the antenna bandwidth (blue) and band-pass filter bandwidth from figure E.3a (black).

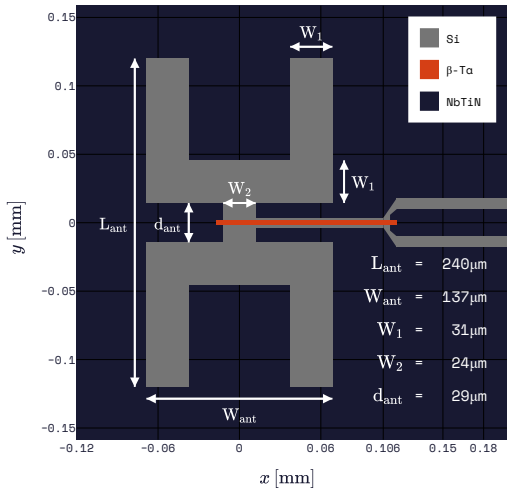

(a)

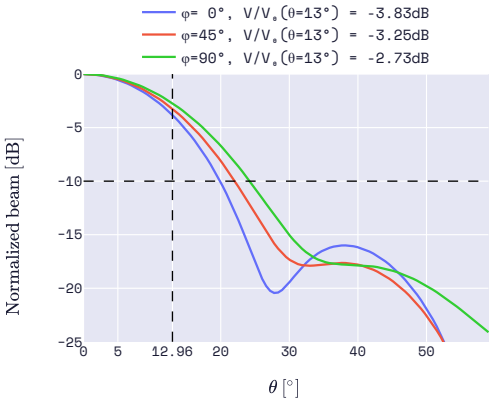

(b)

Figure E.6 – **(a)** Schematic representation of the twin-slot antenna design for 350GHz with its five determining dimensions listed. The length L_{ant} and width W_{ant} are the main determining factors for the antenna to match well to a 350GHz source. For reference, the CPW structure has been drawn as well, with the β-Ta (orange) in the narrow CPW stretching from the NbTiN ground(dark blue) on the left of the origin to $x \approx 106.0$µm, which corresponds to an attenuation of -10dB. d_{ant} has been chosen such that it is sufficiently wide to contain the wide 8-20-8 NbTiN CPW. The areas without superconducting film will have their Si directly exposed (gray). **(b)** (Normalized) beam pattern for for the lens antenna consisting of the lens in figure E.3b coupled to the antenna in (a), which is placed in its origin. Three different angles φ with respect to the x-axis are shown. A vertical dashed line is used to indicate the opening angle within the setup given the source at minimum distance from the top of the lens (see figure 4.5).

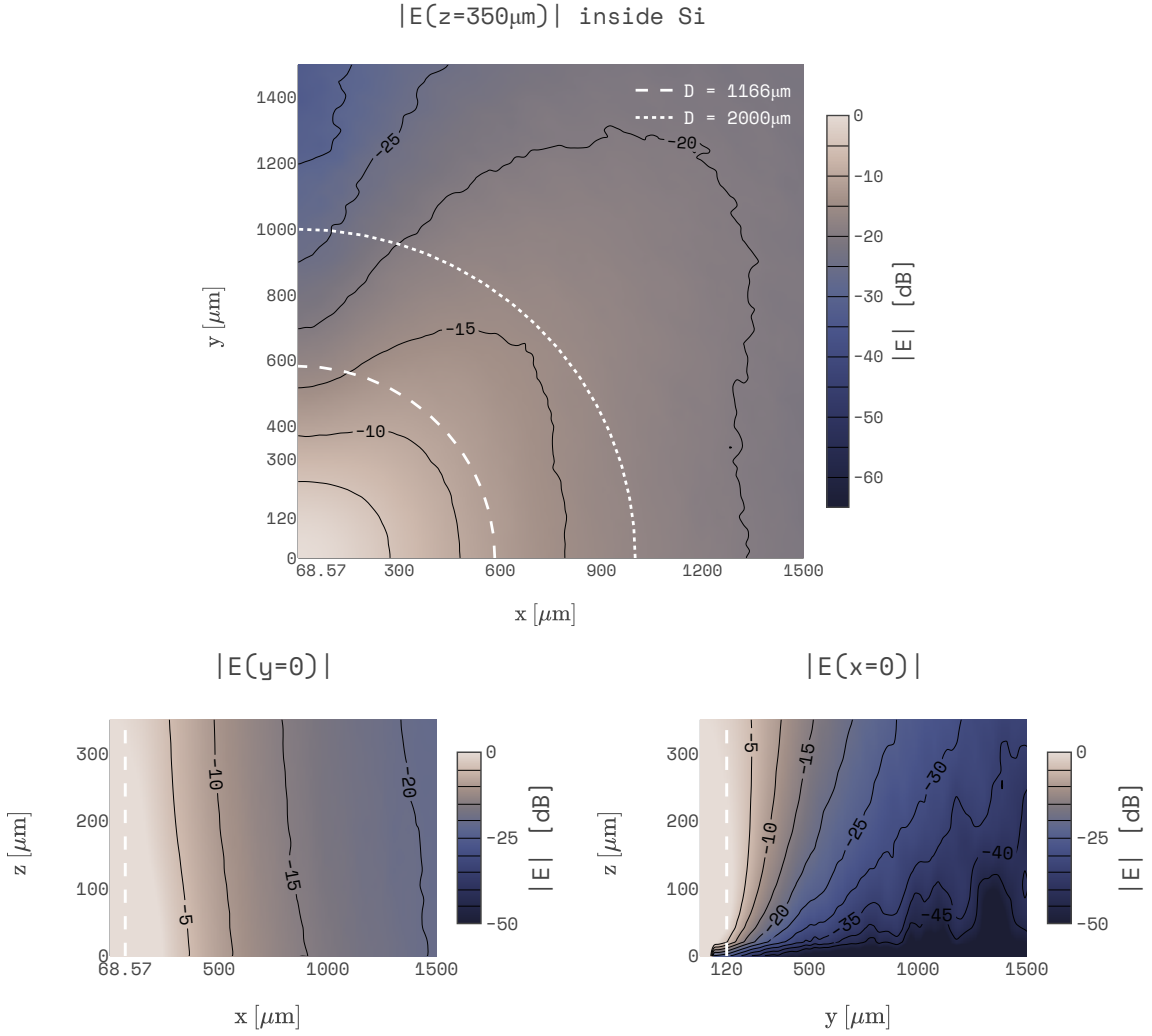

Figure E.7 – Cross sections of the magnitude of the normalized electric field as transmitted by the antenna, shown in three planes: **(top)** the x-y plane at $z = 350\mu m$, equivalent to the backside of the chip's substrate, **(bottom left)** the x-z plane, and **(bottom right)** the y-z plane. Each figure only shows the first quadrant and can be extrapolated using symmetries within the substrate (Si) for $z > 0$. All have the antenna placed at the origin. The top figure has two circle indicators for different diameters. The smaller being the diameter of the aperture one finds when taking the cross section of the cone defined by the lens aperture and the origin at $z = 350\mu m$ (cone defined by R_{FO} in figure E.3b); the larger one being the diameter chosen for the aperture in the backside mesh, which is chosen to be of the same size as chosen for the 70GHz design. The bottom figures have vertical dashed lines to indicate half the length and width of the antenna.

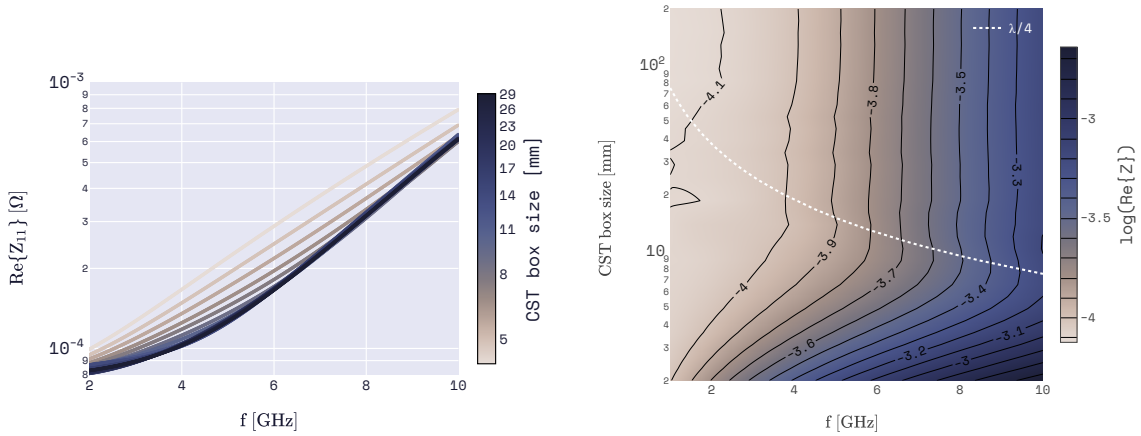

(a) (b)

Figure E.8 – **(a)** The real part of the antenna impedance for the 350GHz design over readout frequencies. Different box dimensions in the setup in CST were used for to determine the antenna impedance. The box size represents the side of the cubic box in which the antenna is centered. **(b)** The same data, but now shown as a heatmap with the box size on the y-axis. A white dotted line is added showing the quarter wavelength $\lambda/4 = c/4f$ at these readout frequencies.

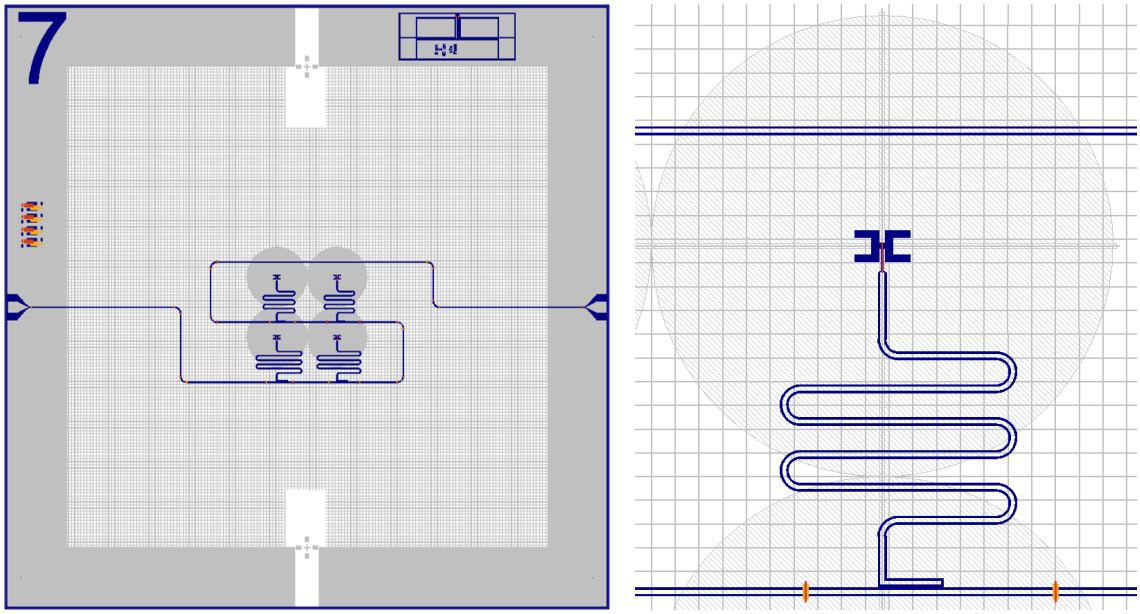

(a) (b)

Figure E.9 – **(a)** Generated mask for chip 7. Dark blue layer is a negative of NbTiN, orange positive of β-Ta, and yellow positive of polyimide used for the bridges. The gray layer is used to show the negative of β-Ta on the backside of the chip, where the mesh is. The mesh structure has dimensions $w = 100\mu$m and $g = 3\mu$m, which was optimized for 350GHz in a previous project [77]. A 2mm hole in the mesh can be seen on the four KIDs with design resonance frequencies [2.50, 2.60, 3.00, 3.50]GHz. **(b)** A zoom-in of the (top right) KID designed for $f_0 = 3$GHz.

F

Outlook on experimental evaluation

The designs shown in chapter 5 are currently being fabricated. This chapter highlights measurements that will have to be performed to experimentally evaluate the design, combining methods from previous research [30, 43, 83, 84].

Superconducting film properties

For our designs, we have assumed certain values for ρ_N, T_c and d to characterize both NbTiN and β-Ta using BCS and MB-theory. As these values vary based on fabrication, it is useful to determine the values that we find on our chips and use them in deriving the properties of the KIDs.

We have added structures on the chip wafers specifically for the purpose of determining the thickness of the thin films. Namely, we have added overlapping symbols of the three different deposited materials to create a relief profile in the overlapping films (see figure 5.2). Hence, a profilometer can help us determine film thicknesses $d_{\beta-\text{Ta}}$ and d_{NbTiN}.

Both ρ_N and T_c can be found using other structures added on the chip wafers, namely DC chips. These DC chips allow for a 4-point probe measurement across a film strip of width w and length l. A schematic of such a structure on a DC chip is shown in figure F.1. We have added additional DC structures on each chip, of which the placement is visible in figure 5.2.
The resistance is calculated as the difference in voltage divided by the difference in induced current [43],

$$R = \frac{V^+ - V^-}{I^+ - I^-}. \tag{F.1}$$

Performing a sweep in temperature allows us to observe the transitioning from superconducting to normal state conducting when measuring the resistance. The transitioning point at $R(T = T_c) = R_N/2$ defines T_c. From this, we can also find R_N, which is the maximum of $R(T)$ reached for $T > T_c$. R_N relates to $\rho_N = 1/\sigma_N$ through $\rho_N = R_s d$, where $R_s = R_N w/l$.

Resonator properties

Knowing the material characteristics of the films on our chip, we can turn to the detectors themselves. Performing a sweep in temperature, we can use the changes in S_{21} to measure the amplitude and phase responsitivities of the detectors (see equations 2.35 and 2.36, respectively). Using the dependence on temperature for n_{qp} and therefore for the responsivities, we can find the expressions for $Q(T)$, $(1/Q_i)(T)$, and $\delta\omega_0/\omega_0$. Ultimately, we thus obtain $Q_i(T)$ and $f_0(T)$.

As $\omega_0 \propto \sqrt{1-\alpha_k}$, we can also find an expression of the kinetic inductance fraction (see equation 2.16). We determine $\alpha_k(0)$ through,

$$\frac{f_0(0)}{f_0(T)} = \frac{\sqrt{1-\alpha_k(0)}}{\sqrt{1-\alpha_k(T)}} = \sqrt{\frac{L_k(T)+L_g}{L_k(0)+L_g}} \Rightarrow \left(\frac{f_0(0)}{f_0(T)}\right)^2 - 1 = \alpha_k(0)\left(\frac{L_k(T)}{L_k(0)} - 1\right). \tag{F.2}$$

After we have found expressions for $Q_i(T)$ and α_k, we can compare the KIDs with an antenna at their load to those that are shorted and compare it to what is shown in figure 5.5.

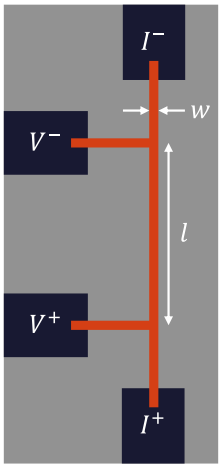

Figure F.1 – Schematic of the DC structure used for a 4-point probe measurement to find R_N and T_c. Both the voltage and current differences across a strip of width w and length l are measured to find the resistance at different temperatures.

Noise and sensitivity measurements

In section 2.2.4, we used noise-equivalent power to define sensitivity limits due to noise. In general, the NEP relates to noise power spectral density and responsivity through [30],

$$\mathrm{NEP} = \sqrt{S_X}\left(\frac{dX}{dn_{qp}}\frac{dn_{qp}}{dP_{rad}}\right)^{-1}\sqrt{1+(\omega\tau)^2}, \tag{F.3}$$

where S_X is the noise spectral density in an observable X, the response or change to that observable dX/dn_{qp}, and its limiting timescale τ (e.g., quasiparticle lifetime τ_{qp}, or resonator ring time τ_{res}). For amplitude A and phase θ, we can use the responses from equations 2.35 and 2.36. dn_{qp}/dP_{rad} describes the change of quasiparticle density under change of incoming radiation power. We can use a simple description of radiation power as a function of quasiparticles [30],

$$\eta_{opt}\eta_{pb}P_{rad} = N_{qp}\tau_{qp}/\Delta \tag{F.4}$$

which takes into account how much of the radiation power is actually absorbed inside of a volume V (optical efficiency η_{opt}), of which only a fraction results in pairs being broken (pair-breaking efficiency η_{pb}).

The power spectral density of generation-recombination noise is a Lorentzian spectrum [57, 85],

$$S_{\mathrm{g-r}}(\omega) = \frac{4N_{qp}\tau_{qp}}{1+(\omega\tau_{qp})^2}, \tag{F.5}$$

where $N_{qp}\tau_{qp}$ is constant over temperature. Photon noise, being a source of white noise, has a frequency-independent power spectral density [44],

$$S_{\mathrm{ph}} = 2P_{rad}\hbar\omega(1+mB), \tag{F.6}$$

where m is the efficiency from emission to detection of a single mode, and B the photon occupation number per mode (determined using the Bose-Einstein distribution).

Ideally, the detectors should show photon-noise-limited detection. To show whether the fabricated designs obtain this goal, we have to perform noise measurements. This evaluation can be done dark, but also by using the black body source in the setup (see figure 4.5) to achieve different levels of radiation power. For the latter case, we can prove that we observe photon-noise-limited detection, if we observe the following two characteristics in our noise spectra [64, 83]:

1. Both the phase and amplitude noise spectra are that of white noise with a Lorentzian roll-off determined by a limiting timescale τ.
2. When reducing the optical loading power from the state where photon-noise-limited detection is observed to negligible optical loading, the noise sources within the detector should become limiting. This is observed when the noise spectra are no longer that of white noise.